The mechanical regulation of RNA binding protein hnRNPC in the failing heart

Fabiana Martino[1,2,3,4], Nandan Mysore Varadarajan[5], Ana Rubina Perestrelo[1], Vaclav Hejret[5,6], Helena Durikova[1], Dragana Vukic[5], Vladimir Horvath[1,7], Francesca Cavalieri[8,9], Frank Caruso[7], Waleed S. Albihlal[10], André P. Gerber[11], Mary A. O'Connell[5], Stepanka Vanacova[5], Stefania Pagliari[#1,3], Giancarlo Forte[#1,3,12].

[1]International Clinical Research Center (ICRC) of St Anne's University Hospital, CZ-65691 Brno, Czech Republic; [2]Faculty of Medicine, Department of Biology, Masaryk University, CZ-62500 Brno, Czech Republic; [3]Competence Center for Mechanobiology in Regenerative Medicine, INTERREG ATCZ133, CZ-62500 Brno, Czech Republic; [4]Cardiac Section, National Heart and Lung Institute (NHLI), Faculty of Medicine, Imperial College London, London W12 0NN, United Kingdom.; [5]Central European Institute of Technology (CEITEC), Masaryk University, CZ-62500 Brno, Czech Republic; [6]National Centre for Biomolecular Research, Masaryk University, CZ-62500 Brno, Czech Republic; [7]Centre for Cardiovascular and Transplant Surgery, CZ-60200 Brno, Czech Republic; [8]Department of Chemical Engineering, The University of Melbourne, Parkville, Victoria 3010, Australia; [9]Dipartimento di Scienze e Tecnologie Chimiche, Università degli Studi di Roma Tor Vergata, 00133, Rome, Italy; [10]The Francis Crick Institute, London NW1 1AT, United Kingdom; [11]Dept. Microbial Sciences, Faculty of Health and Medical Sciences, University of Surrey, Guildford GU2 7XH, United Kingdom; [12]School of Cardiovascular Medicine & Sciences, King's College London WC2R 2LS, United Kingdom.

Single-sentence summary: hnRNPC is a mechanosensitive component of RNA homeostasis apparatus in heart failure.

[#]These authors contributed equally to the study. Corresponding authors. Email: giancarlo.forte@fnusa.cz (GF); stefania.pagliari@fnusa.cz (SP)

ABSTRACT

Cardiac pathologies are characterized by intense remodeling of the extracellular matrix (ECM) that eventually leads to heart failure. Cardiomyocytes respond to the ensuing biomechanical stress by re-expressing fetal contractile proteins via transcriptional and post-transcriptional processes, like alternative splicing (AS). Here, we demonstrate that the heterogeneous nuclear ribonucleoprotein C (hnRNPC) is upregulated and relocates to the sarcomeric Z-disc upon ECM pathological remodeling. We show that this is an active site of localized translation, where the ribonucleoprotein associates with the translation machinery. Alterations in hnRNPC expression, phosphorylation and localization can be mechanically determined and affect the AS of mRNAs involved in mechanotransduction and cardiovascular diseases, including Hippo pathway effector Yes Associated Protein 1 (YAP1). We propose that cardiac ECM remodeling serves as a switch in RNA metabolism by impacting an associated regulatory protein of the spliceosome apparatus. These findings offer new insights on the mechanism of mRNA homeostatic mechanoregulation in pathological conditions.

INTRODUCTION

The onset and progression of aging-associated pathologies is paralleled by continuous local extracellular matrix (ECM) remodeling. This remodeling serves as a compensatory strategy for tissues to cope with altered conditions *(1)*. ECM remodeling is perceived and transmitted within a cell through the modulation of cytoskeleton-propagated intracellular tension *(2)* that eventually affects tissue-specific cell responses and function *(3, 4)*. Cardiac pathologies are a prime example of how ECM remodeling can impact on cell functionality, here affecting muscle contractility and organ pumping *(5)*. Pathological remodeling is a complex phenomenon that includes modification of the chemical composition and the mechanical properties of the cardiac ECM. Independently of the etiology, cardiac remodeling confers a major shift in cardiomyocyte contractile function by inducing changes in signaling axes *(6)*, metabolic pathways *(7)*, and the overall epigenetic landscape *(8)*. Such changes eventually trigger modifications in the cardiomyocyte genetic program to increase cell contractility and favor cell survival *(9)*. Reactivation of the fetal cardiac genetic program is a hallmark of the pathological heart, as observed in pressure overload-induced hypertrophy *(10)*.

Post-transcriptional events such as alternative splicing (AS) and RNA editing, transport, translation and degradation are also affected in cardiac disease *(11)*. In particular, changes in AS in the pathological heart lead to alterations in the expression of sarcomeric and ion channel genes associated with cardiac pathologies, being determinants of cardiomyopathies and, eventually, of heart failure (HF) *(12)*. The mechanisms presiding over RNA homeostasis permit prompt cellular adaptation to changes in the external environment. This process is mainly controlled via RNA binding proteins (RBPs) that physically associate with and guide RNAs through all steps of post-transcriptional control. Given the importance of RBPs in RNA metabolism, their expression must be tightly controlled.

Among the RBPs, heterogeneous nuclear ribonucleoproteins (hnRNPs) represent a large family of proteins that comprise nuclear ribonucleoprotein complexes consisting of RNA and proteins, and help control mRNA dynamics *(13)*. Under stress conditions, hnRNPs may translocate to a different cellular compartment, undergo post-transcriptional modification, and/or exhibit altered protein expression; all of these events can affect the metabolism of essential transcripts needed for cell adaptation *(14, 15)*. Indeed, the mislocalization and deregulation of hnRNPs has been associated with the onset of several pathologies, including cancer, Alzheimer's disease and frontotemporal lobe dementia *(16)*.

Emerging data suggest that RNA homeostasis can be controlled by mechanical cues *(17–19)*, but the molecular basis of such processes is largely unknown. One hypothesis is that mechanical stress arising from the surrounding environment could affect RNA dynamics by either altering RBP function or localization *(20, 21)*. However, this process requires that components of the RNA processing apparatus respond to mechanical cues generated during ECM remodeling.

In this study, we show ischemic and chronic cardiac pathologies are accompanied by the altered expression of the RBP heterogeneous nuclear ribonucleoprotein C (hnRNPC). hnRNPC is a core ribonucleoprotein that is ubiquitously distributed, best known for its role as a splicing regulator *(22–24)* and associated with pathological conditions *(25–27)*. Its upregulation in diseased cardiomyocytes has been recently confirmed by single-cell RNA-sequencing in a model of ischemia-reperfusion *(28)*.

We demonstrate that hnRNPC is phosphorylated by protein kinase C (PKC), adopts a peculiar sarcomeric distribution and associates with translation machinery upon pathological ECM remodeling. Moreover, we provide evidence that hnRNPC intracellular localization can be controlled by the increased biomechanical stress generated by cardiac ECM remodeling and show that the relocation of a fraction of the protein from the nucleus is sufficient to affect the AS of transcripts coding for components of the mechanosensitive Hippo pathway. This pathway is known to be heavily involved in the progression of cardiac diseases *(29, 30)*. Therefore, we propose that hnRNPC acts as a mechanosensitive switch affecting RNA metabolism in heart failure.

RESULTS

hnRNPC is upregulated in the diseased heart

The intense ECM remodeling occurring in cardiac pathologies can alter tissue integrity and impair organ function *(5)*, but the underlying molecular mechanisms are unclear. We first asked whether this phenomenon was associated with a common transcriptomic signature in both ischemic and non-ischemic heart diseases. To do so, we analyzed four published expression profiling array datasets obtained from ischemic (mouse myocardial infarction, MI) *(31)* and non-ischemic (mouse and human HF) *(32–34)* cardiac diseases and looked for common molecular function terms among the upregulated genes in the pathological heart (**data file S1).**

We found that 11-17% of the upregulated genes in MI and HF hearts (fold change (FC)>1.5) shared the RNA binding (GO:0003723) annotation (**Fig. 1A; data file S1**). When browsing the genes encoding RBPs, we found 82 RBPs that were upregulated in both mouse datasets and four that were upregulated in both human HF datasets. We identified hnRNPC as the only common upregulated gene among all four datasets (**Fig. 1B**).

Consistently, our in silico expression array analyses showed that hnRNPC was upregulated 1.52 fold 48 h after MI and 1.77 fold in HF in mice, and from 1.68 to 4.2 fold in HF patients (**fig. S1A**; **data file S1**).

We further analyzed its expression in heart tissue specimens obtained from a cohort of 17 patients diagnosed with end-stage HF and undergoing cardiac transplantation. As a healthy control, we used non-transplantable hearts from deceased (healthy) donors (**fig. S1, B and C; table S1**). By RT-qPCR analysis, we confirmed that *HNRNPC* gene (**Fig. 1C**) was reproducibly upregulated in failing human hearts. Western blot analysis showed the expression of the protein in diseased hearts followed the same tendency, although there was no statistically significant difference upon quantification (**Fig. 1D,** $P = 0.056$). These results support that hnRNPC expression is upregulated in HF independently of the etiology of the pathology (**fig. S1, D and E**).

hnRNPC interacts with components of the myofibril in the pathological heart

We set out to investigate hnRNPC binding partners and how these might change upon HF. Therefore, we pulled down the endogenous protein in human end-stage failing and healthy control heart left ventricle apex samples and quantitatively analyzed the immunoprecipitated (IP)

complexes by tandem mass tag spectrometry (TMT-MS, **Fig. 2A**). We identified 194 unique proteins interacting with hnRNPC in HF, and 127 in healthy samples: only 55 interactors were common to both conditions (**Fig. 2B; data file S2**).

We weighted the specific HF and healthy interactor proteins for their abundances in the hnRNPC-IP complexes and used the resulting data to build proteomaps based on KEGG database *(35)*. This approach allowed us to visualize how the hnRNPC interactome composition changed in the pathology with a focus on the function of its binding partners (**Fig. 2C** and **data file S2**). We found that hnRNPC mainly interacted with components of the spliceosome complex in both healthy and HF, consistent with its acknowledged function in RNA splicing *(23, 24)*. More interestingly, HF-specific interactors returned a common annotation for cardiac muscle contraction and cytoskeletal proteins (**Fig. 2C**), suggesting that hnRNPC might display a distinct localization in the pathological heart (**fig. S2A**).

We next performed gene ontology (GO) analysis of hnRNPC interactors in healthy and diseased heart to identify which cellular component they belonged to. This analysis revealed that HF-specific hnRNPC interactors included proteins belonging to the myofibril (**Fig. 2D; fig. S2B**). Together with the annotation for cytosolic and polysomal ribosome, which was predominant for hnRNPC interactors in HF samples (**Fig. 2D**), these data support a differential localization of the protein in the pathological heart.

hnRNPC localizes to the Z-disc of the sarcomeric apparatus

hnRNPC is mainly localized in the nucleus of healthy cardiomyocytes, whereas our mass spectrometry analysis suggested that it might relocate at the sarcomeres in HF. To confirm our hypothesis, we investigated hnRNPC intracellular localization in the human myocardium. Besides finding an expected nuclear localization in cardiomyocytes, we also detected hnRNPC in the cytoplasm of the contractile cells in HF, with a characteristic striated pattern closely following the distribution of cardiac troponin T (TNNT2) (**Fig. 3A**). Using structured-illumination microscopy (SIM) to resolve the subcellular distribution of the protein, we observed that hnRNPC was localized at the Z-disc of the sarcomeres in HF (**Fig. 3B; fig. S3A**) with a lateral resolution of ~125 nm. The shuttling of a fraction of the protein in the diseased heart was confirmed by western blot analysis of nuclear

and cytoplasmic extracts. This experiment also indicated a reduction in hnRNPC nuclear expression in the pathological heart (**fig. S3B**).

To understand whether hnRNPC sarcomeric distribution can be considered a common feature of cardiac pathologies, we analyzed hnRNPC localization in a model of MI generated by left anterior descending (LAD) coronary artery ligation in C57BL/6 mice *(36)* (**fig S3, C and D)**. We stained the infarction border and the distal zone of the infarcted myocardium with an antibody directed against hnRNPC at day 4 post-MI, when the tissue is stormed by intense inflammatory response and at day 21 post-MI, when the acute phase is resolved and the scar is stabilized *(5)*. As expected, hnRNPC showed a characteristic nuclear localization in both the healthy and ischemic heart. When co-stained with TNNT2, hnRNPC also displayed a clear sarcomeric pattern in cardiomyocytes located at the infarct border zone 21 days post-MI. A similar pattern could be detected at the earlier time-point (day 4 post-MI). Image analysis clarified the co-localization between hnRNPC and TNNT2 was only significant (P=0.0016) at day 21 post-MI as compared to sham-operated control. No such phenomenon was found far from the infarct, at the distal zone (**Fig. 3C**). These results suggest that in cardiomyocytes at the border zone of the infarction hnRNPC translocates to the sarcomeres where it interacts with sarcomeric components.

To further confirm hnRNPC sarcomeric localization in failing hearts, we performed a proximity ligation assay (PLA) with TNNT2 (**Fig. 3D**; **data file S2**). We found that hnRNPC and TNNT2 are located within 40 nm of each other in HF and that the number of interactions, as indicated by PLA dots, was significantly lower in healthy hearts (**Fig. 3D**). We also confirmed the physical interaction between hnRNPC and other sarcomeric proteins (FHL2, PDLIM5, MYH7) identified by TMT-MS in HF but not in the healthy heart by co-IP analysis (**Fig. 3E**).

To further corroborate hnRNPC interaction with FHL2 and PDLIM5, we pulled the two endogenous proteins down in 2 HF samples and resolved the interacting proteins (**data file S3**). hnRNPC presence was confirmed in both IP preparations by MS analysis and by western blot (**fig. S3E; data file S3**). FHL2, PDLIM5 and hnRNPC interactomes returned 143 common binding partners in the failing heart (**fig. S3F**) with a common annotation for actin cytoskeleton and myofibril component (**fig. S3G**; **data file S3**).

The sarcomeric distribution of hnRNPC in HF suggests this protein might have distinct functions in physiological and pathological conditions.

hnRNPC binds transcripts encoding components of cardiomyocyte contractile apparatus in HF

To understand the role of hnRNPC at the sarcomere in HF, we next determined which transcripts it physically binds. To do so, we carried out RNA-binding protein-immunoprecipitation (RIP) followed by high-throughput sequencing (seq) in three human HF samples (**Fig. 4A; fig. S4A**). Next, we found that the distribution of reads on genomic regions (intron/exon, 5'UTR, 3'UTR, CDS) in the hnRNPC-IP library mostly mapped to intronic regions (63%), followed by coding DNA sequences (CDS, 22%), 3' (13%) and 5' (2%) untranslated regions (UTRs) (**Fig. 4B**). After browsing the POSTAR2 database, we confirmed that 2,487 out of 2,629 RNA targets found in our RIP-seq experiment harbored at least one binding site for hnRNPC *(37)* (**fig. S4B**).

Next, we calculated the number of reads mapping to a specific region (intron/exon, 5'UTR, 3'UTR, CDS) for each gene. By this approach, we could define two groups of targets: the transcripts enriched in intronic and those enriched in exonic reads (exon, CDS, 5' and 3' UTRs) (**fig. S4C; data file S4**). The large proportion of intronic hits is consistent with the documented role of hnRNPC in pre-mRNA splicing *(22)*. Although RBPs can regulate pre-mRNA splicing by binding to exonic splicing enhancers or silencers *(38)*, we hypothesized that the exon-enriched targets found in the pathological heart could represent mature RNAs that might be informative as to hnRNPC activity at the sarcomere.

We then performed GO analysis of hnRNPC targets and identified that the intron-enriched targets (1,681) mostly belonged to the nucleus, cytoskeleton, and adhesion categories, while 18.8% of all annotated I-band components were hnRNPC targets (**Fig. 4, C and D**). Among the latter we found transcripts such as LDB3, CACNA1C, DMD, PDLIM5, for which an alteration in AS has been previously assigned to the occurrence of cardiac pathologies *(12, 39)*. Moreover, we found splicing regulators among the hnRNPC targets (including RBM20, MBNL2, CELF1-2, RBFOX1-2) that are involved in heart development and disease *(40, 41)*. These findings indicate that hnRNPC could exert both a direct and indirect role in splicing control of sarcomeric transcripts affecting the post-transcriptional regulation of other RBPs. Selected hnRNPC intron-enriched targets showing high read coverage on intronic regions as obtained by Integrative Genomics Viewer (IGV) are shown in **Fig. 4E** and in **fig. S4D.**

We performed a cellular component enrichment analysis of the hnRNPC exon-enriched targets and identified an enrichment for the myofibril, troponin complex, A and I bands of the sarcomeres (**Fig. 4F**). Titin (*TTN*), cardiac muscle alpha actin (*ACTC1*) and troponin I (*TNNI3*) contractile apparatus transcripts were found among hnRNPC targets (**Fig. 4, G and H; fig. S4E**). When we analyzed the enriched biological processes by these exon-enriched hnRNPC targets, we found that these targets were mainly involved in muscle structure development (22), filament sliding (9), contraction (14) and myofibril assembly (9) (**fig. S4F**). By comparison, the intron-enriched targets were principally associated with the regulation of signal transduction (472), cell communication (513), cytoskeletal organization (209) and heart development (113) (**fig. S4G**).

This finding suggests that, besides its acknowledged role in splicing, hnRNPC might be also implicated in the translational regulation of selected targets upon its translocation to the sarcomeres in HF.

ECM pathological remodeling induces hnRNPC association with translation machinery at the sarcomere

Next, we queried the role of hnRNPC at the sarcomeres. *TTN*, *ACTC1* and *TNNI3* transcripts, found among hnRNPC exon-enriched targets, are translated at the sarcomeres in the rat heart, in a process dubbed as 'localized translation' *(42, 43)*. This process allows for the spatiotemporal control of contractile protein synthesis at the sarcomeric site *(43, 44)*. Previous reports have shown ribosomes are present at the sarcomeres in the rat heart, where localized translation occurs *(43, 45)*. Consistently, our TMT-MS analysis identified nine ribosomal proteins in the hnRNPC interactome in the failing heart (**fig. S5A**) which accounted for the ribosome annotation found in GO cellular component analysis (**Fig. 2D**). To confirm the presence of the ribosomes at the sarcomeric structure, we labeled the evolutionarily conserved RPS6 ribosomal protein (which was a potential hnRNPC interactor in our TMT-MS analysis) in healthy control and HF cardiac tissue sections. We found a typical sarcomeric cross-striated pattern, as confirmed by TNNT2 staining, in both groups (**fig. S5B**). We observed a similar pattern in the sarcomeres of cardiomyocytes residing both at the distal and at border zones of MI, as well as in healthy cardiomyocytes in the murine heart (**fig. S5C**).

Because we found that hnRNPC relocated to the sarcomeres in HF and confirmed the presence of the ribosomes at this site in the human heart, we asked whether sarcomeres could be a site of localized translation in human cardiomyocytes. Therefore, we derived contractile cardiomyocytes from human induced pluripotent stem cells (iPSC-CMs) through an established protocol *(46)*. In differentiated cells, we first confirmed RPS6 presence at the sarcomeres by colocalization analysis of the protein with cardiac TNNT2 (**Fig. 5A**). Next, we performed a ribopuromycylation assay that exploits puromycin mimicry of aminoacylated tRNA to visualize the active sites of translation (**fig. S5D**). Here, puromycin (PMY) could be incorporated in the contractile apparatus of human iPSC-CMs, thus demonstrating human cardiomyocyte sarcomeres are active sites of protein translation (**Fig. 5B**).

Next, we investigated whether hnRNPC associates with the translation machinery when localized at the sarcomeres in the pathological heart. To do this, we adopted an original reductionist approach to reproduce some key mechanical features of pathological cardiac ECM remodeling by decellularizing healthy control and diseased human heart tissue (dECMs) *(30, 47)*. We used the homogenized dECMs to coat the surface of cell culture plates. Next, we seeded contractile iPSC-CMs on healthy and pathological dECMs and combined ribopuromycilation with PLA assay to investigate whether hnRNPC localized close to the active translation sites, as indicated by PMY staining (**Fig. 5C**). The analysis showed significantly (P= 0,0286) higher number of PLA dots, corresponding to hnRNPC–PMY proximity, in TNNT2-positive cells cultured on pathological dECMs as compared to iPSC-CMs grown on healthy control dECMs (**Fig. 5D**). By using the same approach, we also confirmed that hnRNPC is localized in proximity of sarcomeric TNNT2 in iPSC-CMs cultured on pathological dECM (**fig S5E**). These data confirm that sarcomeres are active sites of RNA translation and that hnRNPC localizes to those sites as a result of cardiac ECM pathological remodeling.

hnRNPC intracellular localization is controlled by cell spreading and cytoskeletal tension

We next tried to disentangle the role of the mechanical stress associated with ECM remodeling *(5, 30)* in hnRNPC localization. Using surfaces with the same chemical composition and controlled rigidities (1.5 vs 28 kPa), we repeated the ribopuromycilation assay followed by PLA on iPSC-CMs. The elasticity values selected have been shown to induce mechanosensor activation in other cell systems *(48–50)*. Here we found hnRNPC localization to the sites of active translation, as detected

by PMY interaction, was sensitive to the stiffness of the substrate, since PLA signal was significantly (*P*=0.0286) different on substrates with different elasticities. This result suggests that substrate stiffness *per se* can induce hnRNPC shuttling (**fig. S6A**).

To corroborate this result, we challenged normal human dermal fibroblasts (NHDFs), a highly mechano-responsive cell type, with different mechanical stimuli and analyzed hnRNPC distribution. Here, we used a fibrin-based three-dimensional (3D) culture system, whose mechanical properties can be tuned in a physiological range by modulating the fibrinogen concentration in the presence of constant amount of thrombin *(51)* (**fig. S6B**). We embedded NHDFs into the hydrogels and analyzed hnRNPC localization after 48 hours. We additionally stained F-actin to monitor cell spreading within the hydrogels, indicative of the degree of cytoskeletal tension. We observed that NHDFs spread well in soft (2 mg/ml and 5 mg/ml fibrinogen) hydrogels, but failed to elongate as the stiffness of the fibrin gel increased (17 mg/ml fibrinogen). At the highest fibrinogen concentration (50 mg/ml), the cells were unable to acquire an elongated morphology (**fig. S6C**). Image analysis demonstrated that hnRNPC nuclear localization was affected by NHDF volume and cellular ability to spread within soft hydrogels, with hnRNPC translocation to the cytoplasm characteristic of cells confined in stiff fibrin gels (**Fig. 6A; fig. S6C**). These data suggest that hnRNPC nuclear localization might be controlled by intracellular tension and cell spreading within the surrounding milieu.

To corroborate our hypothesis, we used fibronectin-coated micropatterned surfaces to precisely control single cell area *(49, 50, 52)*. We stained hnRNPC in NHDFs and used YAP1 as an example of a mechanosensitive protein whose localization depends on intracellular tension and cell spreading *(49, 50)*. Confocal analysis showed that hnRNPC localized at the nucleus in cells that were confined to bigger areas (2,025 μm^2) or free to spread. By contrast, the protein shuttled to the perinuclear region of cells constrained on smaller surfaces (1,024 and 300 μm^2) (**Fig. 6B; fig. S6D**). To resolve the intracellular distribution of the protein, we counterstained with Lamin A/C and visualized the cells by SIM. Here we found that hnRNPC egressed the nucleus and acquired a perinuclear localization in constrained cells, with a peculiar distribution close to Lamin A/C nuclear invaginations (**Fig. 6C**). We repeated the same experiment using iPSC-CMs and again observed that hnRNPC nuclear localization was also sensitive to cell spreading in contractile cells (**fig. S6E**).

Having shown that hnRNPC nuclear localization required the cell to spread in two and three dimensions, we next performed in depth experiments to clarify whether the shuttling of the protein

was driven by the availability of adhesion sites within the local ECM or by the transmission of intracellular tension. We first designed single cell fibronectin-coated micropatterned arrays that maintain constant cell area (4,900 μm^2) while reducing the number of fibronectin adhesion spots *(49)*. When we decreased the adhesion area (1,000 and 450 μm^2), we saw no significant effect on hnRNPC nuclear localization (**fig. S6F**). We concluded that adhesion did not affect hnRNPC localization.

Next, we inhibited the transmission of intracellular tension by treating NHDFs with pharmacological inhibitors of either RhoA/ROCK pathway (Y27632) or F-actin polymerization (Latrunculin A) *(2, 53)*. We analyzed hnRNPC localization in the nucleus and cytoplasm by cell fractionation followed by western blotting and detected a significant decrease in nuclear hnRNPC and the concomitant increase in its cytoplasmic expression in cells treated with the pharmacological inhibitors (**Fig. 6D**). These data are consistent with the hypothesis that the inhibition of intracellular tension leads to a reduction in hnRNPC nuclear expression and the shuttling of a fraction of the protein to the cytoplasm. Finally, since YAP1 shuttling is regulated via phosphorylation *(2)*, we treated NHDFs with Y27632 and found the inhibition of intracellular tension resulted in increased hnRNPC phosphorylation, as shown by western blot (**Fig. 6, E and F**), indicative of phosphorylated protein shuttling to the cytoplasm. Next, we inhibited the activity of PKC, a family of serine-threonine kinases which have been implicated in the pathogenesis of HF and proposed as potential pharmacological targets *(54)*. PKC inhibition caused a significant decrease in hnRNPC phosphorylation and its presence in the cytoplasm (**Fig. 6F**). However, PKC inhibition could not completely abolish hnRNPC phosphorylation in the presence of RhoA/ROCK inhibitor, suggesting other kinases might be involved in the process.

hnRNPC regulates the AS of genes involved in mechanotransduction

As hnRNPC is associated with the spliceosome and mainly nuclear in physiological conditions, we studied which changes in terms of AS events would cause the reduced contribution of hnRNPC to the splicing process. We therefore knocked down (KD) hnRNPC in NHDFs using two independent siRNAs (**Fig. 7A**) and analyzed the abundance of RNA splicing variants by high throughput genome-wide RNA-seq. We then adopted the multivariate analysis of transcript splicing (MATs) statistical algorithm to quantify the changes in AS driven by hnRNPC downregulation. We identified the differential splicing of 2,032 RNA transcripts (FDR< 0.01 and $|\Delta PSI| \geq 0.1$) in KD cells, as compared

to the scrambled control-transfected cells (**data file S5**). Consistent with previous reports *(24, 55)*, most of the splicing events affected by hnRNPC KD consisted of skipped exons (SE: 78.95%), followed by mutually exclusive exons (MXE: 14.85%), alternative 3'-5' splice sites (A3SS: 3.76% and A5SS: 2.15%) and intron retention (IR: 0.3%) (**Fig. 7B**). Pathway enrichment analysis of the 2,032 differentially spliced genes in hnRNPC KD cells revealed that the splicing of multiple genes involved in cell mechanotransduction, integrin-mediated cell adhesion and focal adhesion were affected (**Fig. 7C**). In particular, 15 components of the Hippo signaling pathway, a mechanosensitive molecular axis involved in heart development *(29)* and diseases *(52, 56)*, displayed altered AS upon hnRNPC silencing (**data file S6**).

Among these we found the main effector of Hippo pathway, YAP1. *YAP1* encodes for multiple protein isoforms (**Fig. 7D**). The distinct co-transcriptional fingerprints of the splicing variants depend upon the presence of one (YAP1-1) or two (YAP1-2) WW domains *(57)*. The exon 4, which encodes for the second WW domain in YAP1-2 isoforms, was found differentially spliced in hnRNPC-depleted cells by RNA-seq. We thus analysed the inclusion of exon 4 in YAP1 transcript upon hnRNPC KD by calculating the relative abundance of YAP1 isoforms including (YAP1-2) or lacking (YAP1-1) exon 4 by RT-qPCR and by conventional PCR. We found that hnRNPC depletion promoted the inclusion of exon 4 in YAP1 transcript and affected the overall balance among YAP1-1 and YAP1-2 splicing variants (**Fig. 7E, and fig. S7A**). These results were confirmed in hnRNPC-depleted iPSC-CMs (**fig. S7, B and C**). Additionally, we obtained similar results by treating NHDFs with inhibitors of cytoskeletal tension (**Fig. 7E**), suggesting that hnRNPC shuttling out of the nucleus affects YAP1 AS.

To prove that hnRNPC displacement is responsible for the changes observed in YAP1 AS we genetically targeted the RBP to the cytoplasm via disruption of its nuclear localization sequence (NLS). After confirming the cytoplasmic localization of hnRNPC-NLS mutant in HeLa and NHDF cells (**fig. S7D**) we analyzed the effect of hnRNPC displacement on YAP1 AS (**Fig. 7F, fig. S7E**). The overexpression of hnRNPC-NLS mutant in both HeLa and NHDF cells (lacking endogenous hnRNPC) promoted the inclusion of exon 4 in YAP1 transcript (**Fig. 7F, fig. S7E**). Hence, the mechanical displacement of hnRNPC from the nucleus affects the splicing of YAP1 by promoting exon 4 inclusion.

To validate this set of data, we analyzed the expression of the variable exon 7 of CD44 transcript, whose AS has been proven mechanosensitive *(58)*. As expected, here we found the inclusion of variable exon 7 in CD44 transcript increased upon hnRNPC depletion as well as upon treatment with

inhibitors of tension in NHDFs (**fig. S7F**). We also validated the reduced expression of MYLK exon 11 and COL6A3 exon 3 found by RNA-seq in hnRNPC KD cells by RT-qPCR (**fig. S7, G and H**).

Next, we compared the differentially spliced genes in hnRNPC KD cells to the RNAs known to harbor hnRNPC binding sites (as documented in the POSTAR2 database). We found as many as 1,738 among the 2,032 transcripts had at least one hnRNPC binding site and could, in principle, interact with the RBP (**fig. S7I**). To check that those were true hnRNPC targets, we performed individual-nucleotide resolution cross-linking and immunoprecipitation (iCLIP). This approach allowed us to map precisely hnRNPC-RNA interactions and relate them to the previously detected hnRNPC-dependent splicing events in NHDF cells (**fig. S8, A and B; data file S7**). A total of 1,470,396 uniquely mapped hnRNPC crosslink events were identified, which clustered into 13,567 binding sites in 5,536 transcripts (**data file S7**). As a control, we found the majority of hnRNPC crosslink events to be located within introns, with high coverage of Alu elements, in good agreement with previous results obtained in other cell types *(22, 23)* (**fig. S8, C and D**). While 58% of the crosslink events mapped to coding sequences, several non-coding hnRNPC targets were also identified, including MALAT-1, a long non-coding RNA whose interaction with hnRNPC has already been described *(59)* (**fig. S8, E to G**).

Next, we matched the results of AS events in hnRNPC KD cells with those obtained by iCLIP. We searched for all transcripts directly bound by hnRNPC to determine whether they displayed AS in hnRNPC-depleted cells. We ultimately detected 748 transcripts physically interacting with hnRNPC in NHDFs that were differentially spliced in the absence of the protein (**Fig. 7G; data file S7**). Among those, we confirmed the presence of seven components of the Hippo pathway (**Fig. 7H; data file S6**), on which hnRNPC binding occurred in intronic regions surrounding exons alternatively spliced in hnRNPC-depleted cells (**Fig. 7, I and J**; **fig. S9).** This was the case for YAP1 transcript, for which the RNA-binding protein iCLIP coverage in the proximity of the hnRNPC-dependent exon 4 could be confirmed (**Fig. 7J**). The data were validated by independent iCLIP-PCR assay for three selected hnRNPC targets: *YAP1*, *CD44* and *MYLK* (**fig. S10**). In summary, these results suggest that hnRNPC is directly involved in the regulation of AS of pre-mRNAs encoding genes involved in mechanotransduction.

hnRNPC regulates the AS of genes involved in cardiovascular diseases

We next used our iCLIP and AS analyses to validate the RNA-IP results obtained in the diseased human heart **(Fig. 4).** We figured this approach might help us unveil the direct targets of hnRNPC in

the pathological heart, where the RBP expression and localization are perturbed**.** We matched the three datasets to identify 389 common transcripts which are physically bound by hnRNPC in failing hearts and undergo AS in its absence (**Fig. 8A; data file S8**). Among them, we again confirmed the presence of the components of the Hippo pathway (**data file S6**).

The Comparative Toxicogenomics Database (CTD) annotation of the transcripts targeted for gene-disease associations yielded cardiovascular, cancer and neurological diseases as the main represented categories (**Fig. 8B; data file S8**). In particular, 41 direct targets of hnRNPC belonging to the cardiovascular disease category displayed AS in hnRNPC KD cells (**Fig. 8C; data file S8**). We confirmed the importance of hnRNPC depletion in exon inclusion by visualizing the splice junction of selected transcripts belonging to this category and by highlighting hnRNPC binding sites on those transcripts (**fig. S11**).

Next, we investigated whether the splicing events determined by hnRNPC depletion in vitro are relevant in HF. Hence, we analyzed YAP1 exon 4 splicing in our cohort of patients diagnosed with HF and found an increase in exon 4 inclusion in most of the samples (**fig. S12**). The variability of this result is expected due to the intrinsic complexity of the cardiac tissue (i.e.: heterogeneous cellular composition of the failing human heart, presence of fibrotic tissue).

We then used the MATS statistical algorithm to quantify the changes in YAP1 exon 4 AS in previously published RNA-seq datasets obtained from patients diagnosed with heart failure (GSE108157 and GSE141910). Here, we confirmed that failing human hearts displayed a higher inclusion of exon 4 in YAP1 transcript, thus supporting our data (**fig. S12B**). Finally, we used the same RNA-seq datasets to further corroborate the clinical relevance of the AS events affected by hnRNPC depletion on a larger scale and found that AS events determined by hnRNPC KD in NHDFs also occurred in the failing heart, independently of the etiology of the pathology (**fig. S12C**; **data file S9**).

Taken together, these results indicate that pathological ECM remodeling in the failing heart induces hnRNPC phosphorylation and its shuttling to the sarcomeres, where the RBP localizes in close proximity to the translation machinery. A reduction in hnRNPC nuclear localization and in its contribution to the splicing process affects the AS of mechanosensitive transcripts and RNAs involved in cardiovascular diseases.

DISCUSSION

The active cardiomyocyte response to ventricular remodeling is considered as a compensatory mechanism that aims to minimize the detrimental effects of the increased biomechanical stress on cardiac output, while protecting the integrity and the pumping activity of the organ *(60)*.

Here we performed an in silico analysis of published expression profiling array datasets obtained from ischemic and non-ischemic hearts, with the aim of identifying molecular mediators that help ensure cell adaptation to the new demands of the pathological organ by reshaping gene expression. We observed a general upregulation of RBP expression in the pathological heart in humans and in mice, independently of the etiology of the pathology. Among the RBPs consistently altered in the diseased heart, we identified the upregulation of hnRNPC, an abundant nuclear protein that has mainly been studied for its role as a splicing factor *(22–24)*. hnRNPC upregulation was independently confirmed by single-cell RNA sequencing in cardiomyocytes *(28)*.

We took hnRNPC forward for further analyses, using quantitative proteomics, super-resolution microscopy and PLA to discover that hnRNPC shuttles out of the nucleus and localizes to the sarcomeres of cardiomyocytes in the pathological heart. We confirmed this observation by biochemical analyses and found that the protein settles at the Z-disc, where it physically interacts with components of the contractile apparatus, including TNNT2, PDLIM5, FHL2 and MYH7.

hnRNPC upregulation has been associated with different pathologies, including atherosclerosis and pre-atherosclerotic intimal hyperplasia *(27)*, neurodegenerative diseases *(25)* and some forms of cancer (e.g. gastric cancer) *(61)*; however, modifications in its localized function have not been described in pathological conditions. Indeed, most hnRNPs shuttle between the nucleus and the cytoplasm; hence their interaction with specific binding partners can be considered an indicator of their function at specific cell compartments. In chemoresistant gastric cancer, hnRNPC was upregulated and localized to the cytoplasm and membrane, but its function in these compartments was not investigated *(61)*. Our mass spectrometry analysis of hnRNPC-interacting proteins in diseased human heart samples confirmed that hnRNPC protein interacts with the spliceosome, as previously demonstrated *(62)*. However, the presence of spliceosome components was reduced in hnRNPC interactome in failing hearts compared to healthy hearts. The presence of proteins

belonging to the cytoskeleton, the sarcomere and the ribosome specifically in the failing heart interactome suggested a different function for hnRNPC in diseased conditions.

To identify this function, we performed RIP-seq and found several specific exon-enriched hnRNPC-bound RNAs in the failing heart, mostly encoding for sarcomeric proteins. Some of these mRNAs, including *TTN*, *ACTC1* and *TNNI3*, are translated locally at the sarcomere *(42, 43)*. Together with the evidence that hnRNPC interacts with ribosomal proteins at the sarcomere, these data led us to hypothesize that hnRNPC shuttling to the contractile apparatus in the failing heart could be associated with the localized translation of transcripts encoding for contractile proteins.

Localized translation has been described in different cell types, including neurons *(63)*, fibroblasts *(64)* and myoblasts *(65)*, as a strategy aimed at maximizing the synthesis of needed proteins directly at the site of exploitation. Indeed, hnRNPC was previously found in RNA granules in neurons together with mRNAs involved in synaptic remodeling, which are transported to the subsynaptic site and translated in response to an input *(66)*. Sarcomeres serve as sites of active translation in the rat heart, where the translation machinery and mRNAs encoding for sarcomeric proteins are localized *(43)*. We used iPSC-derived cardiomyocytes to visualize the active incorporation of PMY (an indicator of active translation) at the sarcomere, where ribosome components are found. By coupling dECM obtained from healthy and diseased human hearts with ribopuromycilation and PLA, we found that the pathological dECM induces hnRNPC recruitment to the sarcomeric active sites of translation.

Because cardiac ECM remodeling is associated with mechanical stress, we used 3D hydrogels with controlled stiffness and micropatterned surfaces to demonstrate that a fraction of hnRNPC can shuttle outside of the nucleus when the transmission of intracellular tension is hindered. We confirmed that shuttling to the cytoplasm is precipitated in constrained cells that cannot propagate intracellular tension. It thus seems that the mechanical stress associated with ECM remodeling serves as a switch for hnRNPC redistribution from the nucleus to the sarcomere, presumably to modulate its role in RNA homeostasis. We also investigated the mechanism of mechanical regulation of hnRNPC localization. Mechanosensitive proteins like YAP/TAZ are restricted to the cytoplasm when phosphorylated *(2)*. Additionally, the function of many RBPs can be tuned by phosphorylation *(67)*. Therefore, we used an inhibitor of intracellular tension which induced hnRNPC relocation to the cytoplasm to demonstrate mechanical stress triggers hnRNPC

phosphorylation. This event appeared to be required for hnRNPC shuttling from the nucleus, since the concomitant inhibition of PKC kinase activity hindered phospho-hnRNPC translocation. Members of the PKC kinase family have been recently proposed as novel targets to treat cardiac diseases: inhibitors of PKC (i.e.: ruboxistaurin) have been successfully used in large scale clinical trials to confer protection against infarction-induced heart failure *(54, 68, 69)*.

Given hnRNPC shuttling out of the nucleus and its reduced interaction with spliceosomal components, we investigated the effect of hnRNPC depletion on pre-mRNA AS. To mimic a situation in which hnRNPC function in splicing is reduced, we induced its shuttling from the nucleus by pharmacological inhibitors of tension in NHDFs, which are known to be sensitive to mechanical cues. Together with the results obtained by hnRNPC knockdown in NHDFs and iPSC-derived cardiomyocytes, these experiments indicate that hnRNPC depletion from the nucleus affects the AS of mechanosensitive transcripts and genes involved in cardiovascular diseases.

Next, we used iCLIP-seq to confirm that among hnRNPC direct targets were components of the Hippo pathway, a molecular axis involved in organogenesis and whose dysregulation has been associated with pathologies *(70)* including those affecting the heart *(29, 52, 56, 71)*. Mechanically induced hnRNPC displacement from the cell nucleus or its depletion affected the inclusion of exon 4 in YAP1 transcript. We further confirmed this result by genetically targeting the RBP to the cytoplasm via disruption of its NLS. This splicing event is of particular relevance since the exon encodes for the second WW domain, a domain known to directly control the protein interaction with TEAD transcription factor and thus its DNA binding activity *(49)*. This switch towards the expression of YAP1-2 isoforms with two WW domains has been recently described by our research group in human pathological hearts *(57)* and confirmed in other two independently published RNA-seq datasets.

Going forward, questions remain on the specific role of hnRNPC (e.g., repressor versus activator) at translation sites at the sarcomere, where our data suggest an involvement of the protein in localized translation. Also, our results do not clarify whether hnRNPC plays a direct role in this process and its relevance in the establishment and progression of cardiac diseases. The presence of the hnRNPC transcript in our RIP- and iCLIP-seq analyses suggests that hnRNPC could regulate its own RNA post-transcriptionally, similar to the autoregulatory feedback shown for other RBPs *(72)*. Further studies are thus needed to elucidate whether hnRNPC adopts this mechanism to regulate its expression and function in cardiac pathologies. The study has been performed mostly on human specimens.

Although corroborated by animal and in vitro studies, the impact of the results is limited by the heterogeneity of cardiac diseases as well as by the limited number of controls (healthy donors). The amount of tissue received was variable, so in some cases it was not possible to perform all the experiments.

In conclusion, our results on the regulation of hnRNPC localization and function unveil a novel mechanism by which RNA homeostasis could undergo mechanical regulation following pathological cardiac ECM remodeling (**fig. S13**). In the frame of the new therapeutic strategies using antisense oligonucleotides being developed that aim to rescue AS defects, our study supports that modifications in ECM mechanics influence RBP function and AS regulation in the diseased heart. Additionally, our results identify hnRNPC as a potential target to correct aberrant AS. Finally, given the distinct transcriptional fingerprint of different YAP1 isoforms in healthy and pathological cardiomyocytes, controlling their AS by either antisense oligonucleotides or by indirectly targeting RBPs via ECM remodeling might be an approach to rewire cardiac cell function in the diseased heart.

Materials and Methods

Study design

This study was designed to identify a common signature in the transcriptional landscape of the pathological heart. We used unbiased bioinformatics analysis of gene expression arrays and identified hnRNPC as an RBP upregulated in failing human and murine hearts, regardless of the etiology of the disease. Super-resolution microscopy, PLA and immunoprecipitation were adopted to resolve the distribution of hnRNPC at the Z-disc of pathological cardiomyocytes. Human healthy control and failing hearts were used together with mouse hearts subjected to MI to study the expression, interactome and distribution of hnRNPC in vivo. Multiple cell lines were used to investigate the mechanism of hnRNPC shuttling upon mechanical stress and the effect of its displacement from the nucleus on AS. Transcriptomic techniques (RNA-seq, RIP-seq, iCLIP-seq) were performed to identify hnRNPC direct targets. Sample sizes were dictated by the availability of human tissue. For cell culture experiments group sizes were determined based on previously published experiments in which statistical differences were identified. No exclusion criteria were pre-established, and no data were excluded from analyses. Information on the number of times the experiments were replicated is given in each figure legend. Further details are available in the **Supplementary Materials and Methods file**.

Study approval

This study was performed in accordance with the ethical standards of the Centre of Cardiovascular and Transplantation Surgery (CKTCH) and was approved by the Ethics Committee of CKTCH (EK 46/2017). The experiments were done according to the Declaration of Helsinki (2000) of the World Medical Organization. Experiments involving mice were approved by the Instituto de Biologia Molecular e Celular – Instituto de Engenharia Biomédica (IBMC-INEB) Animal Ethics Committee and the National direção Geral de Veterinária (permit no: 022793) and conformed with Directive 2010/63/EU of the European Parliament.

Patient-derived heart samples

Diseased heart tissue samples (N=17) were obtained from left ventricle apex of patients diagnosed with end-stage heart failure undergoing cardiac transplantation or ventricular assist device implantation. The classification of ischemic (N = 8) and non-ischemic (N = 9) heart failure is defined

based on the patient anamnesis, as per the International Statistical Classification of Diseases and Related Health Problems (ICD-10). Healthy hearts (left ventricle apex) (N=3) obtained from deceased organ donors without a history of cardiac disease were used as a control (**table S1**).

Mouse model of myocardial infarction (MI)

MI was experimentally induced by ligating the left anterior descending coronary artery in C57BL/6 adult mice (9-10 weeks, Charles River), as previously described *(36)* (**Supplementary Method 1**). Animals of different sex (1:1 ratio) were randomly assigned to the experimental groups to avoid the impact of sex-specific effects. The mice hearts cohort was composed of 4 days post-MI (acute MI), 21 days post-MI (chronic MI), and sham-operated (no ligation of the coronary artery) (**fig. S3B**). All animal experiments were approved by the local Ethics Committees.

Protein Immunoprecipitation (IP) and Mass spectrometry

For the IP of hnRNPC-binding proteins, 100 mg of tissue from the human heart sample was used for each IP and control sample (**Fig. 2A**). The sample was dissected and mechanically homogenized in 1 ml of Lysis Buffer. Dynabeads Protein G (50 µl/sample) were incubated with 200 µl primary antibody (5 µg/sample) for 45 min at 4 °C. Heart lysates were incubated with antibody conjugated Dynabeads overnight at 4°C. The proteins were then eluted by incubation with 100 µl 8M Urea (20 min at RT). The eluates were then processed for mass spectrometry analysis (**Supplementary Method 2 and 3; table S2**).

Decellularization of human myocardial tissue and preparation of ECM coating

The decellularization protocol was performed as previously described *(30, 74)* (**Supplementary Method 4**). The ECM-enriched scaffold was mechanically disrupted and used as 2D coating for cell culture (**Fig. 5, C and D**).

Ribopuromycilation

Ribopuromycilation protocol (RPM) to visualize active sites of translation was performed following the original RPM protocol – Procedure A (*77, 78*) (**Supplementary Method 5**; **Fig. S5D**). The RPM experiments were performed on beating cardiomyocytes between days 20 and 30 of differentiation.

Cell culture, differentiation, transfection, treatment and micropatterning

Culture of the human induced pluripotent stem cell line DF 19-9-7T (iPSC) (WiCell) and normal human dermal fibroblasts (NHDFs, ATCC) as well as cardiac differentiation is detailed in **Supplementary Method 6**. Cell treatments, 3D cultures in fibrin gels and micropatterning are detailed in **Supplementary Method 7**.

HNRNPC knockdown was performed as previously described (*23*). Detailed procedures for siRNA transfection, plasmid mutagenesis, qRT-PCR and western blotting are described in **Supplementary Method 8 to 10**.

RNA Immunoprecipitation (RIP)

To immunoprecipitate hnRNPC-binding RNAs, 100 mg tissue from the human heart sample was used for each IP and control sample. In brief, the heart samples were dissected, cross-linked in 1% (v/v) formaldehyde, mechanically dissociated in 1 ml Polysome Lysis Buffer (PLB) and sonicated. Dynabeads Protein G (100 µl/sample) were incubated with 10 µg of primary antibody (**table S2**) for 1 h at 4 °C. Cross-linked lysate was incubated with antibody-conjugated Dynabeads overnight at 4°C. Reverse cross-linking was performed and the proteins were digested by incubation with Proteinase K (60 µg/sample) for 1.5 h at 55 °C. RNA extraction was then performed following standard phenol:chloroform phase separation. The protocol is depicted in **Fig. 4A** and detailed in **Supplementary Method 11**.

RNA sequencing, RIP-seq and AS analysis

For the RIP-sequencing, the immunoprecipitated RNA was used as an input into the total RNA library preparation protocol; control input RNA was rRNA depleted using QIAseq Fastselect HMR Kit (Qiagen). For the AS analysis, 200-300 ng total RNA was used as an input into the polyA enrichment module protocol. Samples were fragmented and transcribed into cDNA. Following universal adapter ligation, samples were barcoded using dual indexing primers. Detailed sequencing procedure and analysis are available in the expanded methods section (**Supplementary Method 12 and 13; table S2**).

Individual-nucleotide resolution UV crosslinking and immunoprecipitation (iCLIP) of hnRNPC1/C2

NHDFs were grown to 85-90% confluency and exposed to 150 mJ/cm^2 at 254 nm in a Stratalinker 2400 on ice. Cell pellets were resuspended in 1 ml of ice-cold lysis buffer. The insoluble fraction was removed by centrifugation at 20,000g for 20 min at 4°C and the supernatant was used for the iCLIP experiment. Dynabeads Protein G (Invitrogen) (100 µl/sample) were incubated with 15 µg of anti hnRNPC1/C2 antibody (Santa Cruz) in a total volume of 100 µl of lysis buffer for 1 h at RT. Antibody coupled beads were mixed with 1 ml of soluble cell lysate and incubated for 1 h at 4°C. Dephosphorylation, radiolabeling (γ-ATP) and 3' end adapter ligation was carried out on the protein-RNA complex. The resultant protein-RNA complex was resolved on a gradient NuPAGE gel and blotted onto nitrocellulose membrane. Post-autoradiography the membrane was cut between 48-100 kDa size and Proteinase K treatment was performed to isolate RNA. The cDNA libraries were prepared as previously described *(73)* with slight modifications. Protocol and reagents are detailed in **Supplementary Method 17 and table S2**. A schematic representation of the protocol can be found in **fig. S8A**.

Microscopy and image analysis

Histology, immunohistochemistry and immunocytochemistry are detailed in **Supplementary Method 14**. PLA is detailed in **Supplementary Method 15**. A Zeiss LSM 780 confocal microscope with 40x (1.3 NA) oil-immersion or 20x air (0.8 NA) objective lenses was used for image acquisition. ImageJ and Imaris software were used for image quantification (**Supplementary Method 16**). Super-resolution imaging was performed using a 3D-SIM Deltavision OMX with a 60x objective (1.42 NA).

Statistical Analyses

All data are expressed as the mean ± standard deviation (S.D.) unless otherwise specified. The statistical analyses were performed by using GraphPad Prism v. 6.0 software package. The null hypothesis was rejected when $P < 0.05$. The number of biological (N) and technical (n) replicates and the statistical tests used are indicated in figure legends and in the **data file S10**.

List of the Supplementary Materials

Materials and Methods

Figs. S1 to S12

Tables S1 to S2

Data files S1 to S10

Uncropped Gels

MDAR Reproducibility Checklist

References

1. L. Smith, S. Cho, D. E. Discher, Mechanosensing of matrix by stem cells: From matrix heterogeneity, contractility, and the nucleus in pore-migration to cardiogenesis and muscle stem cells in vivo, *Semin. Cell Dev. Biol.* **71**, 84–98 (2017).

2. F. Martino, A. R. Perestrelo, V. Vinarský, S. Pagliari, G. Forte, Cellular mechanotransduction: From tension to function, *Front. Physiol.* **9**, 1–21 (2018).

3. H. E. Kim, S. S. Dalal, E. Young, M. J. Legato, M. L. Weisfeldt, J. D'Armiento, Disruption of the myocardial extracellular matrix leads to cardiac dysfunction, *J. Clin. Invest.* **106**, 857–866 (2000).

4. M. W. Parker, D. Rossi, M. Peterson, K. Smith, K. Sikström, E. S. White, J. E. Connett, C. A. Henke, O. Larsson, P. B. Bitterman, Fibrotic extracellular matrix activates a profibrotic positive feedback loop, *J. Clin. Invest.* **124**, 1622–1635 (2014).

5. F. G. Spinale, Myocardial matrix remodeling and the matrix metalloproteinases: Influence on cardiac form and function, *Physiol. Rev.* **87**, 1285–1342 (2007).

6. J. J. Saucerman, P. M. Tan, K. S. Buchholz, A. D. McCulloch, J. H. Omens, Mechanical regulation of gene expression in cardiac myocytes and fibroblasts, *Nat. Rev. Cardiol.* **16**, 361–378 (2019).

7. H. Taegtmeyer, S. Sen, D. Vela, Return to the fetal gene program: A suggested metabolic link to gene expression in the heart, *Ann. N. Y. Acad. Sci.* **1188**, 191–198 (2010).

8. R. Papait, P. Cattaneo, P. Kunderfranco, C. Greco, P. Carullo, A. Guffanti, V. Viganò, G. G. Stirparo, M. V. G. Latronico, G. Hasenfuss, J. Chen, G. Condorelli, Genome-wide analysis of histone marks identifying an epigenetic signature of promoters and enhancers underlying cardiac hypertrophy, *Proc. Natl. Acad. Sci. U. S. A.* **110**, 20164–20169 (2013).

9. S. Nomura, M. Satoh, T. Fujita, T. Higo, T. Sumida, T. Ko, T. Yamaguchi, T. Tobita, A. T. Naito, M. Ito, K. Fujita, M. Harada, H. Toko, Y. Kobayashi, K. Ito, E. Takimoto, H. Akazawa, H. Morita, H. Aburatani, I. Komuro, Cardiomyocyte gene programs encoding morphological and functional signatures in cardiac hypertrophy and failure, *Nat. Commun.* **9**, 1–17 (2018).

10. E. N. Olson, M. D. Schneider, Sizing up the heart: Development redux in disease, *Genes Dev.* **17**, 1937–1956 (2003).

11. C. Gao, Y. Wang, mRNA Metabolism in Cardiac Development and Disease: Life After Transcription, *Physiol. Rev.* **100**, 673–694 (2020).

12. A. Beqqali, Alternative splicing in cardiomyopathy, *Biophys. Rev.* **10**, 1061–1071 (2018).

13. T. Geuens, D. Bouhy, V. Timmerman, The hnRNP family: insights into their role in health and disease, *Hum. Genet.* **135**, 851–867 (2016).

14. M. Backlund, F. Stein, M. Rettel, T. Schwarzl, J. I. Perez-Perri, A. Brosig, Y. Zhou, G. Neu-Yilik, M. W. Hentze, A. E. Kulozik, Plasticity of nuclear and cytoplasmic stress responses of RNA-binding proteins, *Nucleic Acids Res.* **48**, 4725–4740 (2020).

15. J. Y. Seo, D. Y. Kim, S. H. Kim, H. J. Kim, H. G. Ryu, J. Lee, K. H. Lee, K. T. Kim, Heterogeneous nuclear ribonucleoprotein (hnRNP) L promotes DNA damage-induced cell apoptosis by enhancing the translation of p53, *Oncotarget* **8**, 51108–51122 (2017).

16. M. C. Lechler, D. C. David, More stressed out with age? Check your RNA granule aggregation, *Prion* **11**, 313–322 (2017).

17. H. Liu, L. Tang, Mechano-Regulation of Alternative Splicing, *Curr. Genomics* **14**, 49–55 (2013).

18. L. J. Simpson, J. S. Reader, E. Tzima, Mechanical Regulation of Protein Translation in the Cardiovascular System, *Front. Cell Dev. Biol.* **8**, 1–13 (2020).

19. T. Wang, S. Hamilla, M. Cam, H. Aranda-Espinoza, S. Mili, Extracellular matrix stiffness and cell contractility control RNA localization to promote cell migration, *Nat. Commun.* **8** (2017), doi:10.1038/s41467-017-00884-y.

20. F. Bordeleau, J. P. Califano, Y. L. N. Abril, B. N. Mason, D. J. LaValley, S. J. Shin, R. S. Weiss, C. A. Reinhart-King, K. S. Anseth, Tissue stiffness regulates serine/arginine-rich protein-mediated splicing of the extra domain B-fibronectin isoform in tumors, *Proc. Natl. Acad. Sci. U. S. A.* **112**, 8314–8319 (2015).

21. W. J. Rhee, C. W. Ni, Z. Zheng, K. Chang, H. Jo, G. Bao, HuR regulates the expression of stress-sensitive genes and mediates inflammatory response in human umbilical vein endothelial cells, *Proc. Natl. Acad. Sci. U. S. A.* **107**, 6858–6863 (2010).

22. J. König, K. Zarnack, G. Rot, T. Curk, M. Kayikci, B. Zupan, D. J. Turner, N. M. Luscombe, J. Ule, ICLIP reveals the function of hnRNP particles in splicing at individual nucleotide resolution, *Nat. Struct. Mol. Biol.* **17**, 909–915 (2010).

23. K. Zarnack, J. König, M. Tajnik, I. Martincorena, S. Eustermann, I. Stévant, A. Reyes, S. Anders, N. M. Luscombe, J. Ule, Direct competition between hnRNP C and U2AF65 protects the transcriptome from the exonization of Alu elements, *Cell* **152**, 453–466 (2013).

24. R. Zhou, J. W. Park, R. F. Chun, T. S. Lisse, A. J. Garcia, K. Zavala, J. L. Sea, Z. X. Lu, J. Xu, J. S. Adams, Y. Xing, M. Hewison, Concerted effects of heterogeneous nuclear ribonucleoprotein C1/C2 to control vitamin D-directed gene transcription and RNA splicing in human bone cells, *Nucleic Acids Res.* **45**, 606–618 (2017).

25. A. Borreca, K. Gironi, G. Amadoro, M. Ammassari-Teule, Opposite Dysregulation of Fragile-X Mental Retardation Protein and Heteronuclear Ribonucleoprotein C Protein Associates with Enhanced APP Translation in Alzheimer Disease, *Mol. Neurobiol.* **53**, 3227–3234 (2016).

26. H. Fischl, J. Neve, Z. Wang, R. Patel, A. Louey, B. Tian, A. Furger, hnRNPC regulates cancer-specific alternative cleavage and polyadenylation profiles, *Nucleic Acids Res.* **47**, 7580–7591 (2019).

27. M. P. Panchenko, N. Silva, J. R. Stone, Up-regulation of a hydrogen peroxide-responsive pre-mRNA binding protein in atherosclerosis and intimal hyperplasia, *Cardiovasc. Pathol.* **18**, 167–172 (2009).

28. M. M. Gladka, B. Molenaar, H. de Ruiter, S. van der Elst, H. Tsui, D. Versteeg, G. P. A. Lacraz, M. M. H. Huibers, A. van Oudenaarden, E. van Rooij, Single-Cell Sequencing of the Healthy and Diseased Heart Reveals Cytoskeleton-Associated Protein 4 as a New Modulator of Fibroblasts Activation, *Circulation* **138**, 166–180 (2018).

29. T. Heallen, M. Zhang, J. Wang, M. Bonilla-Claudio, E. Klysik, R. L. Johnson, J. F. Martin, Hippo Pathway Inhibits Wnt Signaling to Restrain Cardiomyocyte Proliferation and Heart Size, *Science (80-.).* **332**, 458–461 (2011).

30. A. R. Perestrelo, A. C. Silva, J. Oliver-De La Cruz, F. Martino, V. Horváth, G. Caluori, O. Polanský,

V. Vinarský, G. Azzato, G. de Marco, V. Žampachová, P. Skládal, S. Pagliari, A. Rainer, P. Pinto-do-Ó, A. Caravella, K. Koci, D. S. Nascimento, G. Forte, Multiscale Analysis of Extracellular Matrix Remodeling in the Failing Heart, *Circ. Res.* **128**, 24–38 (2021).

31. M. H. Harpster, S. Bandyopadhyay, D. P. Thomas, P. S. Ivanov, J. A. Keele, N. Pineguina, B. Gao, V. Amarendran, M. Gomelsky, R. J. McCormick, M. M. Stayton, Earliest changes in the left ventricular transcriptome postmyocardial infarction, *Mamm. Genome* **17**, 701–715 (2006).

32. A. S. Barth, R. Kuner, A. Buness, M. Ruschhaupt, S. Merk, L. Zwermann, S. Kääb, E. Kreuzer, G. Steinbeck, U. Mansmann, A. Poustka, M. Nabauer, H. Sültmann, Identification of a Common Gene Expression Signature in Dilated Cardiomyopathy Across Independent Microarray Studies, *J. Am. Coll. Cardiol.* **48**, 1610–1617 (2006).

33. D. Colak, N. Kaya, J. Al-Zahrani, A. Al Bakheet, P. Muiya, E. Andres, J. Quackenbush, N. Dzimiri, Left ventricular global transcriptional profiling in human end-stage dilated cardiomyopathy, *Genomics* **94**, 20–31 (2009).

34. J. Rowell, N. Koitabashi, D. A. Kass, A. S. Barth, Dynamic gene expression patterns in animal models of early and late heart failure reveal biphasic-bidirectional transcriptional activation of signaling pathways, *Physiol. Genomics* **46**, 779–787 (2014).

35. W. Liebermeister, E. Noor, A. Flamholz, D. Davidi, J. Bernhardt, R. Milo, Visual account of protein investment in cellular functions, *Proc. Natl. Acad. Sci. U. S. A.* **111**, 8488–8493 (2014).

36. D. S. Nascimento, M. Valente, T. Esteves, M. de Fátima de Pina, J. G. Guedes, A. Freire, P. Quelhas, P. Pinto-do-Ó, MIQuant - semi-automation of infarct size assessment in models of cardiac ischemic injury, *PLoS One* **6** (2011), doi:10.1371/journal.pone.0025045.

37. Y. Zhu, G. Xu, Y. T. Yang, Z. Xu, X. Chen, B. Shi, D. Xie, Z. J. Lu, P. Wang, POSTAR2: Deciphering the post-Transcriptional regulatory logics, *Nucleic Acids Res.* **47**, D203–D211 (2019).

38. H. Dvinge, Regulation of alternative <scp>mRNA</scp> splicing: old players and new perspectives, *FEBS Lett.* **592**, 2987–3006 (2018).

39. H. Cheng, M. Zheng, A. K. Peter, K. Kimura, X. Li, K. Ouyang, T. Shen, L. Cui, D. Frank, N. D. Dalton, Y. Gu, N. Frey, K. L. Peterson, S. M. Evans, K. U. Knowlton, F. Sheikh, J. Chen, Selective deletion of long but not short cypher isoforms leads to late-onset dilated cardiomyopathy, *Hum. Mol. Genet.* **20**, 1751–1762 (2011).

40. W. Guo, S. Schafer, M. L. Greaser, M. H. Radke, M. Liss, T. Govindarajan, H. Maatz, H. Schulz, S. Li, A. M. Parrish, V. Dauksaite, P. Vakeel, S. Klaassen, B. Gerull, L. Thierfelder, V. Regitz-Zagrosek, T. a Hacker, K. W. Saupe, G. W. Dec, P. T. Ellinor, C. A. MacRae, B. Spallek, R. Fischer, A. Perrot, C. Özcelik, K. Saar, N. Hubner, M. Gotthardt, RBM20, a gene for hereditary cardiomyopathy, regulates titin splicing, *Nat. Med.* **18**, 766–773 (2012).

41. C. Zhu, Z. Chen, W. Guo, Pre-mRNA mis-splicing of sarcomeric genes in heart failure, *Biochim. Biophys. Acta - Mol. Basis Dis.* **1863**, 2056–2063 (2017).

42. A. G. Cadar, L. Zhong, A. Lin, M. O. Valenzuela, C. C. Lim, Upstream open reading frame in 5'-untranslated region reduces titin mRNA translational efficiency, *Biochem. Biophys. Res. Commun.* **453**, 185–191 (2014).

43. Y. E. Lewis, A. Moskovitz, M. Mutlak, J. Heineke, L. H. Caspi, I. Kehat, Localization of transcripts, translation, and degradation for spatiotemporal sarcomere maintenance, *J. Mol. Cell. Cardiol.* **116**, 16–28 (2018).

44. D. C. Zarnescu, C. C. Gregorio, Fragile hearts: New insights into translational control in cardiac muscle, *Trends Cardiovasc. Med.* **23**, 275–281 (2013).

45. T. H. Larsen, J. E. Hesketh, S. Rotevatn, G. Greve, T. Sætersdal, Ribosome distribution in normal and infarcted rat hearts, *Histochem. J.* **26**, 79–89 (1994).

46. X. Lian, C. Hsiao, G. Wilson, K. Zhu, L. B. Hazeltine, S. M. Azarin, K. K. Raval, J. Zhang, T. J. Kamp, S. P. Palecek, Robust cardiomyocyte differentiation from human pluripotent stem cells via temporal modulation of canonical Wnt signaling, *Proc. Natl. Acad. Sci. U. S. A.* **109** (2012), doi:10.1073/pnas.1200250109.

47. K. E. Sullivan, K. P. Quinn, K. M. Tang, I. Georgakoudi, L. D. Black, Extracellular matrix remodeling following myocardial infarction influences the therapeutic potential of mesenchymal stem cells, *Stem Cell Res. Ther.* **5**, 0–15 (2014).

48. S. Dupont, L. Morsut, M. Aragona, E. Enzo, S. Giulitti, M. Cordenonsi, F. Zanconato, J. Le Digabel, M. Forcato, S. Bicciato, N. Elvassore, S. Piccolo, Role of YAP/TAZ in mechanotransduction, *Nature* **474**, 179–184 (2011).

49. G. Nardone, J. Oliver-De La Cruz, J. Vrbsky, C. Martini, J. Pribyl, P. Skládal, M. Pešl, G. Caluori, S. Pagliari, F. Martino, Z. Maceckova, M. Hajduch, A. Sanz-Garcia, N. M. Pugno, G. B. Stokin, G. Forte, YAP regulates cell mechanics by controlling focal adhesion assembly, *Nat. Commun.* **8** (2017), doi:10.1038/ncomms15321.

50. J. Oliver-De La Cruz, G. Nardone, J. Vrbsky, A. Pompeiano, A. R. Perestrelo, F. Capradossi, K. Melajová, P. Filipensky, G. Forte, Substrate mechanics controls adipogenesis through YAP phosphorylation by dictating cell spreading, *Biomaterials* **205**, 64–80 (2019).

51. H. Duong, B. Wu, B. Tawil, Modulation of 3D fibrin matrix stiffness by intrinsic fibrinogen-thrombin compositions and by extrinsic cellular activity, *Tissue Eng. - Part A* **15**, 1865–1876 (2009).

52. D. Mosqueira, S. Pagliari, K. Uto, M. Ebara, S. Romanazzo, C. Escobedo-Lucea, J. Nakanishi, A. Taniguchi, O. Franzese, P. Di Nardo, M. J. Goumans, E. Traversa, P. Pinto-Do-Ó, T. Aoyagi, G. Forte, Hippo pathway effectors control cardiac progenitor cell fate by acting as dynamic sensors of substrate mechanics and nanostructure, *ACS Nano* **8**, 2033–2047 (2014).

53. E. N. Olson, A. Nordheim, Linking actin dynamics and gene transcription to drive cellular motile functions, *Nat. Rev. Mol. Cell Biol.* **11**, 353–365 (2010).

54. S. S. Palaniyandi, L. Sun, J. C. B. Ferreira, D. Mochly-Rosen, Protein kinase C in heart failure: a therapeutic target?, *Cardiovasc. Res.* **82**, 229–239 (2008).

55. J. P. Venables, C.-S. Koh, U. Froehlich, E. Lapointe, S. Couture, L. Inkel, A. Bramard, É. R. Paquet, V. Watier, M. Durand, J.-F. Lucier, J. Gervais-Bird, K. Tremblay, P. Prinos, R. Klinck, S. A. Elela, B. Chabot, Multiple and Specific mRNA Processing Targets for the Major Human hnRNP Proteins, *Mol. Cell. Biol.* **28**, 6033–6043 (2008).

56. D. P. Del Re, Y. Yang, N. Nakano, J. Cho, P. Zhai, T. Yamamoto, N. Zhang, N. Yabuta, H. Nojima, D. Pan, J. Sadoshima, Yes-associated protein isoform 1 (Yapl) promotes cardiomyocyte survival and growth to protect against myocardial ischemic injury, *J. Biol. Chem.* **288**, 3977–3988 (2013).

57. J. Vrbský, V. Vinarský, A. R. Perestrelo, J. O. De La Cruz, F. Martino, A. Pompeiano, V. Izzi, O. Hlinomaz, V. Rotrekl, M. Sudol, S. Pagliari, G. Forte, Evidence for discrete modes of YAP1 signaling via mRNA splice isoforms in development and diseases, *Genomics* , 135907 (2021).

58. K. E. Keller, M. J. Kelley, T. S. Acott, Extracellular matrix gene alternative splicing by trabecular

meshwork cells in response to mechanical stretching, *Investig. Ophthalmol. Vis. Sci.* **48**, 1164–1172 (2007).

59. F. Yang, F. Yi, X. Han, Q. Du, Z. Liang, MALAT-1 interacts with hnRNP C in cell cycle regulation, *FEBS Lett.* **587**, 3175–3181 (2013).

60. L. Schirone, M. Forte, S. Palmerio, D. Yee, C. Nocella, F. Angelini, F. Pagano, S. Schiavon, A. Bordin, A. Carrizzo, C. Vecchione, V. Valenti, I. Chimenti, E. De Falco, S. Sciarretta, G. Frati, A Review of the Molecular Mechanisms Underlying the Development and Progression of Cardiac Remodeling, *Oxid. Med. Cell. Longev.* **2017**, 1–16 (2017).

61. H. Huang, Y. Han, C. Zhang, J. Wu, J. Feng, L. Qu, C. Shou, HNRNPC as a candidate biomarker for chemoresistance in gastric cancer, *Tumor Biol.* **37**, 3527–3534 (2016).

62. G. Neubauer, A. King, J. Rappsilber, C. Calvio, M. Watson, P. Ajuh, J. Sleeman, A. Lamond, M. Mann, Mass spectrometry and EST-database searching allows characterization of the multi-protein spliceosome complex, *Nat. Genet.* **20**, 46–50 (1998).

63. D. E. Willis, E. A. Van Niekerk, Y. Sasaki, M. Mesngon, T. T. Merianda, G. G. Williams, M. Kendall, D. S. Smith, G. J. Bassell, J. L. Twiss, Extracellular stimuli specifically regulate localized levels of individual neuronal mRNAs, *J. Cell Biol.* **178**, 965–980 (2007).

64. J. B. Lawrence, R. H. Singer, Intracellular localization of messenger RNAs for cytoskeletal proteins, *Cell* **45**, 407–415 (1986).

65. A. J. Rodriguez, S. M. Shenoy, R. H. Singer, J. Condeelis, Visualization of mRNA translation in living cells, *J. Cell Biol.* **175**, 67–76 (2006).

66. F. Angenstein, A. M. Evans, S. C. Ling, R. E. Settlage, S. Ficarro, F. A. Carrero-Martinez, J.

Shabanowitz, D. F. Hunt, W. T. Greenough, Proteomic characterization of messenger ribonucleoprotein complexes bound to nontranslated or translated poly(A) mRNAs in the rat cerebral cortex, *J. Biol. Chem.* **280**, 6496–6503 (2005).

67. D. Dysregulation, A. Velázquez-cruz, B. Baños-jaime, A. Díaz-quintana, M. A. De Rosa, I. Díaz-moreno, Post-translational Control of RNA-Binding Proteins and, **8**, 1–15 (2021).

68. D. Ladage, L. Tilemann, K. Ishikawa, R. N. Correll, Y. Kawase, S. R. Houser, J. D. Molkentin, R. J. Hajjar, Inhibition of PKCα/β With Ruboxistaurin Antagonizes Heart Failure in Pigs After Myocardial Infarction Injury, *Circ. Res.* **109**, 1396–1400 (2011).

69. K. A. Connelly, D. J. Kelly, Y. Zhang, D. L. Prior, A. Advani, A. J. Cox, K. Thai, H. Krum, R. E. Gilbert, Inhibition of Protein Kinase C–β by Ruboxistaurin Preserves Cardiac Function and Reduces Extracellular Matrix Production in Diabetic Cardiomyopathy, *Circ. Hear. Fail.* **2**, 129–137 (2009).

70. F. D. Camargo, S. Gokhale, J. B. Johnnidis, D. Fu, G. W. Bell, R. Jaenisch, T. R. Brummelkamp, YAP1 Increases Organ Size and Expands Undifferentiated Progenitor Cells, *Curr. Biol.* **17**, 2054–2060 (2007).

71. N. Hou, Y. Wen, X. Yuan, H. Xu, X. Wang, F. Li, B. Ye, Activation of Yap1/Taz signaling in ischemic heart disease and dilated cardiomyopathy, *Exp. Mol. Pathol.* **103**, 267–275 (2017).

72. M. Müller-Mcnicoll, O. Rossbach, J. Hui, J. Medenbach, Auto-regulatory feedback by RNA-binding proteins, *J. Mol. Cell Biol.* **11**, 930–939 (2019).

73. J. Konig, K. Zarnack, G. Rot, T. Curk, M. Kayikci, B. Zupan, D. J. Turner, N. M. Luscombe, J. Ule, iCLIP - Transcriptome-wide Mapping of Protein-RNA Interactions with Individual Nucleotide Resolution, *J. Vis. Exp.* , 2–8 (2011).

74. A. C. Silva, S. C. Rodrigues, J. Caldeira, A. M. Nunes, V. Sampaio-Pinto, T. P. Resende, M. J. Oliveira, M. A. Barbosa, S. Thorsteinsdóttir, D. S. Nascimento, P. Pinto-do-Ó, Three-dimensional scaffolds of fetal decellularized hearts exhibit enhanced potential to support cardiac cells in comparison to the adult, *Biomaterials* **104**, 52–64 (2016).

75. J. R. Wiśniewski, A. Zougman, N. Nagaraj, M. Mann, Universal sample preparation method for proteome analysis, *Nat. Methods* **6**, 359–362 (2009).

76. A. Otto, J. Bernhardt, H. Meyer, M. Schaffer, F. A. Herbst, J. Siebourg, U. Mäder, M. Lalk, M. Hecker, D. Becher, Systems-wide temporal proteomic profiling in glucose-starved Bacillus subtilis, *Nat. Commun.* **1** (2010), doi:10.1038/ncomms1137.

77. F. Fiorini, F. Bonneau, H. Le Hir, in *Bio-Protocol*, (2012), vol. 8, pp. 255–274.

78. A. David, B. P. Dolan, H. D. Hickman, J. J. Knowlton, G. Clavarino, P. Pierre, J. R. Bennink, J. W. Yewdell, Nuclear translation visualized by ribosome-bound nascent chain puromycylation, *J. Cell Biol.* **197**, 45–57 (2012).

79. Y. Wu, W. Zhao, Y. Liu, X. Tan, X. Li, Q. Zou, Z. Xiao, H. Xu, Y. Wang, X. Yang, Function of HNRNPC in breast cancer cells by controlling the dsRNA-induced interferon response, *EMBO J.* **37**, 1–19 (2018).

80. S. Andrews, FastQC: a quality control tool for high throughput sequence data., *Available online at: http://www.bioinformatics.babraham.ac.uk/projects/fastqc* (2010), doi:10.1038/nrm2548.

81. A. M. Bolger, M. Lohse, B. Usadel, Trimmomatic: A flexible trimmer for Illumina sequence data, *Bioinformatics* **30**, 2114–2120 (2014).

82. A. Dobin, C. A. Davis, F. Schlesinger, J. Drenkow, C. Zaleski, S. Jha, P. Batut, M. Chaisson, T. R.

Gingeras, STAR: Ultrafast universal RNA-seq aligner, *Bioinformatics* **29**, 15–21 (2013).

83. L. Wang, S. Wang, W. Li, RSeQC: Quality control of RNA-seq experiments, *Bioinformatics* **28**, 2184–2185 (2012).

84. K. Okonechnikov, A. Conesa, F. García-Alcalde, Qualimap 2: Advanced multi-sample quality control for high-throughput sequencing data, *Bioinformatics* **32**, 292–294 (2016).

85. S. W. Wingett, S. Andrews, Fastq screen: A tool for multi-genome mapping and quality control [version 1; referees: 3 approved, 1 approved with reservations], *F1000Research* **7**, 1–13 (2018).

86. Y. Liao, G. K. Smyth, W. Shi, FeatureCounts: An efficient general purpose program for assigning sequence reads to genomic features, *Bioinformatics* **30**, 923–930 (2014).

87. H. Wickham, Ggplot2, *Wiley Interdiscip. Rev. Comput. Stat.* **3**, 180–185 (2011).

88. J. Lemon, Package ‘ plotrix ,’ *R-news 6.4* , 8–12 (2006).

89. S. Shen, J. W. Park, Z. X. Lu, L. Lin, M. D. Henry, Y. N. Wu, Q. Zhou, Y. Xing, rMATS: Robust and flexible detection of differential alternative splicing from replicate RNA-Seq data, *Proc. Natl. Acad. Sci. U. S. A.* **111**, E5593–E5601 (2014).

90. G. Yu, L. G. Wang, Y. Han, Q. Y. He, ClusterProfiler: An R package for comparing biological themes among gene clusters, *Omi. A J. Integr. Biol.* **16**, 284–287 (2012).

91. E. Y. Chen, C. M. Tan, Y. Kou, Q. Duan, Z. Wang, G. V. Meirelles, N. R. Clark, A. Ma’ayan, Enrichr: Interactive and collaborative HTML5 gene list enrichment analysis tool, *BMC Bioinformatics* **14** (2013), doi:10.1186/1471-2105-14-128.

92. M. V. Kuleshov, M. R. Jones, A. D. Rouillard, N. F. Fernandez, Q. Duan, Z. Wang, S. Koplev, S. L.

Jenkins, K. M. Jagodnik, A. Lachmann, M. G. McDermott, C. D. Monteiro, G. W. Gundersen, A. Ma'ayan, Enrichr: a comprehensive gene set enrichment analysis web server 2016 update, *Nucleic Acids Res.* **44**, W90–W97 (2016).

93. P. Shannon, Cytoscape: A Software Environment for Integrated Models of Biomolecular Interaction Networks, *Genome Res.* **13**, 2498–2504 (2003).

94. G. Bindea, B. Mlecnik, H. Hackl, P. Charoentong, M. Tosolini, A. Kirilovsky, W. H. Fridman, F. Pagès, Z. Trajanoski, J. Galon, ClueGO: A Cytoscape plug-in to decipher functionally grouped gene ontology and pathway annotation networks, *Bioinformatics* **25**, 1091–1093 (2009).

95. G. Bindea, J. Galon, B. Mlecnik, CluePedia Cytoscape plugin: Pathway insights using integrated experimental and in silico data, *Bioinformatics* **29**, 661–663 (2013).

96. D. N. Slenter, M. Kutmon, K. Hanspers, A. Riutta, J. Windsor, N. Nunes, J. Mélius, E. Cirillo, S. L. Coort, D. DIgles, F. Ehrhart, P. Giesbertz, M. Kalafati, M. Martens, R. Miller, K. Nishida, L. Rieswijk, A. Waagmeester, L. M. T. Eijssen, C. T. Evelo, A. R. Pico, E. L. Willighagen, WikiPathways: A multifaceted pathway database bridging metabolomics to other omics research, *Nucleic Acids Res.* **46**, D661–D667 (2018).

97. M. Kanehisa, Y. Sato, KEGG Mapper for inferring cellular functions from protein sequences, *Protein Sci.* **29**, 28–35 (2020).

98. A. P. Davis, C. J. Grondin, R. J. Johnson, D. Sciaky, R. McMorran, J. Wiegers, T. C. Wiegers, C. J. Mattingly, The Comparative Toxicogenomics Database: Update 2019, *Nucleic Acids Res.* **47**, D948–D954 (2019).

99. A. Obrdlik, G. Lin, N. Haberman, J. Ule, A. Ephrussi, The Transcriptome-wide Landscape and

Modalities of EJC Binding in Adult Drosophila, *Cell Rep.* **28**, 1219-1236.e11 (2019).

100. T. Smith, A. Heger, I. Sudbery, UMI-tools: Modeling sequencing errors in Unique Molecular Identifiers to improve quantification accuracy, *Genome Res.* **27**, 491–499 (2017).

101. F. Ramírez, D. P. Ryan, B. Grüning, V. Bhardwaj, F. Kilpert, A. S. Richter, S. Heyne, F. Dündar, T. Manke, deepTools2: a next generation web server for deep-sequencing data analysis, *Nucleic Acids Res.* **44**, W160–W165 (2016).

102. J. T. Robinson, H. Thorvaldsdóttir, W. Winckler, M. Guttman, E. S. Lander, G. Getz, J. P. Mesirov, Integrative genomics viewer, *Nat. Biotechnol.* **29**, 24–26 (2011).

103. A. R. Quinlan, I. M. Hall, BEDTools: A flexible suite of utilities for comparing genomic features, *Bioinformatics* **26**, 841–842 (2010).

104. M. E. Pepin, C. M. Ha, D. K. Crossman, S. H. Litovsky, S. Varambally, J. P. Barchue, S. V. Pamboukian, N. A. Diakos, S. G. Drakos, S. M. Pogwizd, A. R. Wende, Genome-wide DNA methylation encodes cardiac transcriptional reprogramming in human ischemic heart failure, *Lab. Investig.* **99**, 371–386 (2019).

105. A. Karystinou, A. J. Roelofs, A. Neve, F. P. Cantatore, H. Wackerhage, C. De Bari, Yes-associated protein (YAP) is a negative regulator of chondrogenesis in mesenchymal stem cells, *Arthritis Res. Ther.* **17**, 1–14 (2015).

106. H. Miao, A. W. Crabb, M. R. Hernandez, T. J. Lukas, Modulation of factors affecting optic nerve head astrocyte migration, *Investig. Ophthalmol. Vis. Sci.* **51**, 4096–4103 (2010).

107. H. Arafat, M. Lazar, K. Salem, G. Chipitsyna, Q. Gong, T. C. Pan, R. Z. Zhang, C. J. Yeo, M. L. Chu, Tumor-specific expression and alternative splicing of the COL6A3 gene in pancreatic cancer,

Surgery **150**, 306–315 (2011).

108. C. A. Schneider, W. S. Rasband, K. W. Eliceiri, NIH Image to ImageJ: 25 years of image analysis, *Nat. Methods* **9**, 671–675 (2012).

109. Xinglab, Actin-associated hnRNP proteins as transacting factors in the control of mRNA transport and localization, *Available online at: https://github.com/Xinglab/rmats2sashimiplot* , doi:10.4161/rna.6.2.8195.

Acknowledgements

The authors would like to thank Carina Sihlbom and Johannes Fuchs at the Proteomics Core Facility at Sahlgrenska Academy, University of Gothenburg, Sweden for proteomic analysis. They also thank the technical support team at the Center of Translational Medicine, the members of the Mass Spectrometry Core Facility of FNUSA-ICRC, the Core Facility Bioinformatics of CEITEC Masaryk University, the CF Genomics supported by the NCLG research infrastructure (LM2018132 funded by MEYS CR), the CELLIM core facility supported by the Czech-BioImaging large RI project (LM2018129 funded by MEYS CR) for their assistance with obtaining the scientific data presented in this paper. The authors are grateful to Jessica Tamanini of Insight Editing London for reviewing and editing the manuscript prior to submission and to Jan Vrbsky for primer design. The authors also thank Perpetua Pinto-do-Ó and Diana S Nascimento for providing the mouse model of MI. Super-resolution microscopy was performed at the Materials Characterization and Fabrication Platform (MCFP) at The University of Melbourne. We thank Ana Silva (anasilvaillustrations.com) for conceptualizing and designing the graphical abstract (**fig. S13**).

Funding: FM was supported by the European Regional Development Fund - Project ENOCH (No. CZ.02.1.01/0.0/0.0/16_019/0000868). ARP, GF, SP were supported by the European Social Fund and

European Regional Development Fund-Project MAGNET (CZ.02.1.01/0.0/0.0/15_003/0000492). FCaruso acknowledges the award of a National Health and Medical Research Council Senior Principal Research Fellowship (GNT1135806). FCavalieri acknowledges the award of an Australian Research Council (ARC) Future Fellowship scheme (FT140100873) and the European Union's Horizon 2020 Research and Innovation Program under grant agreement No. 690901 (NANOSUPREMI). WSA and APG were supported by the BBSRC (BB/N008820/1) and a Royal Society Wolfson Research Merit Award (WM170036) to APG. SV and NMV were supported by the Czech Science Foundation (20-19617S) and the institutional support CEITEC 2020 (LQ1601). DV was supported by GAČR 20-11101S. MOC was supported by the Ministry of Education, Youth and Sports within programme INTER-COST (LTC18052).

Author contributions: FM: Conceptualization, Experimental Design and Execution, manuscript drafting; NMV, SV: iCLIP-sequencing and validation; ARP: Experimental Execution; VHejret: Bioinformatics analysis; HD: Experimental Execution; DV: Experimental Execution; VHorvath: human tissue harvesting and patient anamnesis; FCavalieri, FCaruso: Super-resolution microscopy, manuscript drafting; WSA, APG: RNA-IP protocol setting and data interpretation; MAOC: paper conceptualization and drafting; SP, GF: project supervision, paper conceptualization and drafting.

Competing interests: The authors declare no competing interests.

Data and materials Availability: All data associated with this study are present in the paper or the Supplementary Materials and Methods file. Sequencing data have been deposited to GEO database under the reference series GSE155474 and GSE169068. The Mass Spectrometry proteomics data have been deposited to the ProteomeXchange Consortium via the PRIDE partner repository under the dataset identifier PXD020663.

Figures

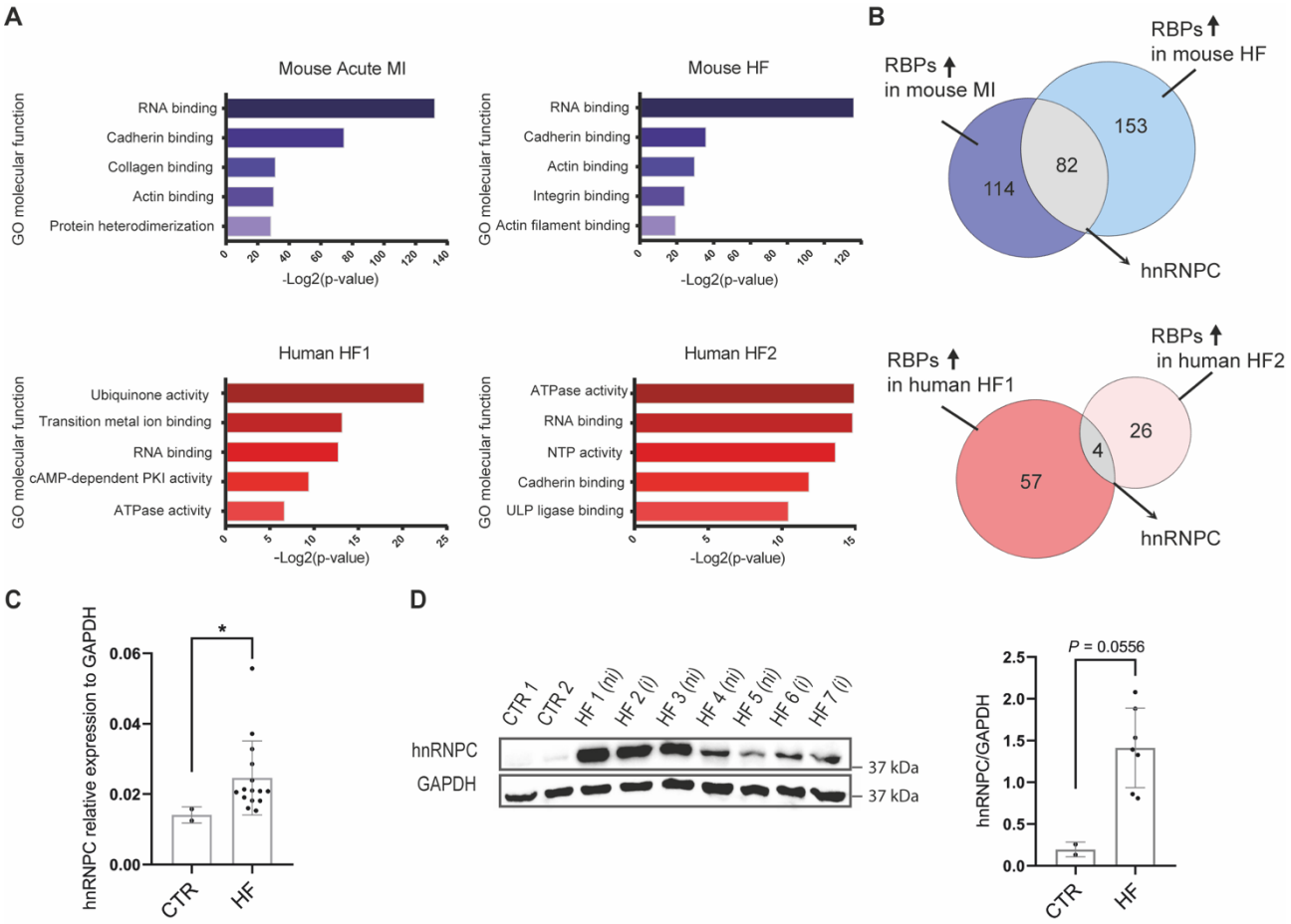

Fig. 1. **The RNA-binding protein hnRNPC is upregulated in the diseased heart.** (**A**) Top: Gene ontology (GO) annotation of the significantly upregulated genes (FDR < 0.1; FC > 1.5) identified by expression profiling array of murine hearts (left ventricle) exposed to myocardial infarction (48 h post-MI) as compared to sham operated (left) and MerCreMer (MCM) murine hearts with peak dysfunction (day 10 post-tamoxifen treatment) as compared to control (right). Bottom: GO annotation of the genes found significantly upregulated by expression profiling array analysis of failing (HF) human heart as compared to healthy human heart in two datasets: HF1 (left) (FDR < 0.05; FC > 1.8) and HF2 (FDR < 0.1; FC > 1.5) (right). (**B**) Top: Genes found upregulated by in silico analysis of profiling array data 48 h post-MI and in HF mouse heart tissues that encode for proteins involved in RNA binding (GO: 0003723). Bottom: Genes found upregulated by in silico analysis of profiling array data of HF1 and HF2 encoding for proteins involved in RNA binding (GO: 0003723). (**C**) RT-qPCR analysis of hnRNPC RNA expression in HF (N = 15; n = 2) compared to healthy human hearts (controls, CTR) (N = 2; n = 2). (**D**) Western blot analysis (left) and relative quantification (right) of hnRNPC protein expression in samples of HF (1-7) (N = 7; n = 3) and healthy control (1-2) (N = 2; n = 3) heart tissues. HF (i) and HF (ni) indicate ischemic and non-ischemic samples, respectively. GAPDH was used for total protein loading normalization. *P < 0.05; p-values were determined by Mann-Whitney test. Data are shown as means ± SD. See also **fig. S1** and **data file S1**.

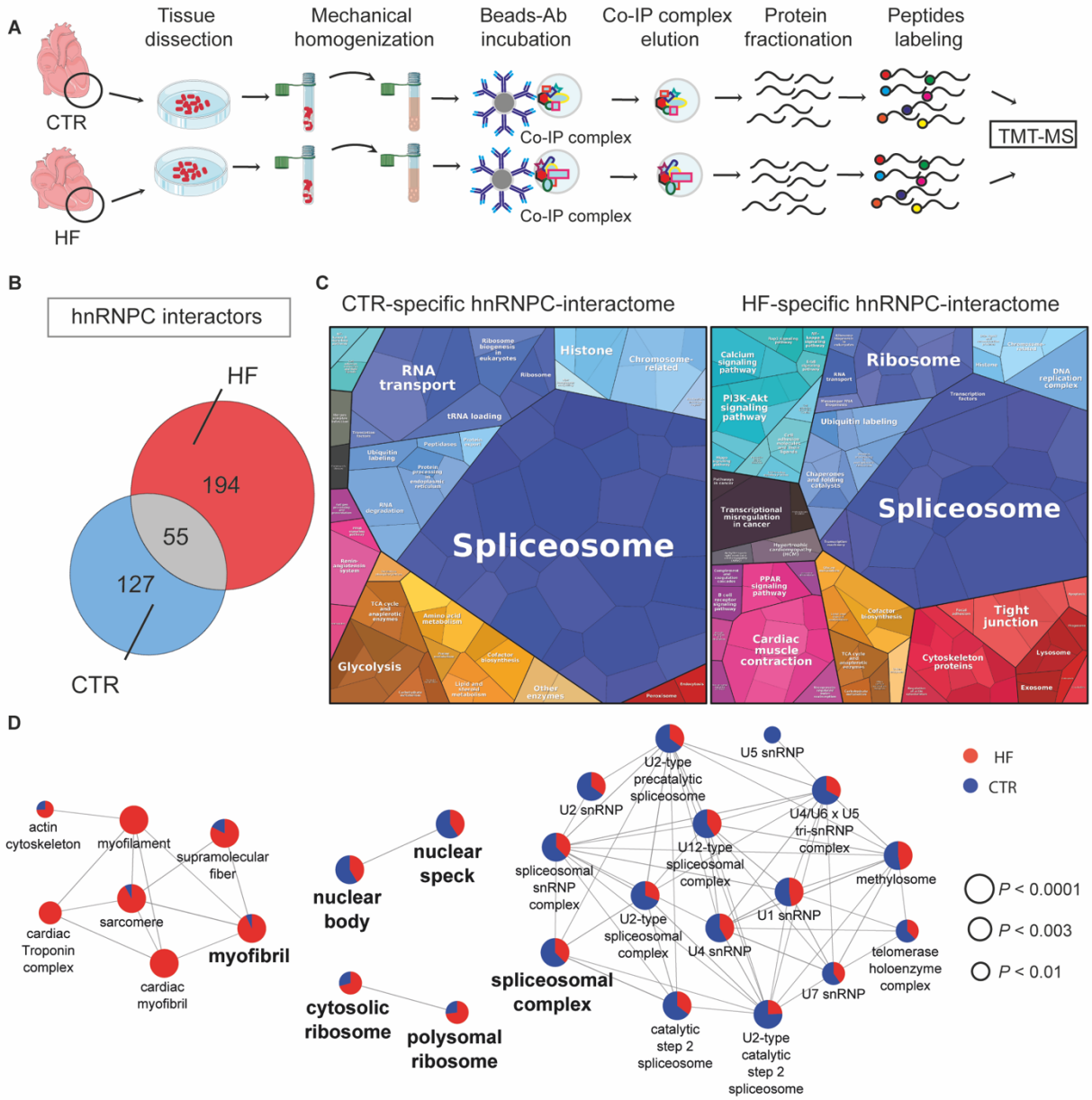

Fig. 2. hnRNPC interacts with components of the myofibril in pathological heart. (**A**) Graphical representation of the strategy adopted to identify hnRNPC interactors in the healthy (CTR) and failing (HF) human heart in vivo by endogenous protein immunoprecipitation followed by tandem mass tag spectrometry (TMT-MS). (**B**) The number of unique and shared proteins found in the hnRNPC interactome in human healthy (CTR) (N=2) and failing (HF) (N=2) heart tissue by TMT-MS. (**C**) Proteomaps (based on the KEGG database) representing the quantitative composition of the hnRNPC interactome in CTR and HF human hearts with a focus on protein function. Proteins are weighted for their abundance in the immunoprecipitated samples. (**D**) Network representation of the cellular components GO categories enriched in the hnRNPC interactome in CTR (blue) and HF (red) heart tissue. The size of the node indicates the Bonferroni adjusted Term p-values. See also **fig. S2** and **data file S2**.

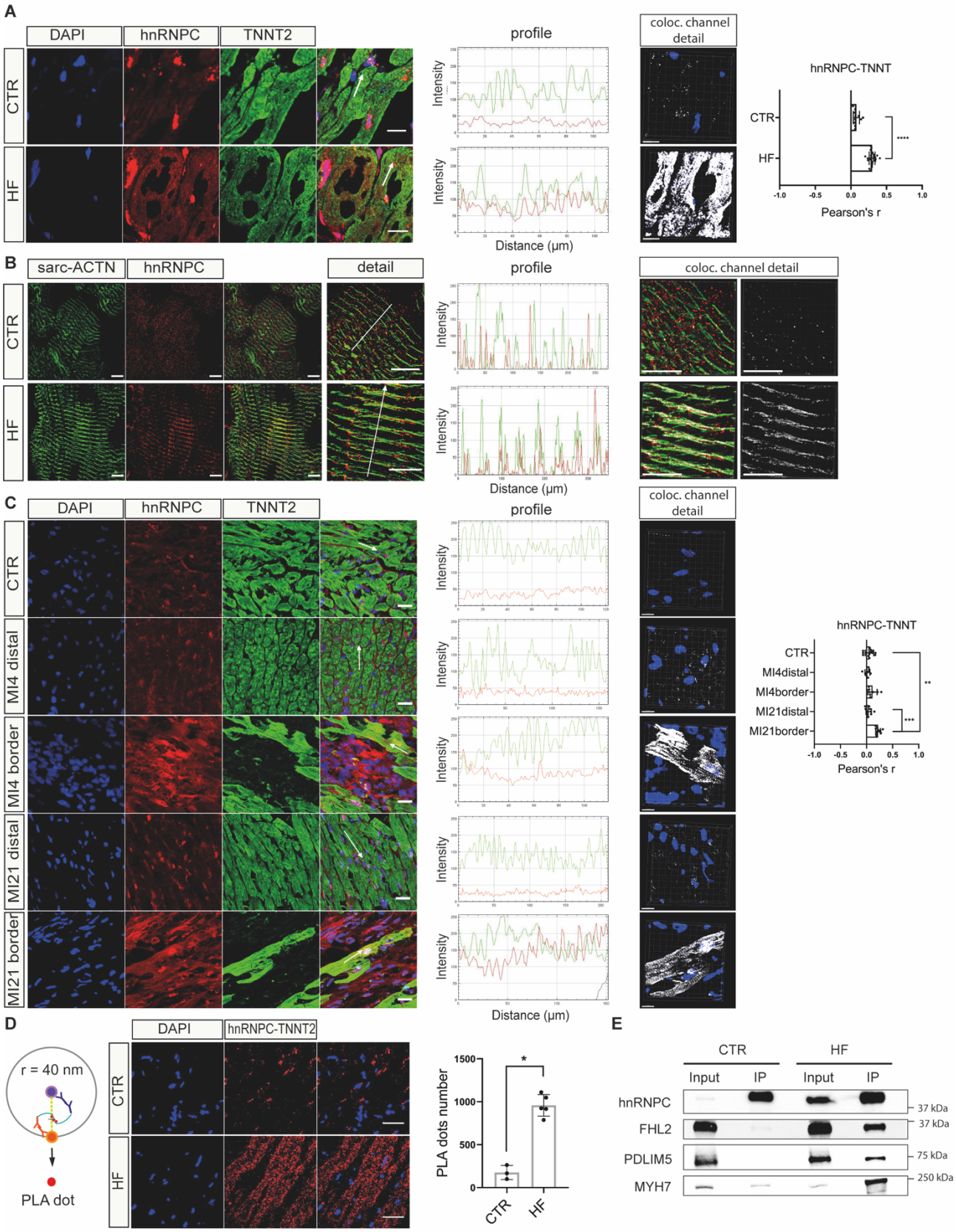

Fig. 3. hnRNPC is localized at the Z-disc of the sarcomere in the pathological heart. (**A**) Representative confocal microscopy images depicting hnRNPC (red) localization in healthy control (N=2) or failing (HF) (N=3) human heart tissue. Cardiomyocytes are stained with cardiac troponin T2 antibody (TNNT2, green) and the nuclei are counterstained with DAPI (blue). The image analysis profile shows hnRNPC (red) distribution across the sarcomere, as identified by TNNT2

staining. The area analyzed is indicated by the white arrow in the microscopic image. The detail shows the colocalization (white) of red and green channels. Pearson's coefficient was calculated by Imaris (n ≥ 11). ****$P < 0.0001$; Mann-Whitney test. Scale bar = 20 μm; Scale bar of detail = 10 μm. (**B**) Representative super-resolution image and image analysis of hnRNPC (red) sarcomeric distribution in failing HF. The sarcomere is counterstained by sarcomeric alpha actinin (sarc-ACTN, green). The area analyzed is indicated by the white arrow in the microscopic image. The detail shows the colocalization (white) of red and green channels. Scale bar = 5 μm. (**C**) Representative confocal images showing the localization and relative profile of hnRNPC (red) in healthy and at the infarction proximity (border zone) or distal areas of infarcted mouse heart 4- and 21-days post-MI. Cardiomyocytes are stained with cardiac troponin T (TNNT2, green) and the nuclei are counterstained with DAPI (blue). The area analyzed is indicated by the white arrow in the microscopic image. The detail shows the colocalization (white) of red and green channels. Pearson's coefficient was calculated by Imaris (n ≥ 8). *** $P < 0.001$; ** $P < 0.01$; Mann-Whitney test. Scale bar = 10 μm. (**D**) Representative confocal images and relative quantification of the results obtained from Proximity Ligation Assay (PLA) by using antibodies against hnRNPC and TNNT2 in healthy (N = 3; n ≥ 12) and HF (N = 5; n ≥ 13) human heart tissue. Red dots identify areas where the proteins are found to be within 40 nm of each other. The nuclei are counterstained with DAPI (blue). * $P < 0.05$; Mann-Whitney test. Scale bar = 50 μm. (**E**) Western blot analysis of three sarcomeric proteins (FHL2, PDLIM5 and MYH7) in hnRNPC-immunoprecipitated samples (IP) or total lysate (input) of healthy and failing human heart (HF). Data are shown as means ± SD See also **fig. S3** and **data file S3**.

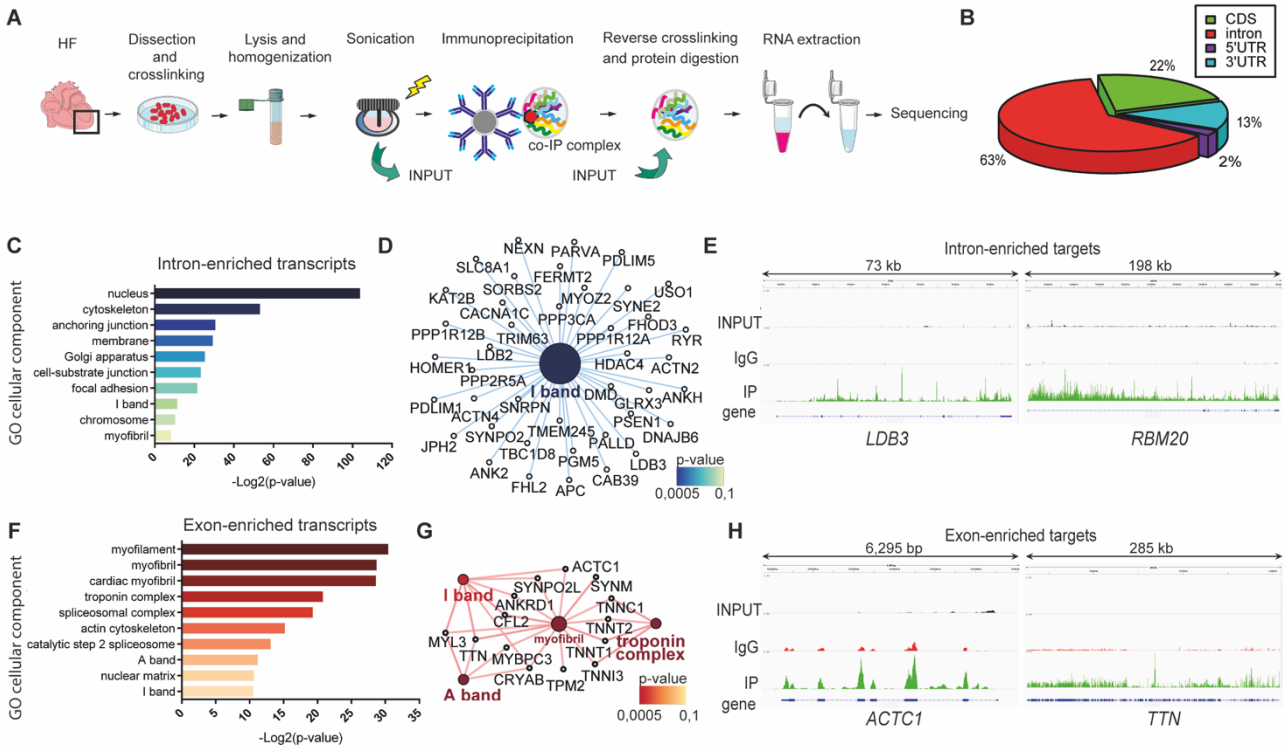

Fig. 4. hnRNPC binds transcripts encoding components of cardiomyocyte contractile apparatus in HF. (**A**) Graphical representation of the strategy adopted to identify hnRNPC RNA targets in human heart failure (N = 3) (HF) in vivo by endogenous RNA immunoprecipitation followed by sequencing. (**B**) Genomic distribution of the read counts showing the percentage of reads mapping on specific genomic regions (intron/exon, 5'UTR, 3'UTR, CDS) in immunoprecipitated samples (N = 3). (**C**) Cellular components GO categories significantly enriched in intron-enriched transcripts (log2 intron/exon ratio > 1) bound to hnRNPC in HF. (**D**) GO network of I band cellular components and the intron-enriched transcripts within this network that bind hnRNPC (*P* corrected with Bonferroni = 0.00037). The size of the node is proportional to the number of hnRNPC targets belonging to the ontology. (**E**) Individual gene representation of intron-enriched hnRNPC targets: read coverage is displayed in INPUT (black), IgG (red) and IP (green) samples. (**F**) Cellular components GO categories significantly (*P* < 0,05) enriched in exon-enriched transcripts (log2 intron/exon ratio < -1) bound to hnRNPC in HF. (**G**) GO network of cellular components of interest enriched (Group *P* corrected with Bonferroni = 9.43E-07) in exon-enriched RNAs that bind hnRNPC in HF. The size of the node is proportional to the number of hnRNPC targets belonging to the ontology. (**H**) Individual gene representation of exon-enriched hnRNPC targets: read coverage is displayed in INPUT (black), IgG (red) and IP (green) samples. See also **fig. S4** and **data file S4**.

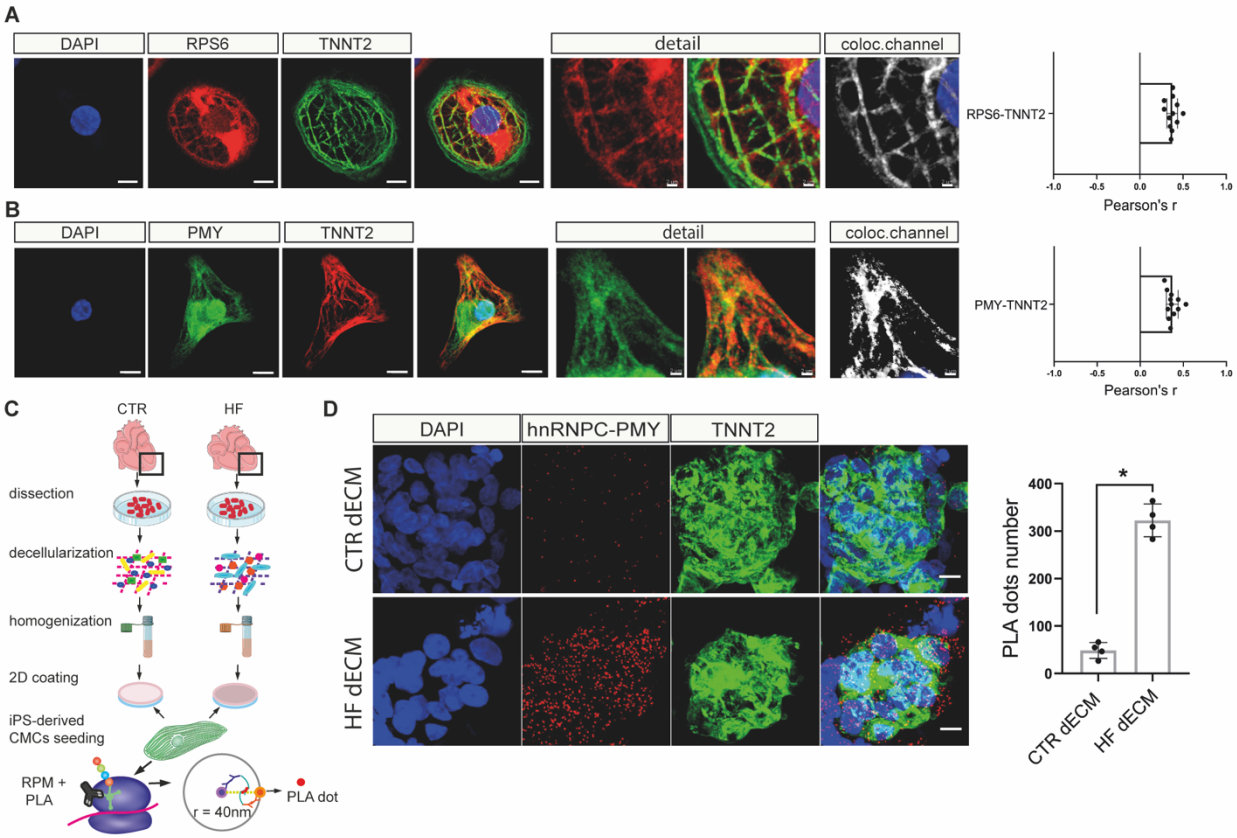

Fig. 5. hnRNPC associates to the translation machinery at the sarcomere following ECM pathological remodeling. (**A**) Representative confocal image of ribosomal protein S6 (RPS6, red) localization in iPSC-derived contractile cardiomyocytes (N = 3). Sarcomeric units are identified by cardiac troponin T (TNNT2, green) staining and nuclei are counterstained with DAPI (blue). The detail shows a magnified area of a single cardiomyocyte in which the colocalization of red and green channels has been quantified using Imaris software (n = 12). Scale bar = 10 µm; Scale bar of detail = 2 µm. (**B**) Representative confocal microscopy images of single iPSC-derived cardiomyocytes labeled with anti-puromycin antibody (PMY, green) after puromycin incorporation (N = 3). Sarcomeric units are identified by cardiac troponin T (TNNT2, red) staining and the nuclei are counterstained with DAPI (blue). Colocalization analysis of the green and red channels was quantified by Imaris software (n = 12). The detail shows a magnified area of a single cardiomyocyte. Scale bar = 10 µm; Scale bar of detail: 2 µm. (**C**) Schematic depiction of the ribopuromycilation and Proximity Ligation Assay (PLA) used to investigate the occurrence of localized translation at the sarcomeres in iPSC-derived cardiomyocytes grown onto decellularized matrices obtained from either healthy or failing human hearts. (**D**) Representative confocal microscopy images of PLA using antibodies against PMY and hnRNPC in iPSC-derived beating cardiomyocytes grown onto HF or healthy decellularized heart matrices. The cardiomyocytes were labeled with cardiac troponin T (TNNT2, green). Red dots indicate that the proteins are within 40 nm of each other. The nuclei are counterstained with DAPI (blue). (N = 4; n = 6). * $P < 0.05$; Mann-Whitney test. Scale bar = 10 µm. Data are shown as means ± SD. See also **fig. S5**.

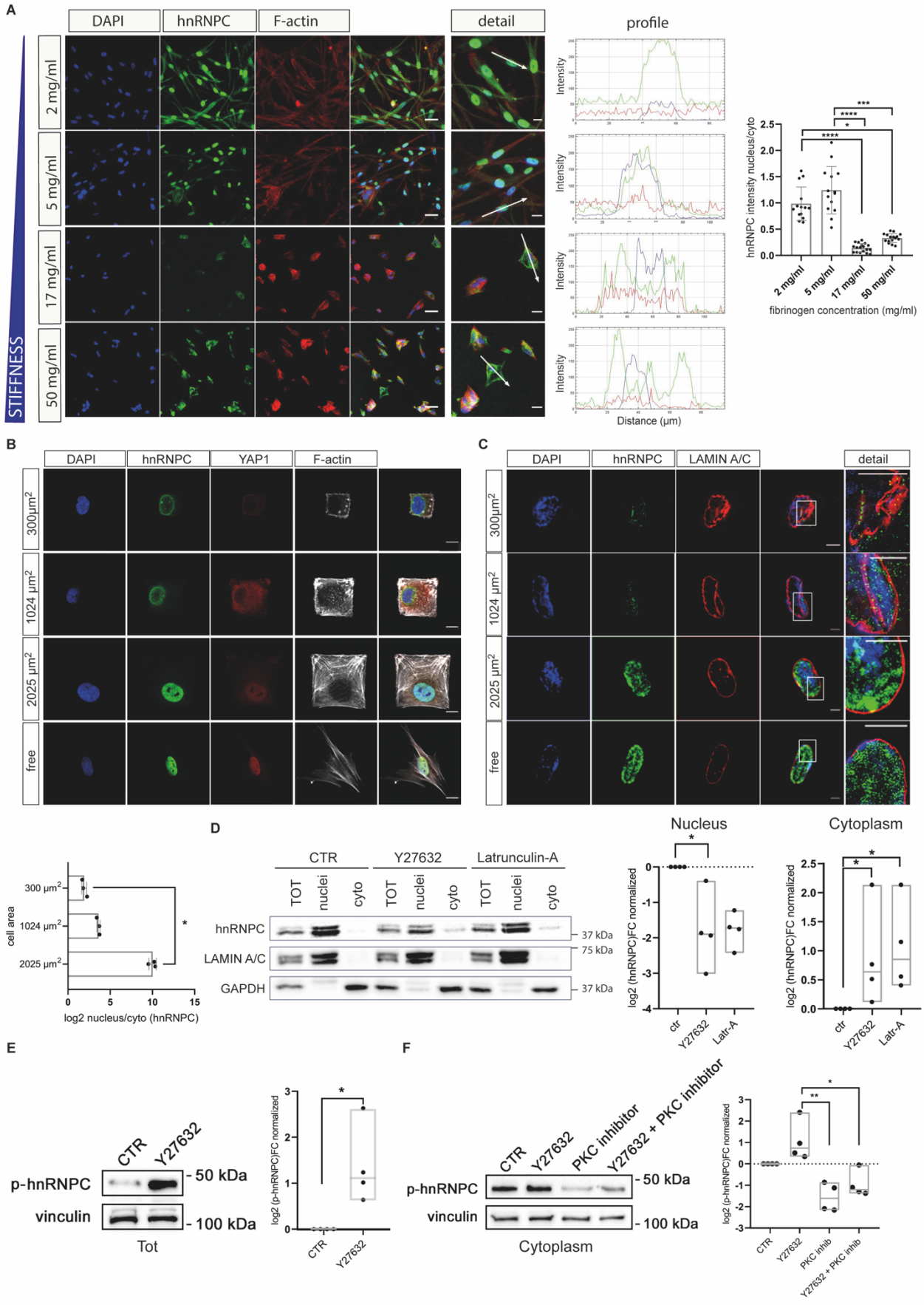

Fig. 6. hnRNPC intracellular localization is mechanically controlled via PKC phosphorylation. (**A**) Left:

Representative confocal microscopy images showing hnRNPC (green) expression in normal human dermal fibroblasts (NHDFs) embedded for 48 h in fibrin-based hydrogels with an increasing fibrinogen concentration and stiffness. Cellular F-actin was labeled with Phalloidin (red) and the nuclei were counterstained with DAPI (blue). Image analysis shows the quantification of signal distribution in NHDFs embedded for 48 h in fibrin-based hydrogels with controlled stiffness. Right: Quantification of the hnRNPC in the nucleus/cytoplasm distribution in fibrin-gels with increasing fibrinogen concentration and stiffness. For each experimental condition, data are presented as mean ± S.D. from N ≥ 7 independent fields of acquisition; * $P < 0.05$; *** $P < 0.001$; **** $P < 0.0001$, Kruskal-Wallis test followed by Dunn's multiple comparison test. (**B**) Top: confocal analysis of individual cells grown onto 300, 1024, 2025 μm^2 micropatterns coated with fibronectin. The cells were labeled with anti-hnRNPC (green), Alexa Fluor 647 Phalloidin, anti-YAP1 (red) and the nuclei were counterstained with DAPI (blue). Bottom: Barplot representation of hnRNPC nucleus/cytoplasm distribution in single cells seeded onto 300, 1024, 2025 μm^2 micropatterns (N = 3; n ≥ 8); * $P < 0.05$; Kruskal-Wallis test followed by Dunn's multiple comparison test. (**C**) Representative super-resolution images of individual cells grown onto 300, 1024, 2025 μm^2 micropatterns coated with fibronectin. The cells were labeled with anti-hnRNPC (green) and anti-Lamin A/C (red). Nuclei were counterstained with DAPI. (**D**) Western blot analysis (left) and quantification (right) of hnRNPC expression in cellular (TOT), nuclear and cytoplasmic fractions of NHDFs treated or not (CTR) with Latrunculin-A (Latr-A) and Y27632 inhibitors. GAPDH was used for loading normalization of the cytoplasmic fractions. Lamin A/C was used to normalize protein loading in the nuclear fraction. Band intensities corresponding to hnRNPC in the nuclear and cytoplasmic fractions were quantified using Bio-Rad Image Lab software. (N = 4). * $P < 0.05$, Kruskal-Wallis test followed by Dunn's multiple comparison test. (**E**) Western blot analysis (left) and quantification (right) of hnRNPC expression in NHDFs treated or not (CTR) with Y27632 inhibitor. (N = 4). Vinculin was used for loading normalization. * $P < 0.05$, Mann-Whitney test. **F)** Western blot analysis (left) and quantification (right) of hnRNPC expression in the cytoplasmic fraction of NHDFs treated or not (CTR) with Y27632 inhibitor, PKC inhibitor and the combination of the two inhibitors. (N = 4). Vinculin was used for loading normalization. * $P < 0.05$, ** $P < 0.01$ Kruskal-Wallis test followed by Dunn's multiple comparison test. Data in A and B are shown as means ± SD. Data in D, E and F are presented as dotplot with median where the box is used to highlight the value distribution. See also **fig. S6**.

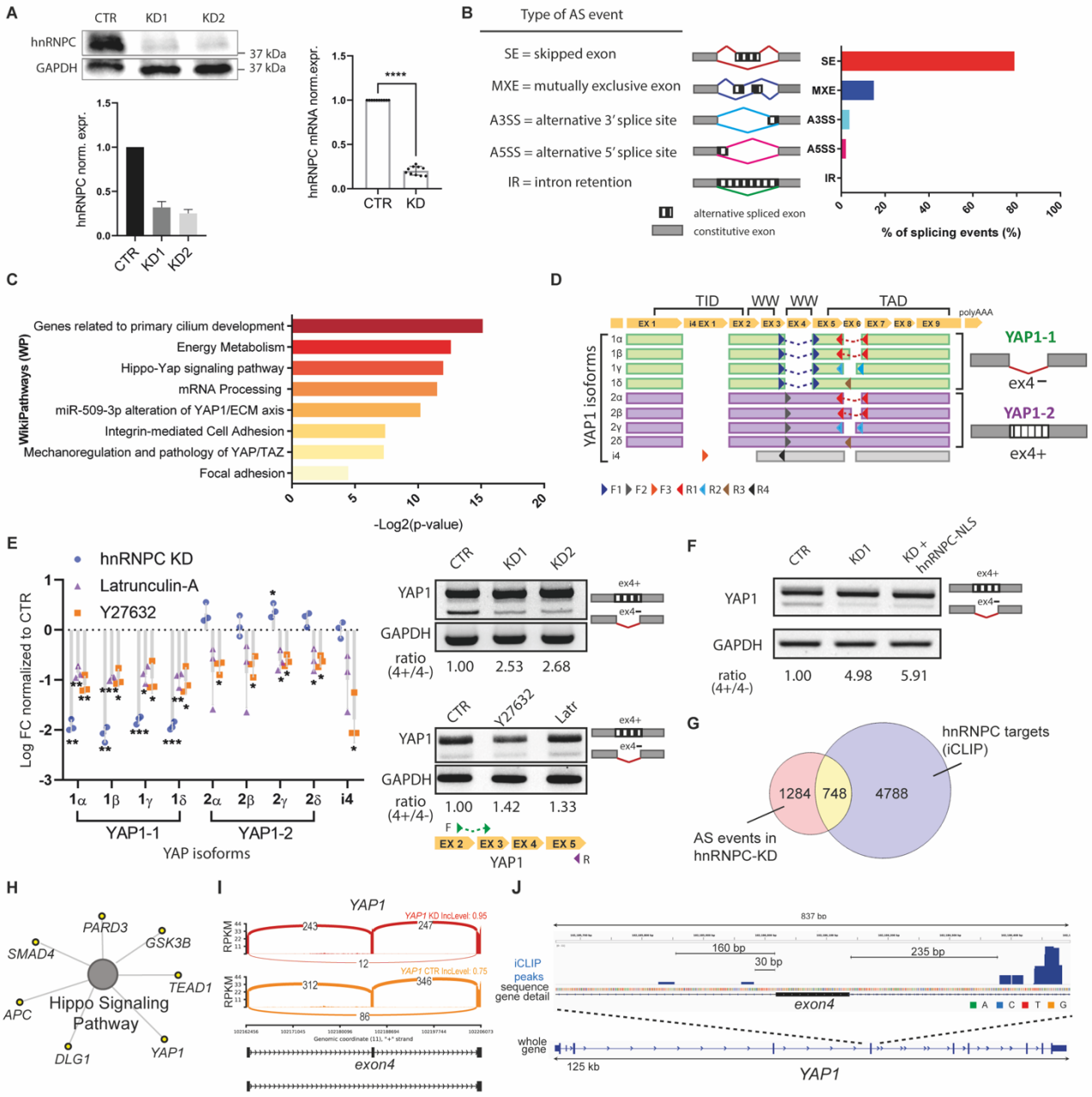

Fig. 7. hnRNPC regulates the AS of genes involved in mechanotransduction. (**A**) Left: Western blot analysis (top) and relative quantification (bottom) of hnRNPC protein expression in normal human dermal fibroblasts (NHDFs) transfected with hnRNPC siRNA constructs (KD1 and KD2) or with a control siRNA construct (CTR). Protein expression was assessed 96 h after the transfection. GAPDH was used for total protein loading normalization. (N = 3) Right: histogram representation of the results obtained by RT-qPCR analysis of hnRNPC RNA expression in NHDFs 96 h after transfection with hnRNPC (KD) or control siRNAs (CTR). (N = 10) ****p < 0.0001, Mann-Whitney test**.** (**B**) The percentage of splicing events occurring in hnRNPC KD cells classified into the five major categories of AS, as obtained by Multivariate analysis of transcript splicing (MATs). (**C**) GO analysis showing the main pathways found significantly enriched (p-value < 0.05) in genes displaying altered splicing in hnRNPC KD cells using the WikiPathways database. (**D**) Schematic representation of protein-coding YAP1 isoforms. Left) Coding regions (CDS) of four YAP1-1, four YAP1-2, and YAP-i4 isoforms are aligned and corresponding protein domains (TEAD-binding domain (TBD), WW domains, TRANS-activating-domain (TID) with N-terminal coiled-coil domain and N terminal PDZ motif) are shown. The arrows represent the approximate binding sites of forward (F) and reverse (R) primers used to detect the specific isoforms. Right) schematic representation of the AS event (exon 4 skipping) that distinguishes YAP1-1 from YAP1-2 isoforms. (**E**) Left) Dotplot representation of YAP isoforms mRNA expression (Log2FC) in NHDFs upon hnRNPC depletion (blue) or upon 24h treatment with latrunculin-A (purple) or rock inhibitor (Y27632) (orange). Each result is compared to its relative control.

(N = 3). * $P < 0.05$; ** $P < 0.01$; *** $P < 0.001$; One-sample t-test. Right) RT-PCR of YAP1 in NHDFs upon hnRNPC depletion (Top) or upon 24h treatment with inhibitors of tension (Latrunculin (Latr) and Y27632) (Bottom). Top band: exon 4-included YAP1 mRNA. Bottom band: exon 4-excluded YAP1 mRNA. (**F**) RT-PCR of YAP1 in NHDFs upon hnRNPC depletion (KD) and KD combined with the overexpression of hnRNPC-NLS mutant. (**G**) Venn diagram representation of the common transcripts identified as hnRNPC targets by hnRNPC iCLIP-seq data that were also found differentially spliced (AS events) in hnRNPC KD in NHDF cells. (**H**) GO network representation of the RNA targets of hnRNPC displaying altered splicing upon hnRNPC silencing and belonging to Hippo signaling Pathway (HSA04390). (**I**) Sashimi plot depicting YAP1 skipped exon (SE) AS event (exon 4) in hnRNPC KD NHDFs (red) and controls (orange). The exon inclusion level (IncLevel) is indicated. (**J**) Genome browser view of YAP1 gene displaying the iCLIP data (crosslink events per nucleotide) of hnRNP C (blue) (average of N = 3) in proximity of exon 4. Data are shown as means ± SD. See also **data file S5.**

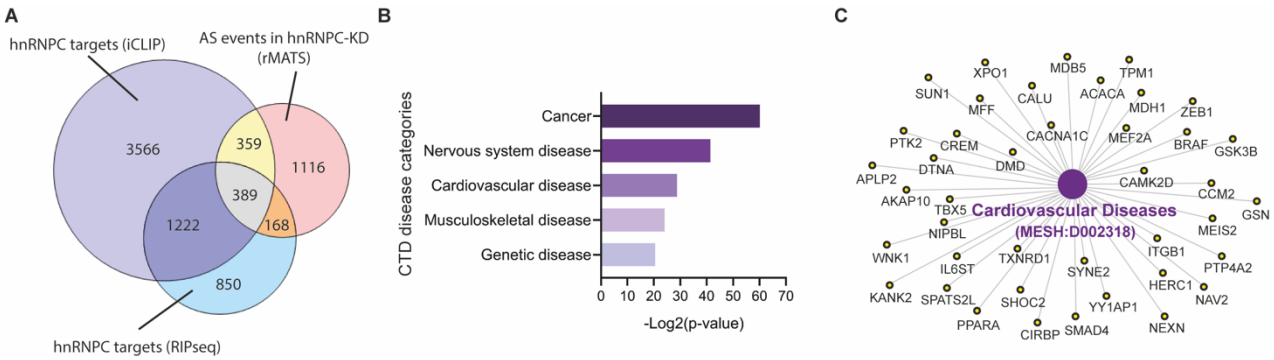

Fig. 8. hnRNPC regulates AS of genes involved in cardiovascular diseases. (**A**) Venn diagram representation of the transcripts common to the following datasets: iCLIP-seq in NHDFs, RNAseq AS-analysis in hnRNPC KD NHDF and hnRNPC RNA-IP in failing human hearts. (**B**) GO analysis of the 389 transcripts common to the three datasets as obtained by Comparative Toxicogenomics Database (CTD). (**C**) GO network representation of the transcripts belonging to Cardiovascular Disease (MESH: D002318) category and common to the three datasets analyzed: iCLIP-seq, AS (rMATS) in *HNRNPC* KD NHDF and hnRNPC RNA-IP in failing human hearts. See also **data files S6 to S8**.

The mechanical regulation of RNA binding protein hnRNPC in the failing heart

Fabiana Martino[1,2,3,4], Nandan Mysore Varadarajan[5], Ana Rubina Perestrelo[1], Vaclav Hejret[5,6], Helena Durikova[1], Dragana Vukic[5], Vladimir Horvath[1,7], Francesca Cavalieri[8,9], Frank Caruso[8], Waleed S. Albihlal[10], André P. Gerber[11], Mary A. O'Connell[5], Stepanka Vanacova[5], Stefania Pagliari[#1,3], Giancarlo Forte[#1,3].

Supplementary Information

Supplementary Materials and Methods:

1. Surgical induction of mouse myocardial infarction (MI)

MI was induced by ligating the left anterior descending coronary artery in C57BL/6 adult mice (9-10 weeks), as previously described *(36)*. Mice hearts were collected 4 days and 21 days after surgery, time points corresponding to acute MI and chronic MI, respectively. The infarcted area downstream of the ligation and the equivalent region in sham-operated control, were isolated. After collection, the isolated heart tissues were washed in PBS and processed for histology.

Experiments involving mice were approved by the Instituto de Biologia Molecular e Celular – Instituto de Engenharia Biomédica (IBMC-INEB) Animal Ethics Committee and the National Direção Geral de Veterinária (permit no: 022793), and conformed with Directive 2010/63/EU of the European Parliament.

2. Protein immunoprecipitation from human heart tissue

For immunoprecipitation of hnRNPC-binding proteins, 100 mg tissue from the human heart apex was used for each IP and control sample.

2.1 Tissue's lysate preparation: Samples were thawed on ice, then washed in PBS before tissue dissection into small pieces on a glass plate placed on ice. The tissue was mechanically homogenized in 1 ml lysis buffer [150 mM NaCl, 50 mM TRIS pH 7.5, 0.5 % deoxycholate, 0.5% Tergitol (Sigma Aldrich, NP40S), protease and phosphatase inhibitor cocktail (10%, Sigma PPC1010)] using 3.0 mm Zirkonia beads (SKU:D1032-30) and a Beadbug homogenizer (Benchmark scientific, catalog number: D1030-E) for 2 min at 300 rpm. The sample was incubated on ice for 10 min after each homogenization cycle. The procedure was repeated until the sample was completely homogeneous

(~60 min, ~6 cycles). Then, the lysate was centrifuged at 10,000 g for 10 min at 4 °C and the total lysate served as the input for western blot analysis.

2.2 Beads preparation

The storage buffer was removed from 50 µl Dynabeads Protein G (**table S2**). Then, primary antibody (hnRNPC 4F4, FHL2, PDLIM5 antibody or isotype control IgG; 5 µg per sample) dilution in 200 µl Ab binding buffer (catalog number 10007D) was added and incubated with the Dynabeads for 45 min at 4°C with gentle rotation. The Ab-conjugated-beads were washed with 200 µl Ab Binding Buffer before proceeding with immunoprecipitation step.

2.3 Immunoprecipitation

An equal amount of protein lysate for each sample was incubated with antibody-conjugated-beads, overnight under rotation at 4°C. Then, the immunoprecipitated samples were washed three times in wash buffer (150 mM NaCl, 50 mM TRIS pH 7.5) and aliquots of the samples were collected for western blotting. For elution with 8 M urea, the samples were incubated with 100 µl urea on a shaker for 20 min at room temperature (RT); the elution was repeated three times and cumulatively collected.

3. Mass spectrometry analysis

Mass spectrometry was applied to hnRNPC immunoprecipitates from human healthy control and failing (HF) heart samples to determine the composition of hnRNPC interactome. The samples were digested with trypsin using the filter-aided sample preparation (FASP) method *(75)*. Briefly, samples were reduced with 100 mM dithiothreitol at 60°C for 30 min, transferred to 30 kDa MWCO Pall Nanosep centrifugation filters (Sigma-Aldrich), washed repeatedly with 8 M urea and once with digestion buffer [1% sodium deoxycholate (SDC) in 50 mM triethylammonium bicarbonate (TEAB)] prior to alkylation with 10 mM methyl methanethiosulfonate in digestion buffer for 30 min. Digestion was performed in digestion buffer supplemented with 0.5 µg Pierce MS grade trypsin (Thermo Fisher Scientific) at 37°C and incubated overnight. An additional portion of trypsin was added and incubated for a further 2 hours and peptides were collected by centrifugation.

3.1 TMT-labeling, MS-analysis and database search

Digested peptides were labeled using TMT pro16-plex isobaric mass tagging reagents (Thermo Scientific), according to the manufacturer instructions. The samples were combined into two TMT

sets and sodium deoxycholate was removed by acidification with 10% TFA. The set included the following samples:

1) diseased 1 - IP hnRNPC

2) diseased 1 - IgG

3) diseased 2 - IP hnRNPC

4) diseased 2 - IgG

5) healthy 1 - IP hnRNPC

6) healthy 1 - IgG

7) healthy 2 - IP hnRNPC

8) healthy 2 – IgG

9) diseased 1 – IP FHL2

10) diseased 1 – IP PDLIM5

11) diseased 1 – IgG

12) diseased 2 – IP FHL2

13) diseased 2 – IP PDLIM5

14) diseased 2 - IgG

The sets were pre-fractionated into 20 fractions by basic reversed-phase chromatography (bRP-LC) using a Dionex Ultimate 3000 UPLC system (Thermo Fischer Scientific). Peptide separations were performed using a reversed-phase XBridge BEH C18 column (3.5 µm, 3.0x150 mm, Waters Corporation) and a linear gradient from 3% to 40% of solvent B over 18 min followed by an increase to 100% of solvent B over 5 min. Solvent A consisted of 10 mM ammonium formate buffer at pH 10.00 and solvent B was 90% acetonitrile and 10% 10 mM ammonium formate at pH 10.00. The fractions were concatenated into 10 sequential fractions (1+11, 2+12, up to 10+20), dried and reconstituted in a solution of 3% acetonitrile, 0.2% formic acid.

3.2 nLC-MS/MS

The fractions were analyzed on an orbitrap Fusion™ Lumos™ Tribrid™ mass spectrometer interfaced with an Easy-nLC1200 liquid chromatography system (Thermo Fisher Scientific). Peptides were trapped on an Acclaim Pepmap 100 C18 trap column (100 µm x 2 cm, particle size 5 µm, Thermo Fischer Scientific) and separated on an in-house packed analytical column (75 µm x 30 cm, particle size 3 µm, Reprosil-Pur C18, Dr. Maisch) using a linear gradient: 5% to 33% solvent B for 77 min, followed by an increase to 100% solvent B for 3 min, and 100% solvent B for 10 min at a flow of 300

nL/min. Solvent A was 0.2% formic acid and solvent B was 80% acetonitrile, 0.2% formic acid. Precursor ion mass spectra were acquired at 120,000 resolution and MS/MS analysis was performed in a data-dependent multi-notch mode where the CID spectra of the most intense precursor ions were recorded in an ion trap at a collision energy setting of 35 for 3 sec ('top speed' setting). Precursors were isolated in the quadrupole with a 0.7 m/z isolation window, charge states 2 to 7 were selected for fragmentation, and dynamic exclusion was set to 45 s and 10 ppm. MS3 spectra for reporter ion quantitation were recorded at 50,000 resolution with HCD fragmentation at a collision energy of 55 using the synchronous precursor selection.

3.3 Proteomic Data Analysis

The data files for each set were merged for identification and relative quantification using Proteome Discoverer version 2.2. The search was made against the *Human* Swissprot Database version June 2019 (Swiss Institute of Bioinformatics, Switzerland) using Mascot version 2.5.1 (Matrix Science) as a search engine with precursor mass tolerance of 5 ppm and fragment mass tolerance of 0.6 Da. Tryptic peptides were accepted with zero missed cleavage, variable modifications of methionine oxidation and fixed cysteine alkylation, and TMT-label modifications of the N-terminal and lysine were selected. The reference samples were used as a denominator and to calculate the ratios. A percolator was used to validate the identified proteins. TMT reporter ions were identified in the MS3 HCD spectra with 3 mmu mass tolerance. The quantified proteins were filtered at 1% FDR and grouped by sharing the same sequences to minimize redundancy. Only peptides unique for a given protein were considered for protein quantification, excluding those common to other isoforms or proteins of the same family.

Proteomics analysis was performed on hnRNPC-immunoprecipitated samples and IgG-immunoprecipitated samples (negative controls) from two healthy controls and two failing (HF) human heart tissues. The ratio of IP/IgG abundances was calculated for each protein found in each sample. A protein was considered successfully immunoprecipitated when IP/IgG > 1.5 in both biological replicates (healthy1-healthy2 or HF1-HF2). Proteomics analysis on FHL- and PDLIM5-immunoprecipitated samples and IgG- immunoprecipitated samples from two HF samples was performed using the same method.

Proteomaps **(Fig. 2C)** (https://bionic-vis.biologie.uni-greifswald.de/) *(35, 76)* were used to represent the quantitative composition of the hnRNPC interactome in healthy and failing human hearts, with a focus on protein function. The polygonal areas in the proteomaps represent the protein

abundances in the immunoprecipitated sample as detected by TMT-MS analysis. Functionally related proteins are distributed in similarly colored regions. Proteomaps are based on the KEGG Pathways gene classification.

4. Decellularization of human myocardial tissue and cell seeding on decellularized ECM

The decellularization protocol was performed as previously described *(30, 74)* with slight modifications. First, the frozen healthy and diseased heart samples were thawed and sliced into small pieces using a 2x2 mm grid as a reference. The explants were then immersed in mild decellularization solutions and mixed by shaking at 300 rpm (Eppendorf Thermomixer C 80 with orbit diameter of 3 mm) at 25°C. The specimens were first immersed for 18 h in hypotonic buffer (10 mM Trizma Base Sigma / 0.1% EDTA 82 Applichem, pH 7.8), then for 24 h in detergent solution (0.5% Sodium Dodecyl Sulfate 83 (SDS, Sigma) / 10 mM Trizma Base Sigma, pH 7.8) and for 1 h in hypotonic wash buffer (10 mM TrizmaBase Sigma, pH 7.8). DNAse treatment [50 U/mL 85 DNAse I (StemCell Technologies) in 10 mM Tris HCl, pH 7.8] was performed for 3 h at 37°C. Finally, the samples were washed overnight in PBS (12 rpm, GFL Shaker 3014).

The decellularized samples were mechanically homogenized in 400 µl sterile PBS supplemented with 1% penicillin/streptomycin using 3.0 mm Zirkonia beads (SKU:D1032-30) and a Beadbug homogenizer (**table S2**). dECM matrices were homogenized until full dissociation with cycles of 1 min at 3,000 rpm and 2 min on ice. A Pierce BCA Protein Assay Kit (ThermoFisher) was used to quantify the proteins in the homogenized samples. Decellularized matrices were preserved in PBS supplemented with 1% Penicillin/Streptomycin (Diagnovum) at 4°C.

The coating was performed by incubating 12 mm coverslips with 100 µl/cm^2 dECM solution (5µg/ml) at 37°C overnight in PBS-1%Penincilin/Streptomycin solution. Coating solution was removed immediately before cell seeding. Beating iPSC-CMs (day 15-20) were dissociated in TryPLE, re-suspended in RPMI medium supplemented with B27 supplement minus insulin and Y27632, and seeded onto ECM-coated-coverslips. Then, 24 h after seeding and when the cells re-started beating, the medium was replaced with RPMI supplemented with B27 supplement plus insulin. 48 h after seeding, the ribopuromycilation assay was performed as described in **Supplementary Method 5**. Cells were then fixed and kept at 4 °C until PLA was performed. Strategy depicted in **Fig. 5C**.

5. Ribopuromycilation

Ribopuromycilation assay was performed to visualize the active sites of translation following Procedure A in the Original RPM protocol, as previously described *(77, 78)*. A schematic representation of the protocol can be found in **fig. S5D**. All the buffers were freshly prepared before use.

Beating cardiomyocytes between day 20 and day 30 of differentiation were incubated with cycloheximide (CHX), a chain elongation inhibitor, at the final concentration of 355 µM for 5 min at RT. Labeling medium containing CHX (355 µM) and puromycin (PMY) (91 µM final concentration) was added for 5 min at 37 C. PMY is incorporated into nascent peptides while CHX prevents PMY-nascent chain release from the ribosomes. For each experiment, a control without puromycin addition was performed. After labeling, the cells were washed with cold PBS. All subsequent steps were performed on ice. Extraction buffer (Triton 0,01%, MgCl2 5mM, KCl 25nM, CHX 355 µM, protease and phosphatase inhibitors 1% v/v, Tris-HCl 50mM pH 7.5) was slowly added and incubated for 2 min. Then, the cells were washed with wash buffer (MgCl2 5mM, KCl 25nM, CHX 355 µM, protease and phosphatase inhibitors 1% v/v, Tris-HCl 50mM pH 7.5) and fixed with 4% PFA for 15 min at RT. After fixation, the cells were washed three times with PBS and immunostaining was performed.

6. Cell culture and iPSC cardiac differentiation

Normal human dermal fibroblasts (NHDF, ATCC) were grown in DMEM Low glucose with stable glutamine and with sodium pyruvate supplemented with 10% fetal bovine serum (FBS) and 1% penicillin-streptomycin (P/S). HeLa cell lines were grown in in DMEM High glucose with stable glutamine and with sodium pyruvate supplemented with 10% FBS, 1% non-essential amino acids (NAA) and 1% P/S.

The human induced pluripotent stem cell (iPSC) line DF 19-9-7T was purchased from WiCell (Madison, WI, USA). iPSCs were cultured on Matrigel Matrix-coated (1:100 in DMEM/F12, Corning) Growth Factor Reduced plates in complete Essential 8™ Medium (Life Technologies) containing penicillin/streptomycin (0.5 %, VWR). For passaging, the cells were dissociated using TrypLE Express (Life Technologies) and supplemented with Rock Inhibitor Y27632 (2.5µM, Selleckchem) for 24h.

Cardiac differentiation was performed as previously described *(46)*, with slight modifications. The medium was changed daily until the cells formed a monolayer. At day 0 of cardiac differentiation,

100% confluent cells were incubated with mesoderm induction medium: RPMI 1640 (Sigma-Aldrich) supplemented with penicillin/streptomycin, L-glutamine (2 mmol/L, Biowest), B-27™ supplement minus insulin (1X, Thermo FisherScientific) and CHIR99021 (8 µM, Sigma-Aldrich). At day 2, the medium was replaced with RPMI plus B-27 supplement minus insulin and IWP-2 (5 µmol/L, Selleck chemicals). At day 4, the medium was changed to RPMI plus B27 supplement minus insulin and substituted every other day until the cells started beating. Around day 8-10, after the iPSC-derived cardiomyocytes (CMs) started beating, the medium was substituted with RPMI supplemented with B27 supplement plus insulin (1X, Thermo Fisher Scientific) and replaced every 2-3 days over the differentiation time to assure cell beating.

7. Cell treatments, embedding in fibrin hydrogels and micropatterning

7.1 Cell treatments

For the treatment with inhibitors of cytoskeletal tension, cells were incubated with Latrunculin-A (1 µM) for 30 min or with Rock inhibitor (Y27632) (50 µM) for 4 h, at 37°C and 5% CO_2. When requested, the cells were treated with PKC Inhibitor (Chelerythrine Chloride, Merck) (5 µM), or the combination of the two inhibitors, for 4h, at 37°C and 5% CO_2. After treatments, cells were washed twice with PBS, harvested with TryPLE and the proteins were extracted as described in **Supplementary Method 10.**

7.2 3D Fibrin hydrogel preparation, 2D elastic surfaces and cells seeding

3D fibrin gels were produced as previously described *(51)*. Fibrinogen and thrombin were purchased from Baxter. DMEM (50µL) containing $2x10^5$ normal human dermal fibroblasts (NHDFs) was embedded in 50µL of 40 U/mL thrombin-$CaCl_2$ solution. The resultant solution was then quickly mixed 1:1 with fibrinogen 100 mg/mL, 34 mg/mL, 10 mg/mL or 4 mg/mL to generate clots with fibrinogen concentrations of 50 mg/mL, 17 mg/mL, 5 mg/mL and 2 mg/mL, respectively, with a constant thrombin concentration of 20 U/ml. The 3D fibrin gels with embedded cells were polymerized for 1 h at 37°C before the addition of complete growth medium (DMEM) supplemented with aprotinin (3000 KIU/mL). The 3D fibrin hydrogels were kept at 37 °C and 5% CO_2 in a humidified incubator until processed.

Thirty-five mm high elastically supported surface (ESS) µ-Dishes with a stiffness of 28 or 1.5 kPa were purchased from iBIDI (Munich, Germany). iPSC-derived cardiomyocytes were seeded on Matrigel-coated µ-Dish ESS in RPMI medium supplemented with B27 supplement minus insulin and Y27632.

After 24 hours, the medium was changed to B27 supplement plus insulin and 48 hours after seeding the cells were fixed with 4% PFA for 15 min at RT. After fixation, the cells were washed three times with PBS and immunostaining was performed.

7.3 Micropatterning

Fibronectin-coated micropatterned slides featuring different areas or patterns (ref: 10–950–10–18; **table S2**) were purchased from CYTOO (CYTOO, Grenoble, France). After 24 h culture in complete medium on the microarrays, the NHDFs were fixed in 4% PFA for 15 min at RT and analyzed by immunofluorescence; n≥8 squares of each type were analyzed *per* experiment (N=3).

8. Cell transfection and plasmid mutagenesis

8.1 Cell transfection

HNRNPC knockdown was performed as previously described *(23)*. In brief, NHDF cells and iPSC-derived cardiomyocytes (CMs) were transfected using two different human hnRNPC1/C2 stealth select small interfering RNA (siRNA) (Invitrogen, HSS179304 and HSS179305) and a stealth siRNA negative control low GC (Invitrogen) at a final concentration of 10 nM. The transfection was performed using Lipofectamine RNAiMAX (Invitrogen) transfection reagent according to the protocol "RNAiMAX Reverse Transfections Lipofectamine" provided by ThermoFisher Scientific (**table S2)**.

For each well of a 6-well plate to be transfected, siRNA duplex-Lipofectamine™ RNAiMAX complexes were prepared as follows: the growth media was replaced by 30 pmol siRNA diluted in 500 µl Opti-MEM Medium (Gibco™, ThermoFisher Scientific) without serum and was gently mixed. Lipofectamine™ RNAiMAX was gently mixed before use, and 5 µl was added to each well containing the diluted siRNA molecules. The resultant solution was gently mixed and incubated for 20 min at RT. NHDFs and iPSC-CMs were diluted in Opti-MEM Medium at a concentration of $1x10^5$ cells/ml; then, 2.5 ml of the diluted cells were uniformly added to each well containing siRNA-Lipofectamine™ RNAiMAX complexes. Cells and transfection reagents were incubated at 37°C in a CO_2 incubator for 24 h followed by the addition of 2 ml of complete growth medium (DMEM containing 10% FBS, 2mM L-glutamine and 1% penicillin/streptomycin for NHDFs; essential 8™ Medium containing penicillin/streptomycin 0.5% and supplemented with ROCK inhibitor Y27632 1:4000. The knockdown efficiency was assessed 96 h after transfection (**see Fig.7A and fig. S7A**).

8.2 Plasmid site-directed mutagenesis

Plasmid containing wild type (WT) sequence of hnRNPC1/C2 was purchased from Addgene (pT7-V5-SBP-C1-HshnRNPC1) and used as a backbone for site-directed mutagenesis. To obtain NLS-deficient mutant of hnRNPC1/2, arginines were mutated to alanine at two positions (R158A and R160A). To this purpose, double primer PCR method was performed using Phusion Hot Start II polymerase (Thermo Fisher), WT hnRNPC1/2 as a template and the following primer sequences: *Forward: 5' TCGAAAGCTCAGGCTGTATCAGGAAACACTTCACGAAGGGGC 3'* and *Reverse: 5' TACAGCCTGAGCTTTCGAGGGCACTACAGCCCGAGC 3'.* The obtained PCR products were incubated for 1h at 37°C with DpnI enzyme (Thermo Fisher) and further used for transformation of Top10 E.coli bacterial strain. Validation of the site-directed mutagenesis was performed by the Sanger sequencing method with CMV forward and SC40pA reverse sequencing primers.

8.3 siRNA and hnRNPC-NLS plasmid co-transfection

For knock-down experiments, NHDF and HeLa cells were transfected with the small interfering RNA targeting hnRNPC1/2 at the 3'UTR with sequence: sense- *5' GCGCUUGUCUAAGAUCAAAU 3'* and dTdT overhangs as described previously *(79)*. Scramble siRNA was used as a negative control in each experiment. Both hnRNPC1/2 siRNA and scramble were purchased from Eurofins (genseq).

In brief, cells were seeded on the day of transfection in 6-well plate. SiRNA transfection Lipofectamine™ RNAiMAX Transfection Reagent (Invitrogen) was used following manufactures instruction. These included preparation of both siRNAs at the final 20nM concentration and transfection reagent of 5 µl per well independently in the serum free Opti-MEM Medium (GibcoTM, ThermoFisher Scientific). Once prepared, they were mixed in 1:1 ratio and incubated at the room temperature for 20 minutes to allow final complex formation. After this complex was added to cells, they were left for further incubation at 37°C in a CO2 incubator. The following day media was replaced with the fresh culture media. 72h following siRNA transfection, NHDF and HeLa cells were transfected with 1µg of plasmid pT7-V5-SBP-C1-HshnRNPC1 in 6-well plate. Briefly, 4µl of Lipofectamine™ 3000 reagent (Invitrogen) was gently resuspended in the OPTIMEM media. Plasmid DNA was prepared by mixing 1 µg of plasmid DNA with 2 µl of p3000 reagent. Diluted lipofectamine was then added to the plasmid DNA mix and incubated for 15 min at room temperature to allow complex to be formed. After complex is formed, it was added to cells with fresh media. Cells were collected after 24h of the incubation at 37°C in a CO2 incubator.

9. Quantitative real-time PCR (qPCR)

Cells were harvested from culture plates by TryPLE, cell pellet was washed twice in DPBS and total RNA was isolated using a High Pure RNA Isolation Kit (Roche) according to the manufacturer's instructions. After RNA isolation, samples were treated with Dnase (Roche) to remove genomic DNA contamination and 1 µg of total RNA was transcribed into cDNA using a Transcription First Strand cDNA Synthesis Kit (Roche) and analyzed by qPCR using a SYBR Green I Master Kit (Roche) and a LightCycler 480 Real-Time PCR System (Roche). The samples were loaded in triplicate and quantified by ΔCt method normalized to reference GAPDH expression using LightCycler 480 Software release 1.5.0. Non-template controls (NTC) containing no cDNA were included in each reaction. The primer sequences used are listed in **table S2**.

10. Western blotting

For total protein extraction from human heart tissue, samples were thawed from -80°C, placed on a glass plate on ice, finely cut into small pieces and mechanically disrupted by pipetting and vortexing. The homogenized heart tissue was then incubated with RIPA lysis buffer (Merck Millipore, 20-188) supplemented with protease and phosphatase inhibitor cocktails (1% v/v, Sigma-Aldrich) for 30 min on ice, vortexing every 10 min. The lysate was then centrifuged at 4°C for 15 min at 16,000 g. The supernatant was collected in a new eppendorf tube and stored at -80°C until further use.

For total protein extraction, the cells were detached with TrypLE Express (Life Technologies, 12604-013), and the pellet was washed with PBS and incubated in RIPA buffer as described above.

Compartment protein extraction was performed using an NE-PER™ Nuclear and Cytoplasmic extraction kit (ThermoFisher, **table S2**) following the manufacturer's specifications. A Pierce BCA Protein Assay Kit (ThermoFisher) was used for protein quantification, with albumin serum bovine standards for calibration. The respective absorbances were read using a Multiskan™ GO Spectrophotometer.

Protein extracts (5-10 µg) were boiled for 5 min at 95 °C, loaded on 10% Mini-PROTEAN TGX™ Precast Protein Gels and separated at 100 V in Tris/Glycine/SDS buffer in a Mini-Protean Tetra System (Bio-Rad). The proteins were transferred to polyvinylidene difluoride membranes (PVDF, Bio-Rad) using a semi-dry Trans-Blot Turbo transfer system (Bio-Rad). The membranes were immersed in 5% skim milk (or 5% BSA for detection of phosphorylated protein) in TBST to block unspecific sites for 1 h, followed by primary antibody incubation in 5% BSA in TBST with gentle rotation overnight at 4°C. After three washes in TBST, the membranes were incubated for 1 h at RT

with the secondary HRP-conjugated antibody (Sigma-Aldrich) in 5% BSA in TBST. Clarity™ Western ECL Substrate (Bio-Rad) and a ChemiDoc MP Imaging System (Bio-Rad) were used to detect Chemiluminescence. Band intensities were quantified using Bio-Rad Image Lab software.

11. RNA immunoprecipitation from human heart tissue

For immunoprecipitation of hnRNPC RNA complexes, 100 mg tissue from the human heart apex was used for each IP and control sample. All the buffers were prepared before use. A schematic representation of the experimental strategy can be found in **Fig. 4A**.

11.1 Tissue's lysate preparation: The samples were thawed on ice, washed twice in PBS and then the tissues were cut into small pieces (2mm diameter) on a glass plate placed on ice. Cross-linking was achieved by soaking the samples in 1% (v/v) formaldehyde for 15 min in 10 ml PBS at RT with gentle rotation. The cross-linking reaction was quenched by adding 200mM TRIS. The samples were centrifuged at 50 g for 1min at 4°C, washed twice in PBS and then mechanically homogenized in 1ml Polysome Lysis Buffer (PLB) [20mM Tris buffer (pH 7.5), 100 mM KCl, 5mM EDTA at pH 8, 0.5% Tergitol (Sigma Aldrich, NP40S), 2 mM DTT, 50 U/mL RNase OUT, heparin 0.2 mg/mL, protease and phosphatase inhibitor cocktail (10%, Sigma PPC1010)] using 3.0 mm Zirkonia beads (SKU:D1032-30) and a Beadbug homogenizer for 2 min at 300 rpm. The sample was cooled on ice for 10 min after each homogenization cycle. The procedure was repeated until the sample was completely homogeneous (~60 min, ~6 cycles). Then, the samples were sonicated (focused-ultrasonicator M220, Covaris) for five cycles, consisting of: peak power 50, duty factor 20%, 200 cycles, 20 sec, plus 30 sec delay, at 4 °C. The resulting lysates were centrifuged twice for 10 mins each at 4 °C and 14,000 x g and the supernatant collected. Aliquots (1:5 of total lysate) of the supernatant were collected to serve as the input for western blot analysis and total RNA extraction.

11.2 Beads preparation: The storage buffer was removed from 100 µl Dynabeads Protein G (immunoprecipitation Kit, catalog number 10007D) using a magnetic rack. Then, the beads were equilibrated by washing them three times with 400 µl NT2-coupling buffer [50 mM Tris–HCl at pH 7.5, 500 mM NaCl, 1 mM MgCl2, with 1% Tergitol, 5% BSA, 0.02% sodium azide, 0.02 mg/mL heparin]. The primary antibody (hnRNPC 4F4 antibody, sc-32308 or isotype control IgG mouse, sc-2025, Santa Cruz Biotech, 10 µg/sample; **table S2**) was then diluted in 400 µl NT2-coupling buffer and incubated with the Dynabeads for 1 h at 4°C with gentle rotation. The antibody-conjugated-

beads were washed twice with 400µl NT2-RIP buffer [50 mM Tris–HCl pH 7.5, 500 mM NaCl, 1 mM $MgCl_2$, with 1% Tergitol, 50 U/mL RNase OUT, 2 mM DTT, 30 mM EDTA at pH 8, heparin 0.02 mg/mL].

11.3 Immunoprecipitation: The antibody-conjugated beads were incubated with an equal volume of cross-linked lysate in NT2-RIP buffer (1:10) for each sample, overnight and under gentle rotation at 4°C. The IP-beads were resuspended in ice-cold NT2 buffer [50 mM Tris–HCl at pH 7.5, 500 mM NaCl, 1 mM $MgCl_2$, and 1% Tergitol] and transferred to a new 1.5 mL conical microtube. The IP-beads were washed four times in NT2 buffer by shaking the tubes and aliquots (~150 µl) were collected for western blot analysis.

11.4 Elution and reverse cross-linking: The input samples were thawed (aliquot for total RNA extraction) and reverse cross-linking was carried out by resuspending the IP-beads samples and input sample in 250 µl SDS-EDTA elution buffer [50 mM Tris–HCl at pH 8, 100 mM NaCl, 10 mM EDTA, 1% (w/v) SDS] supplemented with 60 µg Proteinase K per sample. The samples were then incubated for 1.5 h at 55 °C with shaking (800 rpm).

11.5 RNA extraction: A total of 400 µl TRIzol (Invitrogen) was added to the samples and incubated for 5 min on ice. Then, 80 µl chloroform was added and incubated for 30 sec with shaking before centrifugation at 10,.000 g for 10min at 4°C. The upper aqueous phase was removed and transferred to a new tube before the addition of 50 µl Salt I (Millipore), 15 µl Salt II (Millipore), 4 µl Precipitate Enhancer (Millipore) and 850 µl absolute ethanol (**table S2)**. The RNA was precipitated overnight at -80°C, then centrifuged at 14,000 g for 30 min at 4 °C. The supernatant was removed, and the pellet was washed twice with ice cold 75% ethanol by centrifugation at 5 min at max speed at 4°C. Finally, the pellet was air-dried for 2 min at RT and then resuspended in 15 µl nuclease free water.

12. RNA sequencing, RIP-seq analysis and AS analysis

12.1 Sequencing

A sequencing library was prepared using an NEBNext Ultra II Directional Kit (New England Biolabs, MA, USA). For RIP-sequencing, immunoprecipitated RNA was used as an input into the total RNA library preparation protocol; control input RNA was first rRNA depleted using a QIAseq Fastselect HMR Kit (Qiagen, Germany). For the alternative splicing analysis, 200-300 ng total RNA was used as an input into the polyA enrichment module protocol. The samples were fragmented and transcribed into cDNA. Following universal adapter ligation, the samples were barcoded using dual indexing

primers. The RNA resultant from the RIP of heart tissue was sequenced to 25-35 million single-end 75bp reads while the RNA resultant from the NHDF transfection with hnRNPC siRNA and respective control constructs was sequenced to >50 million paired-end 75 bp reads/sample. The samples were sequenced on an Illumina Nextseq 550 sequencer (Illumina, CA, USA).

A quality check of raw fastq reads was carried out by FastQC *(79)*. The adapters and quality trimming of the raw fastq reads was performed using Trimmomatic v. 0.36 *(80)* with settings CROP:250 LEADING:3 TRAILING:3 SLIDINGWINDOW:4:5 MINLEN:35. The trimmed RIP-Seq and RNA-seq reads were mapped against the human genome (hg38) and Ensembl GRCh38 v.94 annotation using STAR v. 2.5.3a *(81)* as splice-aware short read aligner and default parameters, with the exception of outFilterMismatchNoverLmax 0.1 and twopassMode Basic. Quality control after alignment including assessment of uniquely and multi-mapped reads, read coverage distribution, level of read duplication, rRNA contamination, genomic regions of mapped reads and gene biotypes was performed using several tools, namely RSeQC v2.6.2 *(82)*, Picard toolkit v2.18.27 (GitHub Repository. http://broadinstitute.github.io/picard/), Qualimap v.2.2.2 *(83)* and FastQ Screen v0.13.0 *(84)*[7].

12.2 RIP-seq analysis

Counts of mapped reads to specific gene features were made using a modified Ensembl GRCh38 v.94 annotation GTF file. The annotation file was modified as follows:

12.2.1 Four individual GTF files were derived from original annotation GTF file: (1) only for regions specified as a feature "gene", (2) for regions specified as a feature "exon", (3) for regions specified as a feature "three_prime_utr" and (4) for regions specified as a feature "five_prime_utr" (only for chromosomes 1-23, X, Y and MT).

12.2.2 Two derived GTF files for genes and exons were subtracted using bedtools subtract v2.29.0 (Quinlan et al.,2018) considering the strandness of the alignment as a parameter to create the GTF file with only intronic regions; regions annotated as RNA (antisense_RNA, bidirectional_promoter_lncRNA, 3prime_overlapping_ncRNA, lincRNA) were excluded from GTF file.

12.2.3 As a next step, the 3'UTR and 5'UTR regions in the GTF files were subtracted from the exonic GTF file using bedtools subtract.

12.2.4 The subtracted exonic GTF, 5'UTR GTF, 3'UTR GTF and intronic GTF were joined together into one GTF file, which was sorted by positions, resulting in a final GTF file that was used to count the

mapped reads. Read counts for four specific genomic features (CDS - exons without UTR regions, introns, 3'UTR and 5'UTR) were gathered using featureCounts v1.5.2*(85)*. The set included the following samples:

1) diseased 1 (HF1) – input (total lysate)
2) diseased 1 (HF1) - IP hnRNPC
3) diseased 1 (HF1) - IgG
4) diseased 2 (HF2) - input
5) diseased 2 (HF2) – IP hnRNPC
6) diseased 2 (HF2) - IgG
7) diseased 3 (HF3) – input (total lysate)
8) diseased 3 (HF3) – IP hnRNPC
9) diseased 3 (HF3) - IgG

The input RNA samples were normalized on sequencing depth and further used as normalization factors for IP and IgG sample normalization. IP and IgG samples were further normalized on the length of each feature on a logarithmic scale with base 2. Exon counts were represented by the sum of CDS, 3'UTR and 5'UTR, while introns only included intronic reads. The total transcript expression was defined as the sum of the exonic and intronic reads. The immunoprecipitated transcripts were considered statistically significant when the IP/IgG ratio > 5 and the transcript total expression > 200 in at least two out of three replicates of the IP samples. To distinguish between exons-enriched targets and introns-enriched targets, we established a ratio of intronic/exonic reads on a logarithmic scale with base 2 and set the cutoff as $\log_2$(intron/exon) > 1 (intron-enriched) or $\log_2$ (intron/exon) < -1 (exon-enriched) and the total transcript expression > 200. To visualize all four genomic features (CDS - exons without UTR regions, introns, 3'UTR and 5'UTR) in pie plots, their counts were handled separately without any cutoffs or filtering. Volcano and bar plots were created using the ggplot2 v3.3.1 *(86)* library, and pie plots were generated using the plotrix v3.7-8 *(87)* library.

12.3 Alternative splicing (AS)

The experimental design included the following samples:

CTR x3 : NHDFs transfected with a stealth siRNA negative control low GC (Invitrogen)
KD1 x3: NHDFs transfected with hnRNPC1/C2 siRNA HSS179304 (Invitrogen)
KD2 x3: NHDFs transfected with hnRNPC1/C2 siRNA HSS17930 (Invitrogen).

Alternative splicing (AS) analysis was carried out by rMATS v3.1.0 *(88)*, which detects differentially used exons by comparing exon-inclusion levels based on the number of junction reads. In this case, all replicates from the KD1 and KD2 conditions were treated as one condition containing 6 replicates and were compared to three replicates of CTR condition. rMATS was then run with settings -t paired --readLength 75 --libType fr-secondstrand. Sashimi plots depicting skipped exon AS events were generated using rmats2sashimiplot v2.0.2 (https://github.com/Xinglab/rmats2sashimiplot), whereby representative replicates of KD and CTR conditions can be visualized. The clusterProfiler v3.12.0 *(89)* R library was used for Gene Ontology (GO) analysis. The input list of genes uploaded for GO analysis consisted of a pool of genes from all individual rMATS AS event outputs (Alternative 5' start site, Alternative 3'start site, Skipped exons, Retained introns and Mutually exclusive exons), filtered based on FDR ≤ 0.01 and Inclusion level difference (ΔPSI) ≥ 0.1 cutoffs.

AS analysis in human heart samples was carried out by rMATS v3.1.0. Three samples for each diseased condition (HCM, DCM, ISCH, NICM) were analysed and compared to healthy controls (GSE141910). The samples analysed belong to the following published datasets: GSE108157 and GSE141910. The differentially spliced events were calculated based on FDR ≤ 0.05 and inclusion level difference (ΔPSI) ≥ 0.1 cutoffs.

12.4 Splicing analysis (RT-PCR)

GoTaq G2 DNA Polymerase (Promega) kit was used for the splicing assay following the manufacturer's intruction. To assess YAP1 exon 4 inclusion and exclusion pattern, the primers EX2-3 Yap1 (F) and EX5 Yap1 (R) were used (annealing temperature of 49°C and total number of cycles 28). Additionally, PCR for GAPDH was performed at 55°C annealing temperature for a total number of cycles 24 and used for normalization.

PCR products were resolved at 2% agarose gel and the images were taken with GelDoc (BioRad) machine. Further analysis and quantification were performed with ImageJ software.

13. Cytoscape Analysis and GO analysis

The EnrichR enrichment analysis tool was used (http://amp.pharm.mssm.edu/Enrichr) *(90, 91)*, for the molecular function GO analysis of upregulated genes in mouse and human pathological hearts (**Fig. 1A**). Cytoscape 3.7.2 software *(92)* was used to analyze the enrichment of gene annotation (GO terms) in GO networks or sub-networks on data obtained by RNA-seq. The Cytoscape plug-in ClueGO version 2.5.6 *(93)* was used to visualize the biological terms of genes clustered in functionally

grouped networks. The ClueGO plugin CluePedia version 1.5.6 *(94)*, was used to represent the genes and to integrate them in the ontology network primarily built with ClueGO. For the cellular component GO analysis of hnRNPC interactome in human healthy and pathological hearts (**Fig. 2D**), GO term fusion, GO-Tree interval of 4-10, p value ≤ 0,01 were selected as filters. The cellular component and biological process GO analysis of hnRNPC-RNAs targets obtained by RIP-seq GO term fusion, GO-Tree interval of 4-10, p value ≤ 0,05, were selected as filters.

The WikiPathways database *(95)* was used for pathway enrichment analysis performed on differentially spliced genes in hnRNPC silenced cells, and filtered by p-value ≤ 0.05. For all statistical analyses, the Kappa score was set to 0.3 and an Enrichment/Depletion (Two-sided hypergeometric test) test with Bonferroni pV correction was selected as an advanced statistical option in the software.

POSTAR2 database (http://lulab.life.tsinghua.edu.cn/postar/) was used to analyze transcripts which harbor hnRNPC binding sites.

To visualize the components of the Hippo pathway found among hnRNPC interactors by RIP-seq, iCLIPseq and the ones displaying altered AS in hnRNPC KD cells KEGG mapper *(96)* was used (**Data S6**). Comparative Toxicogenomics Database (CTD) *(97)* was used to detect the disease categories enriched using the list of transcripts common between the ones bound to hnRNPC in HF (RIP-seq analysis), the direct targets found by iCLIPseq and the transcripts displaying altered AS in hnRNPC KD cells (**Fig. 8**; **data file S8**).

14. Histology, immunohistochemistry and immunocytochemistry

After collection, human heart tissues were dissected in cold DPBS, fixed for 4-8 h in 4% PFA at 4°C, cryoprotected in 30% sucrose overnight at 4°C, embedded in Tissue Freezing Medium (Leica Biosystems) and snap frozen using a dry ice/isopentane cooling bath. Frozen tissues were cut into 5 µm-thick sections using a cryostat (Leica).

Murine hearts were fixed for 4-8 h in 10% formalin neutral buffer (10%) (VWR BDH & Prolabo), cryoprotected by 30% sucrose immersion, embedded in Tissue Freezing Medium and cut into 3 µm-thick slices using a cryostat (Leica).

All cryosections were thawed at 4°C and rehydrated with DPBS for 5 min at room temperature (RT). Tissue permeabilization was performed with 0.5% Triton X-100 for 10 min at room temperature. After blocking non-specific sites, primary antibodies were incubated overnight at 4°C (**table S2**).

For immunocytochemical analysis of adherent cells, fixation was performed in 4% PFA for 15 min at room temperature, followed by 5 min permeabilization in 0.2% Triton X-100 (Sigma-Aldrich) and 1 h blocking in 2.5% BSA in DPBS solution at room temperature (RT). Cells were incubated with primary antibodies (**table S2**) for 2 h at RT or overnight at 4 °C. After three washes with DPBS, the samples were incubated with the respective Alexa fluorochrome-conjugated secondary antibodies (ThermoFisher Scientific) for 1 h at RT. DAPI (Sigma-Aldrich) was used to counterstain the nuclei. Specimens were then mounted using anti-fade Mowiol 4-88 mounting media (Sigma-Aldrich) plus DABCO (Sigma-Aldrich). Masson's Trichrome (Sigma-Aldrich) staining was performed according to the manufacturer's instructions using celestine blue (Sigma- Aldrich) and bouin's solution (VWR Chemicals).

15. Proximity Ligation Assay

The proximity ligation assay (PLA) was performed on fixed heart tissue slices or on fixed cells using DuoLink PLA technology probes and reagents (**table S2**), according to the manufacturer's protocol. Fixed samples were permeabilized with 0.5% Triton X-100 in PBS for 10 min (tissue slices) or 0.2% Triton X-100 in PBS for 5 min (cells). The samples were then washed three times with PBS and incubated with blocking solution for 1 h at 37°C in a humidified chamber. Primary antibodies were prepared in antibody diluent and incubated overnight at 4°C (**table S2**). The samples were washed twice with buffer A for 5 min and then incubated with the PLA probes (anti-mouse MINUS and anti-rabbit PLUS) in antibody diluent for 1 h at 37°C. After two washes for 5 min each with buffer A, a ligation step was performed by incubating the samples with ligase enzyme diluted in ligation buffer for 30 min at 37°C in a humidified chamber. After 2 washes of 5 min each with buffer A, the samples were incubated with polymerase enzyme diluted in amplification buffer for 100 min at 37°C, in humid chamber. After two washes for 10 min each with buffer B, and a final wash of 1 min with 0.01% of buffer B, the slides were mounted with Duolink *in situ* mounting medium containing DAPI. Each experiment was performed with a pair of antibodies of different species (mouse and rabbit). Negative control experiments were performed where only one antibody or none were incubated with the PLA probes.

16. Image analysis

A Zeiss LSM 780 confocal microscope with × 40 (1.3 NA) oil-immersion or x 20 air (0.8 NA) objective lenses were used for immunostaining read-out acquisition. Z-stack images were acquired with the optimal interval suggested by the software, followed by the application of maximum intensity algorithm. For the Masson's Trichrome analysis, a slide scanner Zeiss Axio Scan Z1 microscope was used to visualize the whole tissue in bright-field mode and through a x10 objective. Super-resolution imaging was performed using a 3D-SIM Deltavision OMX with x 60 objective (1.42 NA) using 524 oil. Expression profiles were obtained by RGB profiler using ImageJ software.

16.1 PLA quantification

For each experiment and respective conditions, a minimum of six Z-stacks were acquired with a confocal microscope and a x40 oil objective. The same confocal acquisition settings were used within the same experiment. PLA dots quantification was performed using ImageJ software as follows: 10 regions of interest (ROIs) of the same size were defined for each Z-stack, a threshold of 50-150 (signal histogram) was set on the red channel (PLA signal) and all the slices of the Z-stack were processed as binary and watershield. The dots in the ROIs were quantified using the "3D Object counter".

16.2 Co-localization analysis

Co-localization analysis was performed using Imaris 9.0 software. For each experiment a minimum of four Z-stacks *per* condition were acquired with a confocal microscope and a x40 oil objective. The same confocal acquisition settings were used across the experiment. A mask was applied to the channel corresponding to the sarcomeric structure (TNNT2) and automatic threshold was selected. Co-localization channel statistics were then automatically calculated by Imaris software. The threshold, the colocalization channel and the colocalization coefficient (Pearson's r) were calculated by Imaris software.

17. Individual-nucleotide resolution UV crosslinking and immunoprecipitation (iCLIP) of HNRNPC1/C2

17.1 Cell culture and crosslinking

Normal Human Dermal Fibroblasts (NHDFs) were grown in DMEM supplemented with FBS to 85-90% confluency. Three 150mm tissue culture dishes were used for each replicate of iCLIP. Cells were washed briefly with ice cold 1x PBS and exposed to 150 mJ/cm^2 at 254 nm in a Stratalinker 2400 on ice. The cells were harvested by scraping, washed with 1x ice cold PBS. Pooled pellets from three

dishes were flash frozen in liquid nitrogen and stored at -80°C until further use. Pellets were thawed and resuspended in 1ml of ice-cold lysis buffer (50 mM Tris-HCl, pH 7.4; 100 mM NaCl; 1% NP-40; 0.1% SDS; 40 U / ml of RNase inhibitor, 1x CompleteMini Protease Inhibitor Cocktail (Roche)), the suspension was passed through g20 syringe and incubated 10 min on ice. The insoluble fraction was removed by centrifugation at 20.000g for 20 min at 4°C and the supernatant was used for the iCLIP experiments.

17.2 iCLIP

100 µl of Protein G Dynabeads (Invitrogen) were coupled with 15 µg of anti HNRNPC1/C2 antibody (Santa Cruz) in a total volume of 100 µl of lysis buffer for 1 h at RT. The beads were washed two times with 1ml of low salt wash buffer (LSWB; 50mM Tris pH 7.4, 150mM NaCl, 0.02% NP-40, 1mM DTT, 1x CompleteMini Protease Inhibitor Cocktail), two times with 1ml of high salt wash buffer (HSWB 50mM Tris pH 7.4, 1M NaCl, 1mM EDTA, 1% NP-40, 0.1% SDS, 1x CompleteMini Protease Inhibitor Cocktail) and two times 1ml lysis buffer. Prior to protein IP, the beads were incubated for 1h at 4°C in lysis buffer containing 0.1 mg/ml heparin (Sigma-Aldrich) and washed as previously mentioned.

Antibody coupled beads were mixed with 1 ml of soluble cell lysate and incubated for 1hour on a rotator at 4°C. The unbound fraction was collected on a magnetic stand. The beads were consequently washed three times with 1ml of LSWB, HSWB and PNK buffer (100mM Tris pH 7.4, 50mM NaCl, 10mM EDTA), each time for 10 min at 4°C with rotation.

The beads were transferred into fresh tubes and resuspended in 500 µl of LSWB supplemented with 0.2 units of RNase I, 5 min at 37°C, with agitation at 1100 RPM. The reaction was stopped by incubation on ice and the beads were subjected to an additional round of high stringency washing. The bound fractions were treated with two units of alkaline phosphatase (Fast-AP, Thermofisher) in 1X FastAP buffer in a reaction volume of 25 µl and incubated 20 min at 37°C. 1/10V of the beads were incubated with 8µl of radiolabelling mix (0.4 µl T4 PNK (NEB); 0.8 µl 32P-γ-ATP; 0.8 µl 10x PNK buffer (NEB)) for 20 mins at 37°C at 1100 RPM, for reference purpose and the rest of the beads were incubated with 20 µl of cold ATP mix (1µl T4 PNK, 1mM ATP, 20µl 10x PNK buffer). 20µM of L3App adapter *(73)* was ligated to the bound RNA in a final volume of 20µl ligation mix (1x RNA ligase buffer, 5% PEG400 (Sigma-Aldrich), 20 Units RNase inhibitor and 10 Units T4 RNA Ligase 2 (truncated) (NEB). The ligation reaction was incubated overnight at 16°C while rotating at 1100 RPM.

The beads were washed with 1ml of HSWB and after each wash transferred to fresh non-sticky 1.5 ml eppendorf tubes to get rid of any non-ligated linkers.

The protein-RNA complexes were eluted by adding 20 µl of 1X NuPAGE loading buffer supplemented with 1x NuPAGE reducing agent and incubating 5 min at 90 °C. The eluted proteins and protein-RNA complexes were resolved by 4-12% gradient SDS-PAGE (NuPAGE, Invitrogen). The region above the migration position of the free protein till the position migrating at 100KDa was cut from the nitrocellulose membrane post transfer and subjected to proteinase K treatment (100mM Tris pH 7.4 50mM NaCl, 10mM EDTA, 100u proteinase K) for 20 min at 37°C. The reactions were stopped with 1V of Urea buffer (100mM Tris pH 7.4, 50mM NaCl, 10mM EDTA, 7M Urea) and incubated for additional 20 min. RNA was purified by adding equal volumes of Phenol chloroform isoamylalcohol and precipitated with 3V of 100 % ethanol overnight at -20°C.

17.3 cDNA library preparation and sequencing

The cDNA libraries were prepared as previously described *(98)* with slight modifications. Briefly, RNA pellets were washed 2x with ice cold 80% ethanol and resuspended in 8µl of RT annealing mixture (Rt1iClip, Rt2iClip and Rt3iClip-0.5µM each, 1mM dNTPs) (**table S2**). The samples were denatured three min at 70°C and cooled to 25°C for 10 min. 12 µl RT reaction mix was added (1x first strand buffer, 5mM DTT, 200u SSIII) and reverse transcription reaction was carried out in a thermal cycler (25°C for 20 min, 42°C for 30 mins, 50°C for 45 mins, 90°C for 3 mins).

The samples were snap-chilled on ice and passed through the QIAquick columns (QIAGEN) following the manufacturer's protocol. DNA was eluted in 20µl ddH2O. DNA circularization was carried in a final reaction volume of 40 µl of the circligaseII reaction mix (1X CircLigase Buffer II (Lucigen), 500mM MnCl2, 60U CircLigase II (Lucigen)) at 60°C for 1hour. The circularised samples were supplemented with oligo annealing mix (11µl ddH2O, 4.5µl 10x Fast digest buffer (Thermofisher), 1.5µl Cut-Oligo **(table S2)**. The samples were incubated 4 min at 95°C and the temperature was subsequently reduced by 1°C every 30 seconds till final temperature of 25°C. Post hybridization the reaction mix was supplemented with 3µl of BamHI and incubated for 1hour at 37°C. Linearized cDNA was further purified using the QIAquick columns and eluted in final volume of 28 µl. cDNA PCR amplification was carried out with P3/P5 primer mix (1mM each) and 1x Phusion Flash High-Fidelity PCR Master Mix (Thermofisher). The PCR products were resolved by a 4% metaphor agarose gel electrophoresis and the fragments of 180-300 bp were excised and purified by QIAquick gel

purification following the manufacturer's protocol. The resulting DNA libraries were quality checked on a bioanalyzer. The libraries were pooled in equimolar concentration and analysed by 75bp single end high-throughput sequencing at Illumina HiSeq2500. A schematic representation of the protocol can be found in **fig. S8A**.

17.4 iCLIP-seq analysis

The iCLIP libraries contained 5-nt random Unique molecular identifier sequence and 4-nt sample barcode, allowing for demultiplexing of samples as well as for PCR duplicates removal. We gathered about 250 million of reads across three replicates. Quality check of raw fastq reads was carried out by FastQC *(79)*. The adapters and quality trimming of raw fastq reads was performed using Trimmomatic v. 0.36 *(80)* with settings CROP:250 LEADING:3 TRAILING:3 SLIDINGWINDOW:4:5 MINLEN:20 and adapter sequences AGATCGGAAGAGCGG, ATCTCGTATGCCGTC, GGGGGGGGGGGGGGG were removed using ILLUMINACLIP setting. Trimmed iCLIP-Seq reads were mapped against the human genome (hg38) and Ensembl GRCh38 v.91 annotation using STAR v. 2.5.3a *(81)* as splice-aware short read aligner and default parameters except --outFilterMismatchNoverLmax 0.1 and --twopassMode Basic. Quality control after alignment was performed using several tools namely RSeQC *(82)*, Picard toolkit (GitHub Repository. http://broadinstitute.github.io/picard/) and Qualimap *(83)*. Unique molecular identifiers were extracted and used for PCR duplicates removal using UMI-tools v. 0.5.5 *(99)*. Counts and ratio of raw reads, trimmed reads, uniquelly/multimapped reads and deduplicated reads can be found in **data file S7**.

17.5 Identification of genomic crosslink sites

To obtain genomic crosslink sites, only uniquely mapped and deduplicated reads were used, to avoid an uncertainty of ambiguously mapped reads. Uniquelly mapped and deduplicated reads were converted into bedgraphs genomic coverage tracks using deeptools bamCoverage v. 3.3.0 *(100)* with settings -of bedgraph --binSize 1 --normalizeUsing None. Bedgraphs were further normalized on number of mapped reads per million (CPM). All of the covered positions were filtered in a way to keep only these regions, where there is more than one uniquelly mapped deduplicated read, to get rid of bias from possible random false positive mapping. All crosslink sites that were closer than 5 bases to each other were merged together to create more robust binding sites. All binding sites were annotated employing Ensembl GRCh38 v.91 annotation file. As a binding site were considered

all crosslink regions which appeared in at least 2 out of 3 replicates. Altogether we observed 13,567 crosslink sites, affecting 5,536 different genes and 2,988 intergenic regions.

For the visualization of binding sites in a close proximity of observed skipped exons all binding sites were averaged across all replicates and visualize in Integrative genomics viewer *(101)*.

To assess the ratio between binding sites in coding and non-coding regions, counts, produced using featureCounts tool *(85)* with settings -s 1 -T 10 -F GTF -Q 0 -d 1 -D 25000 and calculated over feature "gene" including all parts of gene region specified in annotation file - intronic parts of gene are included as well, were adopted. All genomic counts were again annotated using Ensembl GRCh38 v.91. As a non-coding features were considered all records with gene_biotype falling into this list: "3prime_overlapping_ncRNA", "antisense_RNA","bidirectional_promoter_lncRNA", "lincRNA", "non_coding", "processed_transcript", "sense_intronic", "sense_overlapping", "miRNA","macro_lncRNA", "misc_RNA", "Mt_rRNA", "Mt_tRNA", "rRNA","scaRNA", "scRNA" , "snoRNA", "snRNA", "sRNA" , "tRNA", "tRNA_pseudogene","vaultRNA".

All intergenic binding sites were considered as non-coding as well. The rest of genomic counts were treated as coding regions. Based on the same counts and using gene_biotype list containing: lincRNA, Non-antisense_RNA, snRNA, Non-misc_RNA, bidirectional_promoter_lncRNA, snoRNA, rRNA, macro_lncRNA, 3prime_overlapping_ncRNA and miRNA, the counts and ratio within these annotated non-coding genomic features were derived (**fig. S7I; data file S7**).

Read counts of 4 specific genomic features (CDS - exons without UTR regions, introns, 3'UTR and 5'UTR) were gathered using featureCounts and were again based on modified Ensembl GRCh38 v.94 annotation GTF file described in RIP-Seq methods part. All iCLIP sample counts were normalized on sequencing library depth (CPM) .

We used Alu elements annotation based on RepeatMasker predictions (Smit, AFA, Hubley, R & Green, P. RepeatMasker Open-4.0. 2013-2015; http://www.repeatmasker.org) to obtain crosslink sites on the total of 1,131,306 Alu elements. Only deduplicated reads without filtering of multimapped reads were converted into bed files using deeptools bamCoverage. These bed files were further intersected with bed file of Alu elements annotated regions utilizing bedtools intersect v. 2.23.0 *(102)*. We considered all annotated Alu elements with any mapped read as covered Alu and the rest as Not-covered Alu (**fig. S8D**).

All Pie plots were produced using R package plotrix *(87)* and all barplots plotted using R package ggplot2 *(86)*.

17.6 iCLIP-PCR validation assay

NHDFs were crosslinked at 150mJ/cm^2 UV and lysed using 3X pellet volume of lysis buffer supplemented with RNAse inhibitor and protease inhibitor. The pull down was carried out on three biological replicates as described for the iCLIP assay (see 17.1), excluding the RNAse treatment step. Post IP, the beads were subjected to DNAse treatment to remove genomic DNA contamination, followed by 3' linker ligation and proteinase K treatment to release the bound RNA. Immunoprecipitation with FLAG antibody was used as negative control. Total RNA isolated from lysates were used as positive controls.

Supplementary Figures:

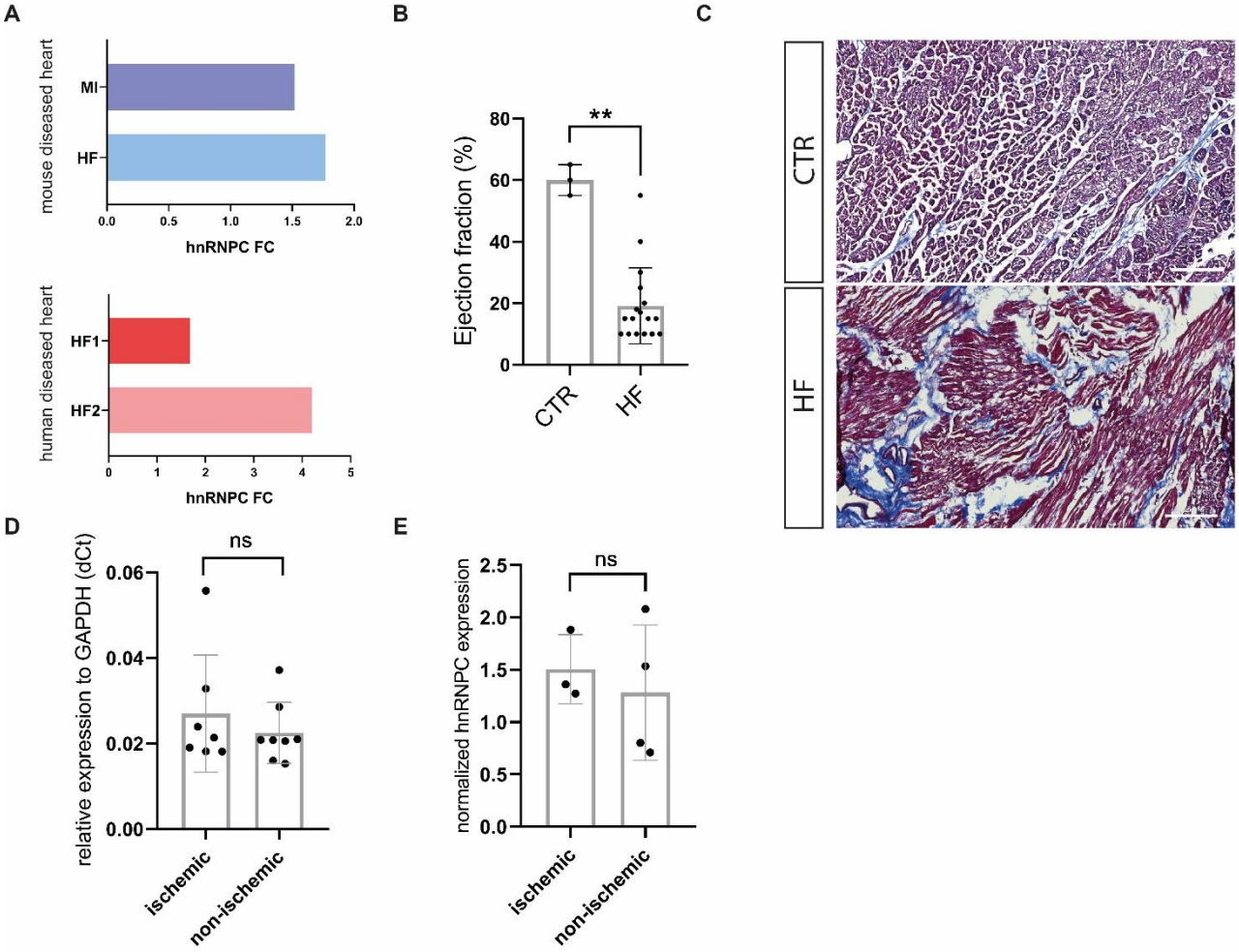

fig. S1. **Expression of hnRNPC in the heart**. (**A**) Top: Barplot representation of hnRNPC expression in mouse diseased heart datasets. Bottom: hnRNPC expression in human diseased heart failure (HF) datasets. The data are expressed as fold change (FC) as compared to their respective control. (**B**) Ejection fraction representation of the patients enrolled in the study. ***P* < 0.01, Mann-Whitney test. Healthy (N = 3); heart failure (HF, N = 17). (**C**) Representative Masson's Trichrome staining of human heart tissue. Collagen, blue; muscle fibers, red. Scale bar = 500 µm. (**D**) Dotplot representation of hnRNPC RNA expression in ischemic HF (N = 7; n = 2) compared to non-ischemic heart tissues (N = 8; n = 2) as obtained by RT-qPCR analysis. (**E**) Dotplot representation of hnRNPC protein expression in samples of ischemic (N = 3; n = 3) and non-ischemic (N = 4; n = 3) heart tissues as obtained by western blot (see also **Fig. 1D**). GAPDH was used for total protein loading normalization. Data are shown as means ± SD.

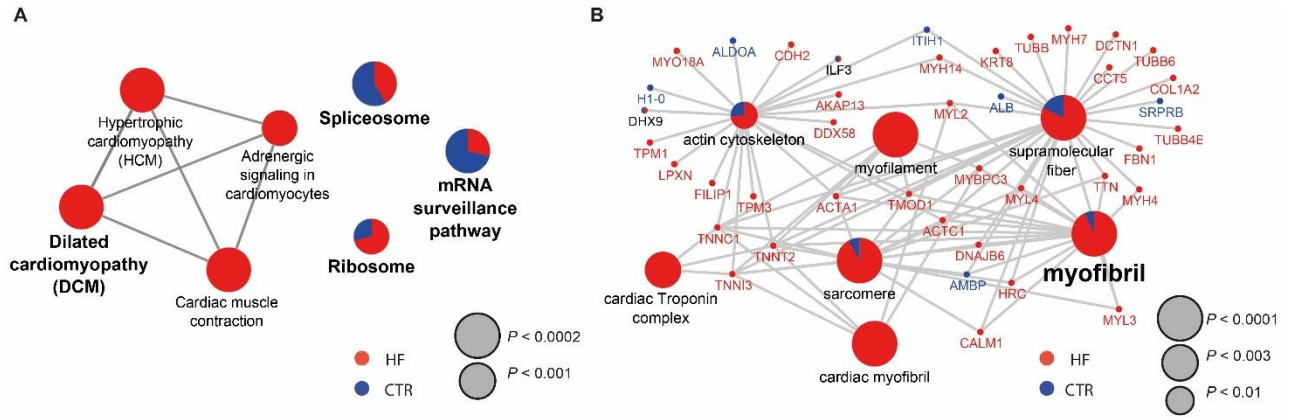

fig. S2. Bioinformatic analysis of hnRNPC interactors in the heart. (**A**) Network of the pathways found enriched in failing (N = 2) (red) or healthy (N = 2) (blue) hearts based on KEGG database. The size of the nodes indicate the Bonferroni adjusted Term p-values. (**B**) Gene-ontology (GO) network representation of the myofibril cluster found significantly [Group p-value (corrected with Bonferroni): 1.31E-08] enriched in failing (HF, blue) heart tissue. The proteins belonging to each node and found in hnRNPC-IP are depicted. The size of the nodes indicate the Bonferroni adjusted Term p-values.

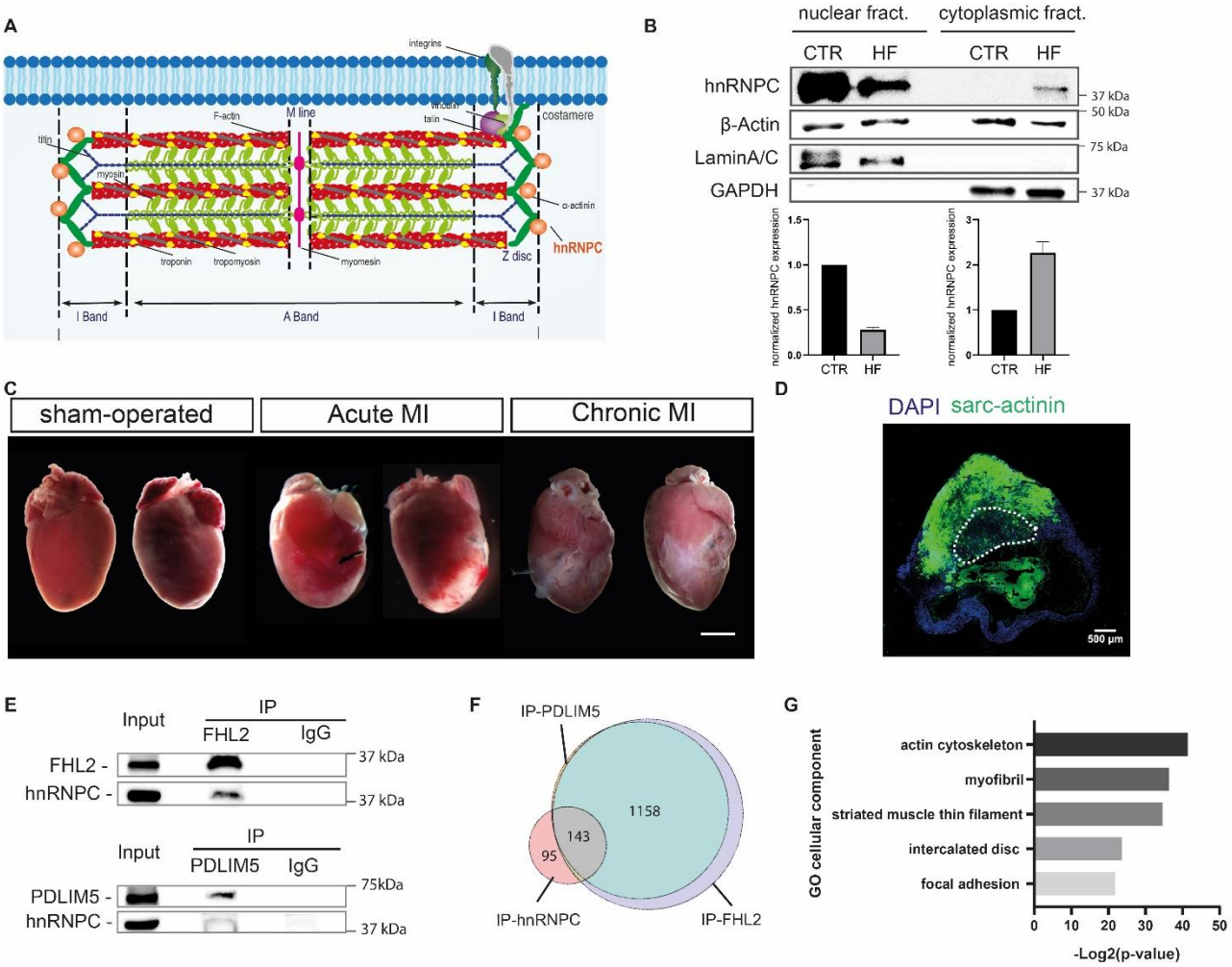

fig. S3. hnRNPC relocates to the z-disk in diseased heart. (**A**) Schematic representation of the sarcomere structure and hnRNPC distribution (orange beads). (**B**) Western blot analysis (top) and quantification (bottom) of hnRNPC expression in nuclear and cytoplasmic fractions of healthy and diseased (HF) human hearts. β-actin was used for loading normalization. Lamin A/C and GAPDH were used to validate the fractionation protocol. Band intensities corresponding to hnRNPC in the nuclear and cytoplasmic fractions were quantified using Bio-Rad Image Lab software. Data are presented as mean ± S.D. (N = 2). (**C**) Representative images of hearts collected from a mouse model of myocardial infarction (MI) 4 days post-surgery (Acute MI) or 21 days post-surgery (Chronic MI) and sham-operated mice. Scale bar = 200 mm. (**D**) Representative confocal image of a transverse mouse heart section 21 days post-MI (Chronic MI). The frozen section was stained for sarcomeric actinin (sarc-actinin, green) and counterstained with DAPI. The dashed line indicates the infarct border zone. Scale bar = 500 µm. (**E**) Western blot analysis of hnRNPC co-immunoprecipitation with FHL2 and PDLIM5 in diseased human heart (total lysate), FHL2- and PDLIM5- immunoprecipitated samples and negative control (IgG). (**F**) Venn diagram representation of the proteins found interacting with hnRNPC, PDLIM5 and FHL2 in immunoprecipitated samples in failing human hearts. (**G**) Barplot representation of cellular components Gene Ontology (GO) categories significantly enriched in the binding partners common to hnRNPC, PDLIM5 and hnRNPC in the failing human heart.

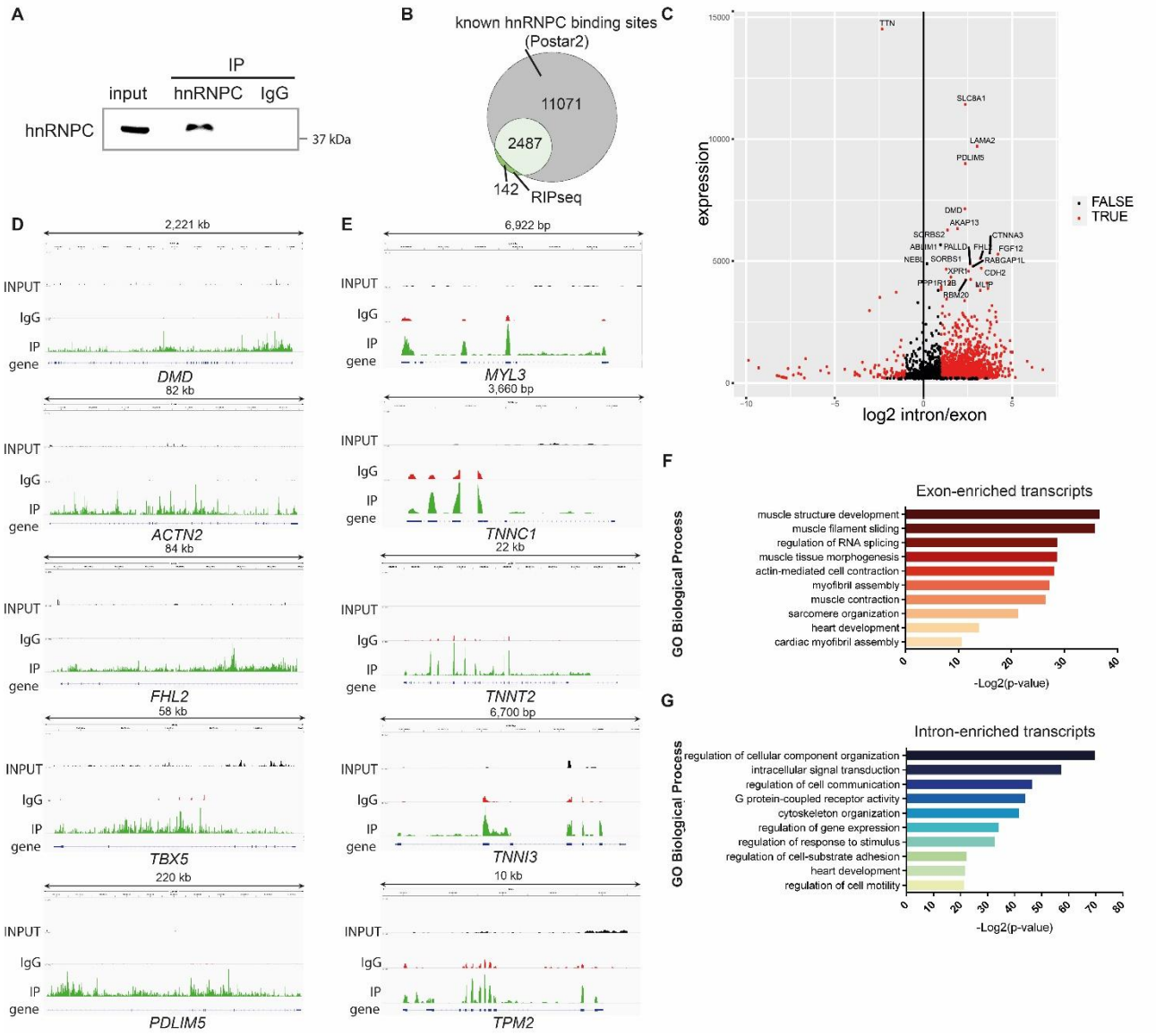

fig. S4. **hnRNPC binds mRNAs coding for sarcomeric components in the failing heart.** (**A**) Western blot analysis of hnRNPC protein in the total human failing heart lysate (input), the hnRNPC immunoprecipitated sample and the negative control (IgG) following a RIP-seq protocol. (**B**) Venn diagram representing the transcripts enriched in hnRNPC-immunoprecipitated samples over the input (green) and the transcripts harboring at least one binding site for hnRNPC, collected from the POSTAR2 database (grey). (**C**) Volcano plot representing the transcripts found enriched in hnRNPC immunoprecipitated samples over the input. The x-axis shows the intron-exon ratio on a logarithmic scale: $\log_2$ (intron/exon) < -1 indicates exons-enriched transcripts whereas $\log_2$ (intron/exon) > 1 indicates introns-enriched transcripts. (**D**) Individual gene representation of representative intron-enriched hnRNPC targets. Read coverage is displayed in INPUT (black), IgG (red) and IP (green) samples. (**E**) Individual gene representation of representative exon-enriched hnRNPC targets. Read coverage is displayed in INPUT (black), IgG (red) and IP (green) samples. (**F**) Gene Ontology (GO) of the biological processes of interest found significantly enriched (P < 0.01) in exons-enriched RNAs bound to hnRNPC in failing heart tissue. (**G**) GO of biological processes of interest found significantly enriched (P < 0.01) in introns-enriched RNAs bound to hnRNPC in failing heart tissue.

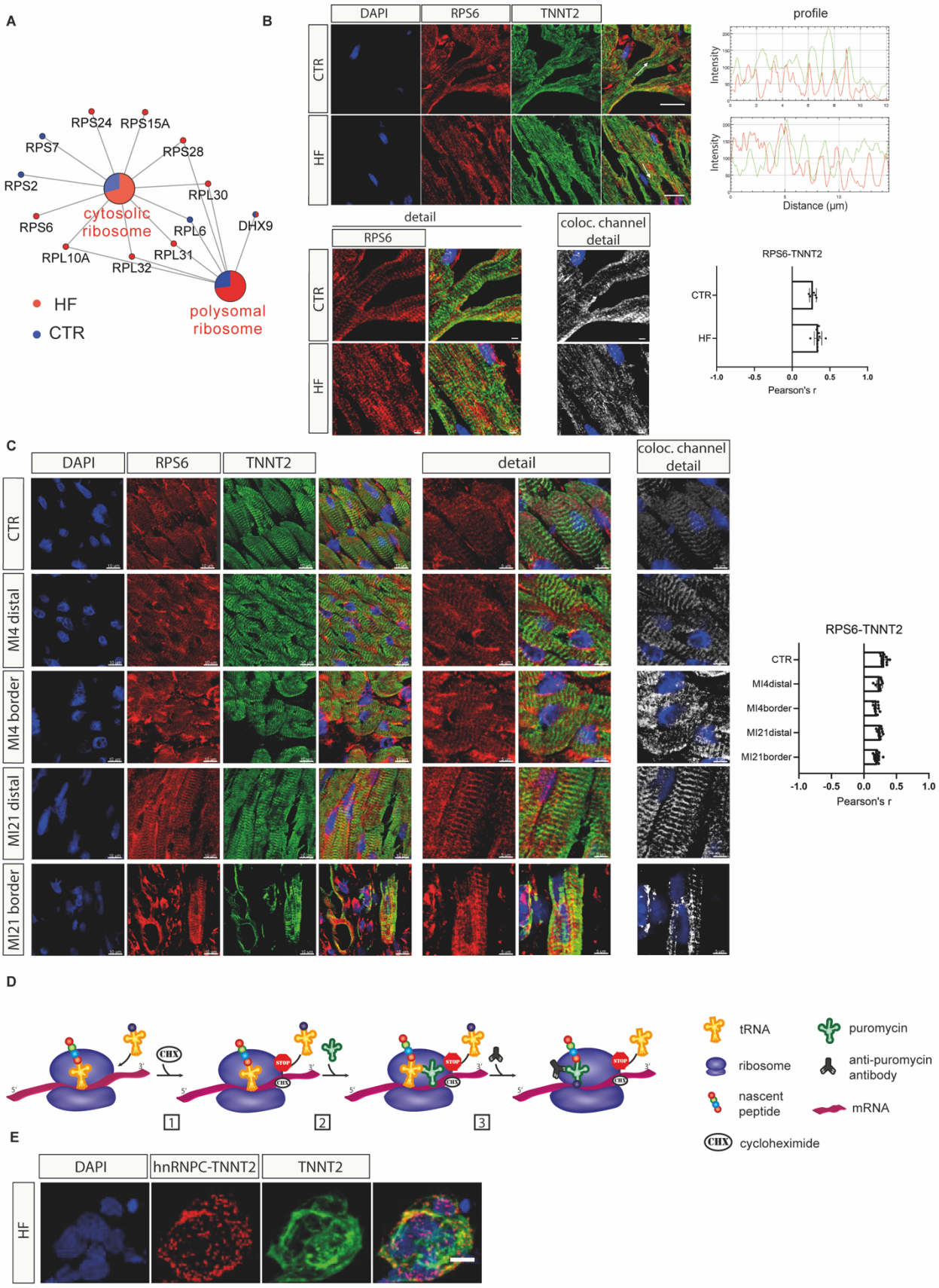
A
RPS24
RPS15A
RPS7
RPS28
RPS2
RPL30
cytosolic ribosome
RPS6
RPL6
DHX9
RPL10A
RPL31
RPL32
HF
CTR
polysomal ribosome
B
DAPI
RPS6
TNNT2
CTR
HF
profile
Intensity
Distance (µm)
detail
coloc. channel detail
RPS6-TNNT2
Pearson's r
C
DAPI
RPS6
TNNT2
detail
coloc. channel detail
CTR
MI4 distal
MI4 border
MI21 distal
MI21 border
RPS6-TNNT2
MI4distal
MI4border
MI21distal
MI21border
Pearson's r
D
CHX
STOP
1
2
3
tRNA
ribosome
nascent peptide
cycloheximide
puromycin
anti-puromycin antibody
mRNA
E
DAPI
hnRNPC-TNNT2
TNNT2
HF

fig. S5. **hnRNPC associtaes with active sites of translation at the sarcomeres in the failing heart.** (**A**) GO network representation of the cytosolic and polysomal ribosome categories (GO cellular component) found enriched ($P < 0.01$) in hnRNPC protein interactome in healthy (blue) and failing (red) heart. (**B**) Representative confocal microscopy images of ribosomal protein S6 (RPS6) (red) expression in healthy and failing (HF) human heart. Sarcomeric units are identified by cardiac troponin T (TNNT2, green) staining and nuclei are counterstained with DAPI (blue). Image analysis shows the intensity profiles of RPS6 and TNNT2 in representative cells. The superimposed white arrow indicates the region of interest. Bottom: the detail shows the colocalization (white) of red and green signals. Pearson's coefficient was calculated by IMARIS (n≥5). Scale bar = 10 µm; Scale bar of detail: 5 µm (**C**) Representative confocal images showing the localization and relative profile of RPS6 (red) in healthy and border or distal areas of the infarcted mouse heart (MI). Cardiomyocytes are stained with cardiac troponin T (TNNT2, green) and the nuclei are counterstained with DAPI (blue). The detail shows the colocalization (white) of red and green signals. Pearson's coefficient was calculated by IMARIS (n≥10). Scale bar = 20 µm. Scale bar detail = 8 µm. (**D**) Schematic of the strategy adopted to identify sites of active protein translation in iPSC-derived cardiomyocytes by means of ribopuromycilation assay: 1) elongation inhibition, 2) puromycin incorporation, 3) puromycin detection. (**E**) Representative confocal microscopy images of iPSC-derived beating cardiomyocytes grown onto HF decellularized heart matrices and stained by PLA using antibodies against hnRNPC and TNNT2 (red dots represent the close proximity between the two proteins). Cardiomyocytes are stained with cardiac TNNT2 (green) and the nuclei are counterstained with DAPI (blue). Data are shown as means ± SD.

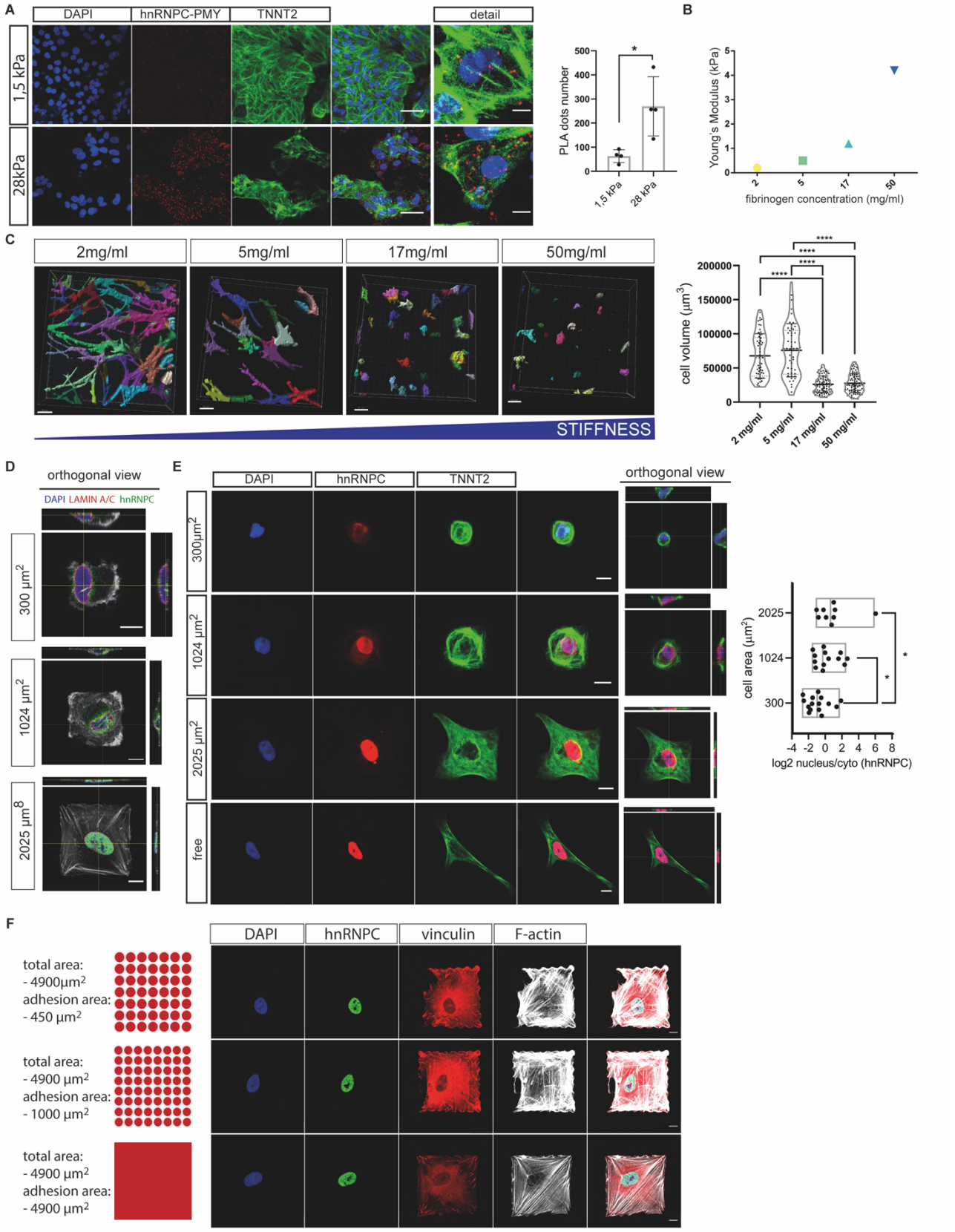

fig. S6. hnRNPC shuttling is mechanically regulated. (**A**) Representative confocal microscopy images of the results obtained from PLA using antibodies against PMY and hnRNPC in iPSC-derived beating cardiomyocytes grown onto

substrate with stiffness of 1.5 and 28 kPa. Cardiomyocytes are labeled for cardiac troponin T (TNNT2, green). The red signal identifies that the proteins are within 40 nm of each other. Nuclei are counterstained with DAPI (blue). (N =4 ; n = 5). * $P < 0.05$, Mann-Whitney test. Scale bar = 10 µm. (**B**) The Young's modulus (kPa) corresponding to the fibrin hydrogels used as calculated in Duong et al.,2009*(51)*. (**C**) A 3D reconstruction (left) and cell volume measure (right) of the NHDF cells embedded in fibrin hydrogels with different stiffnesses, calculated using Imaris software. (> 50 cells per condition) **** $P < 0.0001$; Kruskall Wallis test followed by Dunn's multiple comparisons test. (**D**) Orthogonal view of the representative confocal images showing the hnRNPC distribution in cells confined on fibronectin-coated squares with the indicated areas. The cells were stained with anti-hnRNPC (green), Alexa Fluor 647 Phalloidin, anti-LaminA/C (red) and the nuclei were counterstained with DAPI (blue). (**E**) Representative confocal analysis of individual iPSC-derived cardiomyocytes grown onto 300 μm^2(N=2; n=15), 1024 μm^2 (N=2; n=13), 2025 μm^2 (N=2; n=9) micropatterns or without patterns (free) on a fibronectin coating (left) and hnRNPC nucleus/cytoplasm quantification (right). The cells were stained with anti-hnRNPC (red), cardiac Troponin T (TNNT2), and the nuclei were counterstained with DAPI (blue). Data are represented as doplot with median, the box is used to highlight the values distribution. * $P < 0.05$; Brown-Forsythe and Welch ANOVA tests corrected for multiple comparisons (Dunnett T3) (**F**) Left: Annotation of micropattern properties (cell area and adhesion area) and a schematic top view of the fibronectin distribution in the micropatterns. Red color indicates fibronectin-covered area. Right: Confocal images of single NHDFs grown onto the indicated micropatterns and labeled with anti-vinculin (red), anti-hnRNPC (green), Alexa Fluor 546 Phalloidin and DAPI (blue) (N = 3; n = 5). Data in A and C are shown as means ± SD. Data in D are presented as dotplot with median where the box is used to highlight the value distribution.

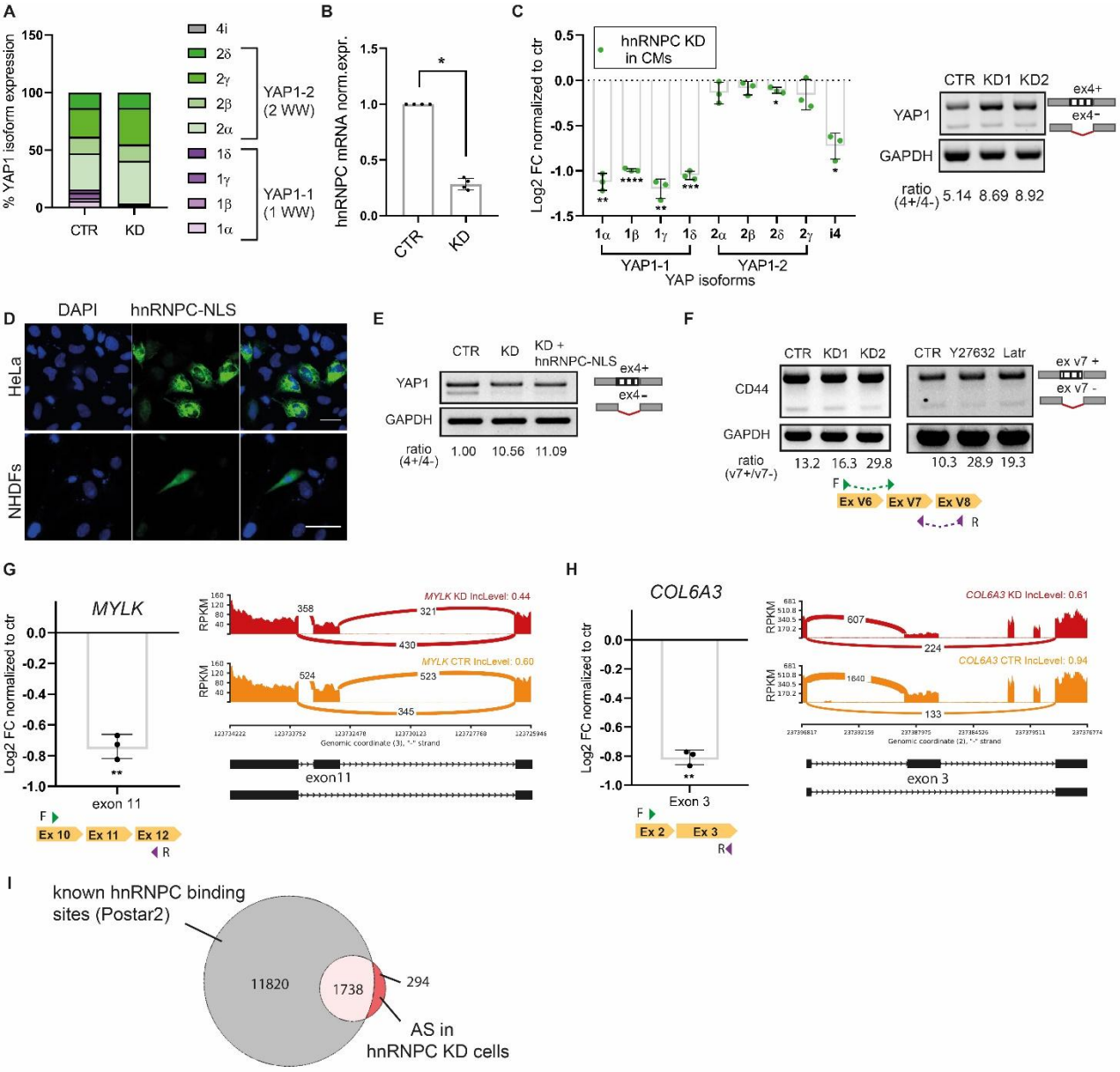

fig. S7. **hnRNPC depletion from cell nucleus affects the alternative splicing of mechanosensitive transcripts.** (**A**) Barplot representation of the relative expression of YAP1 splicing isoforms obtained by RT-qPCR in normal human dermal fibroblasts (NHDFs) depleted (KD) or not (CTR) for hnRNPC. The data are expressed as mean percentages of the indicated isoform ± S.D. and are normalized to GAPDH (N = 4). (**B**) RT-qPCR analysis of hnRNPC mRNA expression in iPSC-derived cardiomyocytes (iPSC-CMs) 96 h after transfection with hnRNPC (KD) or control siRNAs (CTR). (N = 4). *p < 0.05, Mann-Whitney test. (**C**) Left) Barplot representation of YAP1 isoforms mRNA expression (Log2FC) in iPSC-CMs upon hnRNPC-depletion. (N = 3) * $P < 0.05$; ** $P < 0.01$; *** $P < 0.001$; **** $P < 0.0001$; One-sample t-test. Right) RT-PCR of YAP1 in iPSC-CMs upon hnRNPC-depletion. Top band: exon 4-included YAP1 mRNA. Bottom band: exon 4-excluded YAP1 mRNA. (**D**) Representative confocal images of the cytoplasmic distribution of hnRNPC-NLS mutant in HeLa (top) and NHDF (bottom) cell lines. Top scale bar = 20 µm; Bottom scale bar = 50 µm (**E**) RT-PCR of YAP1 in HeLa upon hnRNPC-depletion (KD) and KD combined to the overexpression of hnRNPC-NLS mutant. Top band: exon 4-included YAP1 mRNA. Bottom band: exon 4-excluded YAP1 mRNA (**F**) RT-PCR of CD44 in NHDF upon hnRNPC-depletion (Top) or upon 24h

treatment with inhibitors of tension (Latrunculin and Y27632) (Bottom). Top band: variable exon 7-included CD44 mRNA. Bottom band: variable exon 7-excluded CD44 mRNA. (**G**) Left) Barplot representation of MYLK exon11 expression (Log2FC) in hnRNPC-depleted NHDFs. Data are normalized to GAPDH (N = 3). ** $P < 0.01$; One-sample t-test. Right) Sashimi plot depicting MYLK skipped exon (SE) AS event (exon 11) in hnRNPC KD cells. (**H**) Left) Barplot representation of COL6A3 exon3 expression (Log2FC) in hnRNPC-depleted NHDFs. Data are normalized to GAPDH (N = 3). ** $P < 0.01$; One-sample t-test. Right) Sashimi plot depicting representative COL6A3 skipped exon (SE) AS event (exon3) in hnRNPC KD cells. (**I**) Venn diagram representing the genes that displayed AS events in hnRNPC KD cells (red) and the transcripts harboring at least one binding site for hnRNPC collected from POSTAR2 database (grey). Data are shown as means ± SD.

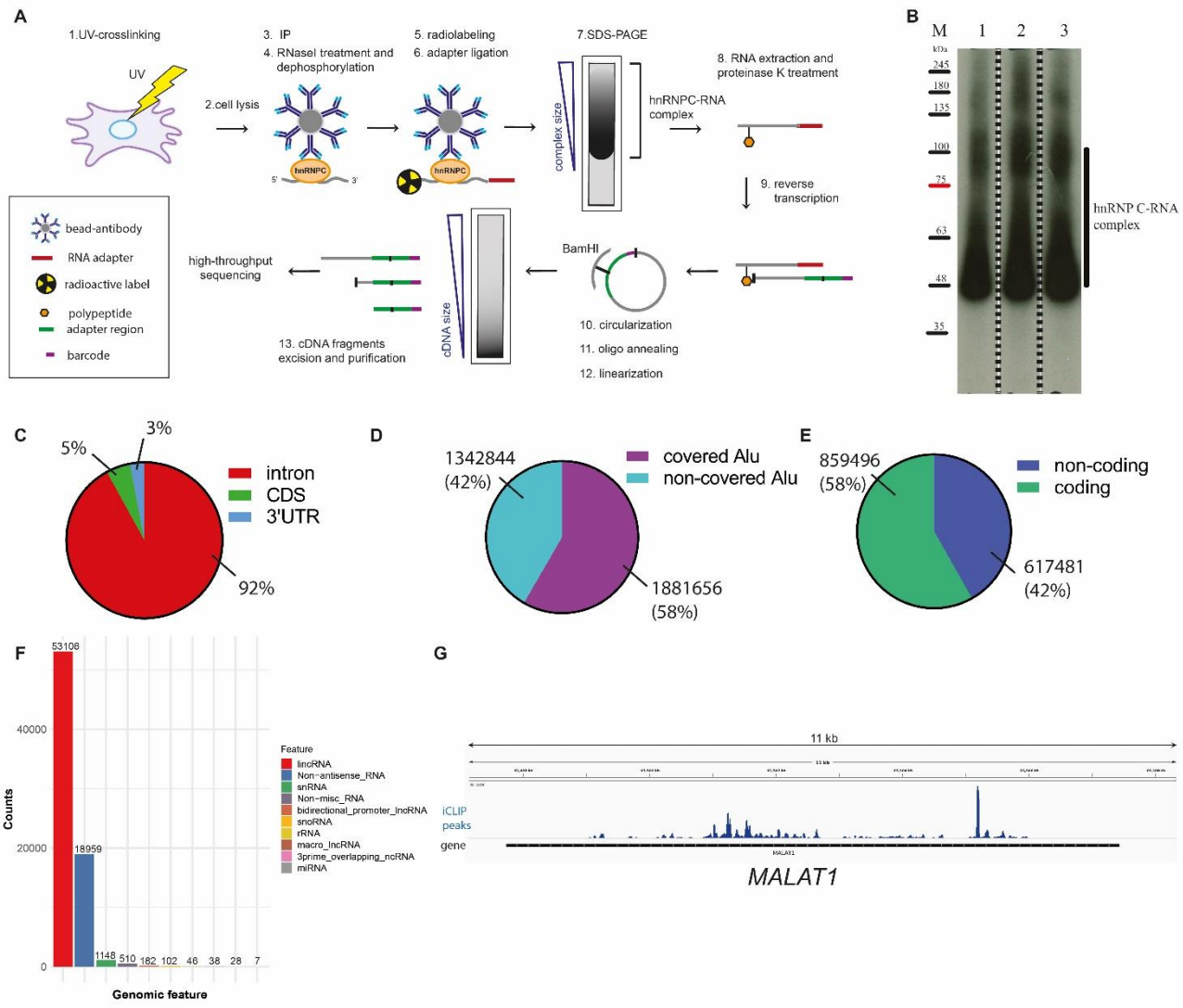

fig. S8. Validation of the iCLIP technology. (**A**) Graphical representation of the strategy adopted to identify hnRNPC RNA targets (N=3) in NHDF cells by iCLIP followed by sequencing. (**B**) Auto-radiography image of 10% IP beads used for labeling. (M) Molecular weight marker; (1)(2) and (3) Three replicates with protein RNA complex resolved on 4-12% gradient SDS PAGE. (**C**) Piechart representation of the genomic distribution of the read counts showing the percentage of reads mapping on specific genomic regions (intron/exon, 5'UTR, 3'UTR, CDS) in immunoprecipitated samples (N = 3). (**D**) Pie chart representation of read counts distribution on Alu elements in iCLIP samples (N = 3). (**E**) Pie chart representation of read counts distribution on coding vs non-coding elements in iCLIP samples (N = 3). (**F**) Bar plot representation of non-coding RNA categories bound by hnRNPC (N = 3). (**G**) Individual gene representation hnRNPC binding on MALAT1: the iCLIP averaged (N = 3) is shown in blue.

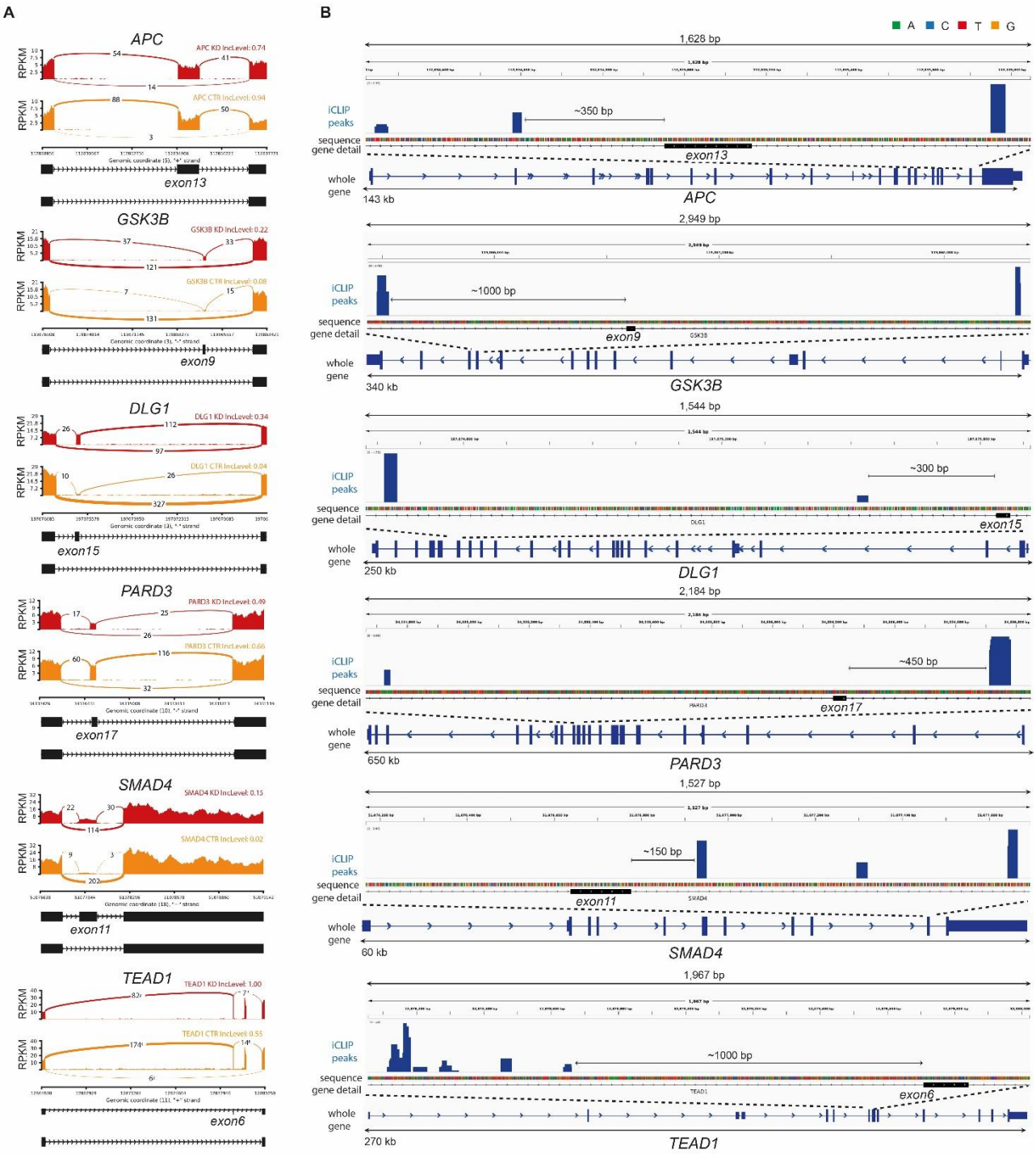

fig. S9. hnRNPC contributes to the splicing of transcripts coding for Hippo pathway components. (**A**) Sashimi plots depicting representative skipped exon (SE) AS events occurring in transcripts belonging to the Hippo pathway in hnRNPC KD cells NHDFs (red) and controls (orange). The exon inclusion level (IncLevel) is indicated. (**B**) Genome browser view of individual genes displaying the iCLIP data (crosslink events per nucleotide) of hnRNPC (blue) (average of N = 3) in proximity of specific exons.

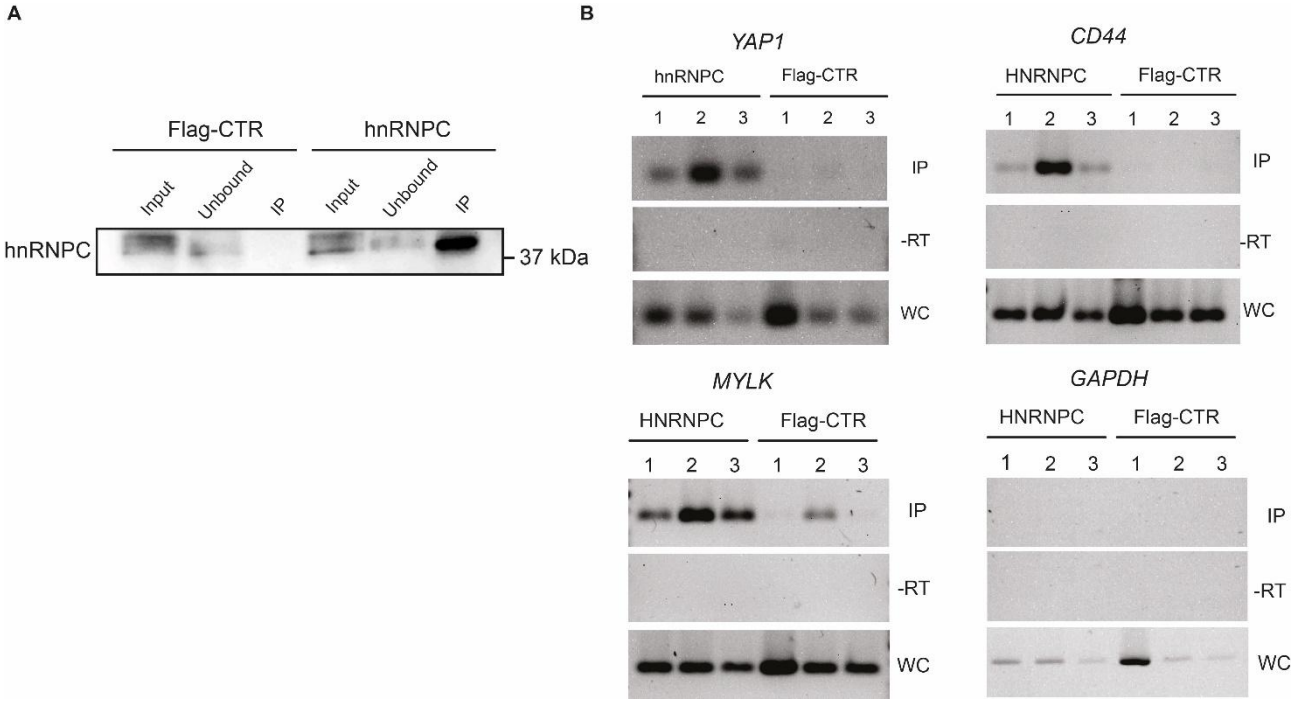

fig. S10. iCLIP validation of representative targets of hnRNPC. (**A**) Western blot analysis of hnRNPC protein in the total lysate of normal human dermal fibroblasts (input), in hnRNPC immunoprecipitated sample (IP) and unbound fraction following iCLIP protocol. Flag immunoprecipitation was used as negative control. (**B**) Analysis of the indicated transcripts in PCR-amplified iCLIP cDNA libraries. Whole cell lysates (WC) and Flag-immunoprecipitated samples were used as positive and negative controls, respectively. -RT represents the negative control in the absence of amplification.

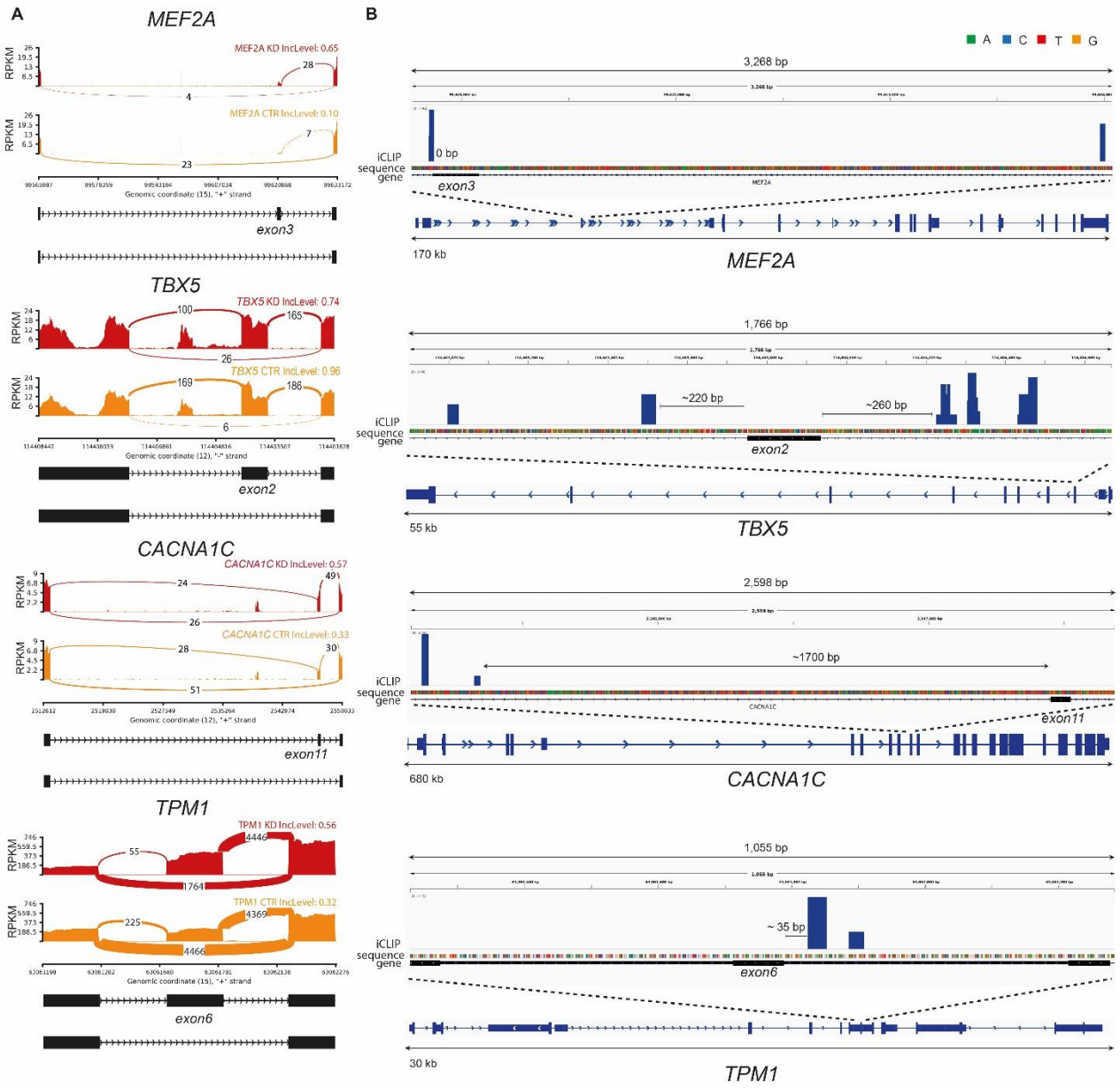

fig. S11. hnRNPC contributes to the splicing of transcripts involved in cardiovascular disease. (**A**) Sashimi plots depicting representative skipped exon AS events in *MEF2A*; *TBX5*; *CACNA1C* and *TPM1* belonging to Cardiovascular Disease category of the CTD database in hnRNPC KD NHDFs (red) and controls (orange). The exon inclusion level (IncLevel) is indicated. (**B**) Genome browser view of individual genes displaying the iCLIP data (crosslink events per nucleotide) of hnRNP C (blue) (average of N = 3) in proximity of specific exons. See also **data file S6 to 8**.

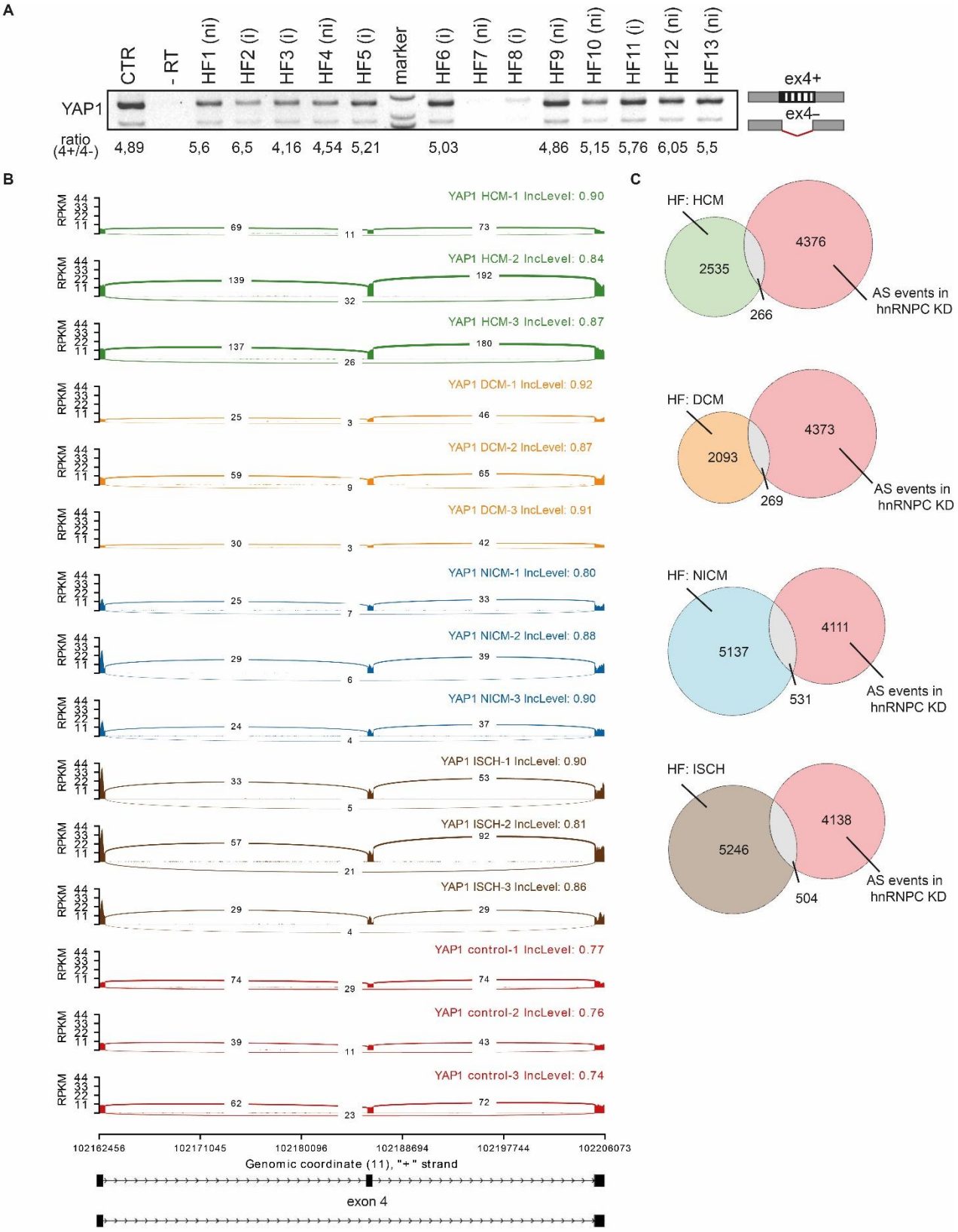

fig. S12. YAP1 alternative splicing is found in human failing heart. (A) RT-PCR of YAP1 in samples of human healthy and diseased (HF) hearts. HF (i) and HF (ni) indicate samples obtained from patients diagnosed with either ischemic or non-ischemic HF, respectively. Top band: exon 4-included YAP1 mRNA. Bottom band: exon 4-excluded YAP1 mRNA. -RT represents the negative control in the absence of amplification. **(B)** Sashimi plot depicting the inclusion level of YAP1

exon 4 in human healthy (control) or failing hearts. Failing hearts are obtained from patient diagnosed with hypertrophy (HCM) (GSE141910), dilated cardiomyopathy (DCM) (GSE141910), non-ischemic (NICM) (GSE108157), or ischemic cardiomyopathy (ISCH) (GSE108157). Healthy human hearts are obtained from the dataset GSE141910. **(C)** Venn diagram representations of the AS events determined by hnRNPC depletion in KD NHDF that are also found in failing human hearts (HCM, DCM, NICM, ISCH) and not in control heart. See also **data file S9**.

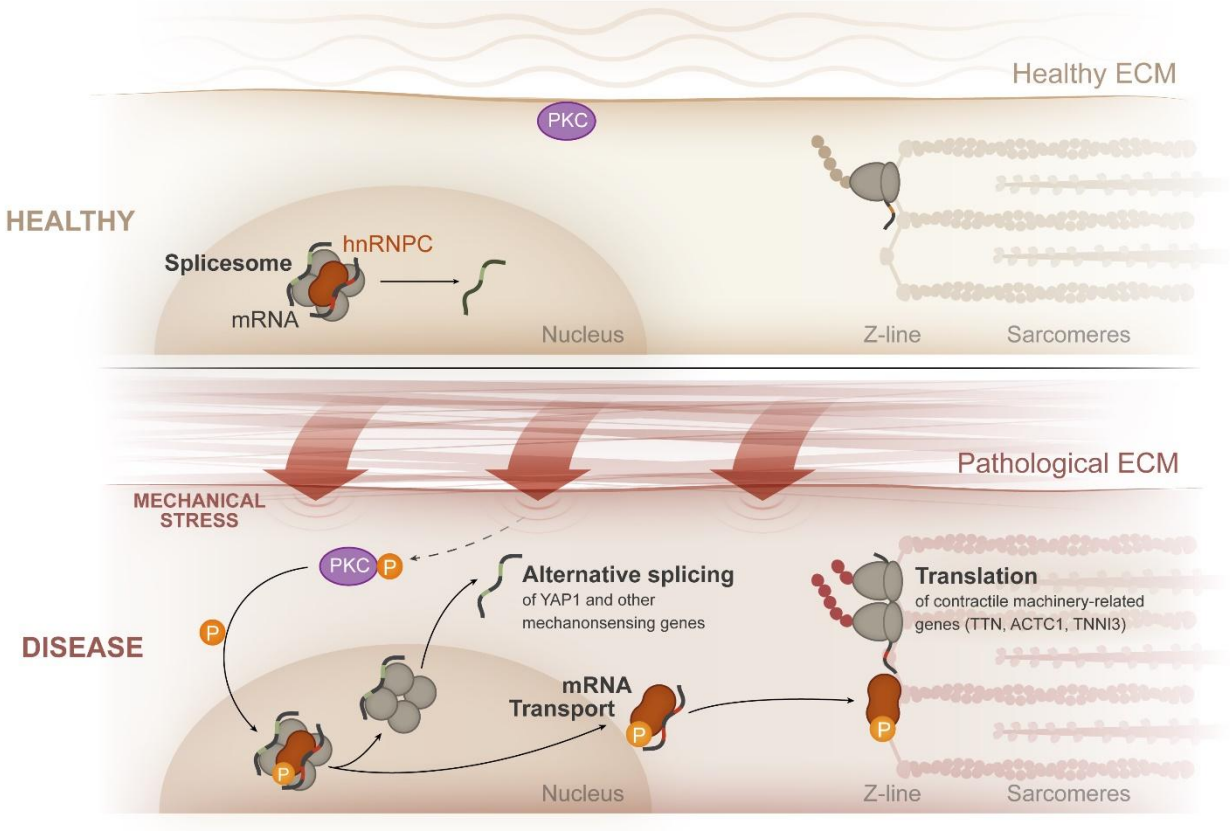

fig. S13: Graphical representation of hnRNPC displacement in the pathological heart.

Supplementary Tables

		Study groups	
		Control	**Heart Failure**
		N = 3	N = 17
	Actual surgery	Autopsy (100%)	LVAD (53%) Heart transplant (47%)
Physiology	**Age (years)**	52±3	53 ± 15
	Gender	M (100%)	M (88%) F (12%)
	BMI (kg/m^2)	25 ± 2	27 ± 5
	Heart rate (bpm)	80 ± 20	80 ± 16
	Ejection Fraction LV (%)	60 ± 5	19 ± 12
	NYHA I	n/a	0

Heart Failure Functional Classification (%)	**NYHA II**	n/a	6
	NYHA III	n/a	29
	NYHA IV	n/a	65
Cardiac pathologies (%)	**Arrhythmia**	n/a	71
	Congestive Heart Failure	n/a	65
	Ischemic Heart Disease	n/a	53
	Dilated Cardiomyopathy	n/a	65
	Danon disease	n/a	6

Table S1. Patients enrolled in the study. Data are presented as the ratio in percentage or mean ± SD. Abbreviations: F, female; LV, left ventricle; LVAD, left ventricular assist device; M, male; NYHA, New York Heart Association Functional Classification; n/r, not reported; n/a, not applicable.

REAGENT or RESOURCE	SOURCE	IDENTIFIER
Antibodies		
Mouse monoclonal anti-hnRNPC (4F4)	Santa Cruz Biotechnology	Cat# sc-32308, RRID:AB_627731
Rabbit monoclonal anti-hnRNPC (EP3034Y)	Abcam	Cat# ab75822, RRID:AB_1310320
Rabbit monoclonal anti-hnRNPC (EPNCIR152)	Abcam	Cat# ab133607, RRID:AB_2860560
Rabbit polyclonal anti-TNNT2	Sigma Aldrich	Cat# HPA017888, RRID:AB_1858355
Mouse monoclonal anti-alpha-actinin (EA-53)	Sigma-Aldrich	Cat# A7811, RRID:AB_476766
Rabbit polyclonal anti-FHL2	Proteintech	Cat# 21619-1-AP, RRID:AB_10860263
Rabbit polyclonal anti-PDLIM5	Sigma-Aldrich	**Cat# HPA016740, RRID:AB_1855153**
Mouse monoclonal anti-PDLIM5	Sigma-Aldrich	**Cat#WH0010611M1** RRID:AB_1842923
Mouse monoclonal anti-RPS6 (C8)	Santa Cruz Biotechnology	Cat# sc-74459, RRID:AB_1129205
Mouse monoclonal anti-PMY (12D10)	Millipore	Cat# MABE343, RRID:AB_2566826
Mouse monoclonal anti-Lamin A/C (4C11)	Sigma -Aldrich	Cat# SAB4200236, RRID:AB_10743057
Mouse monoclonal anti-YAP (SPM227)	Santa Cruz Biotechnology	Cat# sc-101199, RRID:AB_1131430
Mouse monoclonal anti-vinculin (63.7)	Abcam	Cat# ab18058, RRID:AB_444215
Mouse monoclonal Anti-β-Actin	Sigma-Aldrich	Cat# A2228, RRID:AB_476697

Normal mouse IgG	Santa Cruz Biotechnology	Cat# sc-2025, RRID:AB_737182
Normal rabbit IgG	Santa Cruz Biotechnology	Cat# sc-2027, RRID:AB_737197
Mouse monoclonal anti-Flag (M2)	Sigma-Aldrich	Cat# F3165, RRID:AB_259529
Rabbit polyclonal anti-MYH7	Cloud-Clone Corp.	Cat# PAD418Hu01
F-actin-Alexa Fluor 555	ThermoFisher Scientific	Cat# A34055
F-actin-Alexa Fluor 647	ThermoFisher Scientific	Cat# A22287, RRID:AB_2620155
GAPDH-HRP (GA1R)	Invitrogen	Cat# MA5-15738-HRP, RRID:AB_2537659
Chicken anti-mouse IgG-HRP	Santa Cruz Biotechnology	Cat# sc-2954, RRID:AB_639239
Chicken anti-rabbit IgG-HRP	Santa Cruz Biotechnology	Cat# sc-2963, RRID:AB_639249
Alexa Fluor 488 donkey anti-mouse IgG	ThermoFisher Scientific	Cat# A-21202, RRID:AB_141607
Alexa Fluor Plus 555 goat anti-rabbit IgG	ThermoFisher Scientific	Cat# A32732, RRID:AB_2633281
Alexa Fluor 555 donkey anti-rabbit IgG	ThermoFisher Scientific	Cat# A-31572, RRID:AB_162543
Alexa Fluor 488 goat anti-mouse IgG	ThermoFisher Scientific	Cat# A-11001, RRID:AB_2534069
TNNT-FITC	Miltenyi Biotec	Cat# 130-119-575, RRID:AB_2751735
Biological Samples		
Patient-derived heart tissues	Centre of Cardiovascular and Transplantation Surgery, Brno, Czech Republic	N.A
Chemicals, Peptides, Plasmids and Recombinant Proteins		

Lipofectamine RNAiMAX	Invitrogen	Cat# 13778075
Dynabeads	Invitrogen TM	Cat# 10007D
Zirconia beads	Benchmark Scientific	Cat# D1032-30
Precision Plus Protein™ Dual Color Standards	Biorad	Cat# 1610374
Trizol reagent	Invitrogen	Cat# 15596026
DTT	Bio-Rad	Cat# 1610611
DNase I	Roche	**Cat# 04716728001**
Salt I	Millipore	**Cat#** CS203173
Salt II	Millipore	**Cat#** CS203185
Precipitate Enhancer	Millipore	**Cat#** CS203208
Cycloheximide	Sigma Aldrich	**Cat#** C7698
Proteinase K	Invitrogen TM	**Cat#** AM2548
Puromycin	Santa Cruz Biotechnology	**Cat#** sc-108071
DAPI	Sigma Aldrich (Roche)	**Cat#** 10236276001
Mowiol 4-88 mounting media	Sigma Aldrich	**Cat# 81381**
DABCO 33-LV	Sigma Aldrich	**Cat#** 290734
Bouin's solution	VWR Chemicals	**Cat#** 7000.1000
Celestin blue	Sigma Aldrich	**Cat#** 206342
Heparin (5000IU / ML)	Zentiva	**Cat#** 8594739026131
Fibrinogen (Tisseel_ Sealant Kit)	Baxter Bioscience	**Cat#** 1504514
Thrombin (Tisseel_ Sealant Kit)	Baxter Bioscience	**Cat#** 1504514
Aprotinin (Tisseel_ Sealant Kit)	Baxter Bioscience	**Cat#** 1504514
RIPA lysis buffer	Millipore	**Cat#** 20-188
Rnase-OUT	Invitrogen	**Cat#** 0777019
Tergitol	Sigma-Aldrich	**Cat#** NP40S
Latrunculin	Sigma-Aldrich	**Cat#** 76343-93-6

Y27632	Selleck Chemicals	**Cat#** S1049
CHIR99021	Sigma-Aldrich	**Cat#** SML1046
IWP2	Selleck Chemicals	**Cat#** S7085
B27 supplement minus	Thermo FisherScientific	**Cat#** A1895601
B27 supplement	Thermo FisherScientific	**Cat#** 17504044
Lithium dodecyl sulfate	Sigma-Aldrich	Cat#L9781
IGEPAL CA-630	Sigma-Aldrich	Cat#I3021
CompleteMini Protease Inhibitor Cocktail	Roche	Cat#11836170001
RNAseI	Thermo Fisher	Cat# EN0601
TurboDNase	Thermo Fisher	Cat# AM2239
T4 RNA Ligase 2 (truncated)	New England Biolabs	Cat#M0242S
CircLigase II	Lucigen	Cat#CL9021K
PEG400	Sigma-Aldrich	Cat#8074850050
Linear Acrylamide	Thermo Fisher	Cat#AM9520
Protein G	Thermo Fisher	Cat#10003D
pT7-V5-SBP-C1-HshnRNPC1	Addgene	plasmid # 64920
Phusion Hot Start II DNA Polymerase	Thermo Fisher	Cat#F549L
DpnI (10 U/µL)	Thermo Fisher	Cat#ER1701
PKC inhibitor (Chelerythrine Chloride)	Merck	Cat#C2932
Critical Commercial Assays		
High Pure RNA Isolation Kit	Roche	**Cat#** 11 828 665 001
SYBR Green I Master Kit	Roche	**Cat#** 04707516001
Phusion Flash High-Fidelity PCR Master Mix	Thermo Fisher	Cat#F-548L
Transcription First Strand cDNA Synthesis Kit	Roche	**Cat#** 04896866001
Pierce BCA Protein Assay Kit	ThermoFisher	**Cat#** 23225
Duo-link in situ PLA Kit	Sigma-Aldrich	**Cat#** DUO92101

NE-PERtm Nuclear and Cytoplasmic extraction kit	ThermoFisher Scientific	**Cat#** 78833
QIAseq Fastselect HMR Kit	Qiagen	**Cat#** 334376
M.O.M basic kit	Baria	**Cat#** BMK-2202
MinElute Gel Extraction kit	Qiagen	Cat#28604
QIAquick PCR purification kit	Qiagen	Cat#28104
SuperScript III Reverse Transcriptase Kit	Sigma-Aldrich	Cat#18080044
Dynabeads™ Protein G Immunoprecipitation Kit	Invitrogen TM	**Cat#** 10007D
Deposited Data		
TMT-Mass spectrometry data (hnRNPC interactome)	This study	Deposited to PRIDE PXD020663
RIP-sequencing data (hnRNPC-RNAs targets)	This study	Deposited to GEO GSE155472
RNA-sequencing data (AS in hnRNPC KD cells)	This study	Deposited to GEO GSE155473
iCLIP-seq data (hnRNPC in NHDF cells)	This study	Deposited to GEO GSE169068
Mouse 48h post-MI dataset	Harpster et al., 2006	GSE4648
Mouse heart failure dataset	Rowell et al., 2014	GSE54681
Human heart failure dataset	Barth et al., 2006	GSE3586
Human heart failure dataset (AS analysis)	Pepin et al., 2019*(103)*	GSE108157
Human heart failure dataset (AS analysis)	MAGNet; www.med.upenn.edu/magnet	GSE141910
Experimental Models: Cell Lines		
iPSCs	WiCell (Madison, WI, USA	DF 19-9-7T
NHDFs	ATCC	ATCC PCS-201-012™

Experimental Models: Organisms/Strains		
C57BL/6	IBMC-INEB	Nascimento et al.,2011*(36)*
Oligonucleotides		
hnRNPC Forward 5'-TCCCCTTCTTGTTTTCGGCT -3'	Generi Biotech (custom)	N.A
hnRNPC Reverse 5' – CTGAGTAGAGGGGACGGAGA -3'	Generi Biotech (custom)	N.A
GAPDH Forward 5'-AAGTATGACAACAGCCTCAA-3'	Invitrogen (custom)	N.A
GAPDH Reverse 5'-TCCTTCCACGATACCAAAGT-3'	Invitrogen (custom)	N.A
YAP-1α Forward 5'-GATGAACTCGGCTTCAGCCATGAA-3'	Generi Biotech	Vrbsky et al., 2021*(57)*
YAP-1α Reverse 5'-GCAGGGCTAACTCCTGCCGAAGCA-3'	Generi Biotech	modified from Karystinou 2015*(104)*
YAP-2α Forward 5'-CCTCTTCCTGATGGATGGGA-3'	Generi Biotech	Vrbsky et al., 2021*(57)*
YAP-2α Reverse 5'-GCAGGGCTAACTCCTGCCGAAGCA-3'	Generi Biotech	Vrbsky et al., 2021; Karystinou 2015*(57, 104)*
YAP-1β Forward 5'-GATGAACTCGGCTTCAGCCATGAA-3'	Generi Biotech	Vrbsky et al., 2021*(57)*
YAP-1β Reverse 5'-GCAGGGCTAACTCCTGTGGCCTCA-3'	Generi Biotech	Vrbsky et al., 2021*(57)*
YAP-2β Forward 5'-CCTCTTCCTGATGGATGGGA-3'	Generi Biotech	Vrbsky et al., 2021*(57)*
YAP-2β Reverse 5'-GCAGGGCTAACTCCTGTGGCCTCA-3'	Generi Biotech	Vrbsky et al., 2021*(57)*
YAP-1γ Forward 5'-GATGAACTCGGCTTCAGCCATGAA-3'	Generi Biotech	Vrbsky et al., 2021*(57)*

YAP-1γ Reverse 5'-TATTCCGCATTGCCTGCCGAAGCA-3'	Generi Biotech	Vrbsky et al., 2021; Karystinou 2015*(57, 104)*
YAP-2γ Forward 5'-CCTCTTCCTGATGGATGGGA-3'	Generi Biotech	Vrbsky et al., 2021*(57)*
YAP-2γ Reverse 5'-TATTCCGCATTGCCTGCCGAAGCA-3'	Generi Biotech	Vrbsky et al., 2021; Karystinou 2015*(57, 104)*
YAP-1δ Forward 5'-GATGAACTCGGCTTCAGCCATGAA-3'	Generi Biotech	Vrbsky et al., 2021*(57)*
YAP-1δ Reverse 5'-ATTGCCTGTGGCCTCACCT-3'	Generi Biotech	Vrbsky et al., 2021; Karystinou 2015*(57, 104)*
YAP-2δ Forward 5'-CCTCTTCCTGATGGATGGGA-3'	Generi Biotech	Vrbsky et al., 2021*(57)*
YAP-2δ Reverse 5'-ATTGCCTGTGGCCTCACCT-3'	Generi Biotech	Vrbsky et al., 2021; Karystinou 2015*(57, 104)*
YAP-i4 Forward 5'-AGCCCACTCGGGATGTAACTTGA-3'	Generi Biotech	Vrbsky et al., 2021; Karystinou 2015*(57, 104)*
YAP-i4 Reverse 5'-CTGGTGGGGGCTGTGACGTT-3'	Generi Biotech	Vrbsky et al., 2021; Karystinou 2015*(57, 104)*
YAP1 Forward 5'-CCTGAACAGTGTGGATGAGA-3'	Generi Biotech (custom)	N.A
YAP1 Reverse 5'-GCTTCAAGGTAGTCTGGGAA-3'	Generi Biotech (custom)	N.A
CD44 Forward 5'-GGAGCAGCACTTCAGGAGGTTAC-3'	Generi Biotech (custom)	Wang et al., 2017[41]
CD44 Reverse 5'-GGAATGTGTCTTGGTCTCTGGTAGC-3'	Generi Biotech (custom)	Wang et al., 2017*(19)*
EX2-3 Yap1 (F)- ACTTCTTAAATCACATCGAT	Generi Biotech (custom)	N.A
EX5 Yap1 (R): TGCCGAAGCAGTTCTTGCTG	Generi Biotech (custom)	N.A
CD44 ex v6 (F): GCAACTCCTAGTAGTACAACG	Generi Biotech (custom)	N.A
CD44 ex v8 (R): GCGTTGTCATTGAAAGAGGTC	Generi Biotech (custom)	N.A

MYLK ex11 Forward 5'-GAGCCAAGATGTTGTGAGCA-3'	Generi Biotech (custom)	Miao et al., 2010*(105)*
MYLK ex11 Reverse 5'-ATTCAGCAGCCAAGTGATCC-3'	Generi Biotech (custom)	Miao et al., 2010*(105)*
COL6A3 ex3 Forward 5'-AGCAGCAAGCAGATGTCAAA-3'	Generi Biotech (custom)	Arafat et al., 2011*(106)*
COL6A3 ex3 Reverse 5'-TTTCTCCCACAGCTAAGGATTT-3'	Generi Biotech (custom)	Arafat et al., 2011*(106)*
HNRNPC siRNA	Invitrogen	HSS179304
HNRNPC siRNA	Invitrogen	HSS179305
stealth siRNA negative control low GC	Invitrogen	12935200
hnRNPC siRNA *5' GCGCUUGUCUAAGAUCAAAU 3'*	Eurofingenomics	N.A (*79*)
Software and Algorithms		
ImageJ	Schneider et al., 2012*(107)*	https://imagej.nih.gov/ij/ ; RRID:SCR_003070
Imaris 9.0	Oxford Instruments	RRID:SCR_007370
Cytoscape 3.7.2	Shannon, 2003*(92)*	RRID:SCR_003032
Prism v 8.0.1	GraphPad	https://www.graphpad.com/ ; RRID:SCR_002798
rMATS v3.1.0	Shen et al., 2014*(88)*	rnaseq-mats.sourceforge.net/.
POSTAR2	Zhu et al., 2019*(37)*	http://lulab.life.tsinghua.edu.cn/postar/
ClueGO v2.5.6	Bindea et al., 2009*(93)*	RRID:SCR_005748
CluePedia v1.5.6	Bindea et al., 2013*(94)*	RRID:SCR_015784
EnrichR	Chen et al., 2013; Kuleshov et al., 2016	http://amp.pharm.mssm.edu/Enrichr ; RRID:SCR_001575

Integrative Genomics Viewer	Broad Institute	http://software.broadinstitute.org/software/igv/;
KEGG mapper	Kanehisa and Sato, 2020*(96)*	RRID:SCR_018145
WikiPathways	Slenter et al., 2018*(95)*	RRID:SCR_002134
Comparative Toxicogenomics Database (CTD)	Davis et al., 2018*(97)*	http://ctdbase.org/ ; RRID:SCR_006530
FastQC	Andrews, 2010*(79)*	RRID:SCR_014583
Trimmomatic v. 0.36	Bolger et al.,2014*(80)*	RRID:SCR_011848
STAR v. 2.5.3a	Dobin et al.,2013*(81)*	RRID:SCR_015899
RSeQC v. 2.6.2	Wang et al.,2012*(82)*	RRID:SCR_005275
Mascot version 2.5.1	Matrix Science	RRID:SCR_014322
Picard toolkit v. 2.18.27	GitHub Repository	http://broadinstitute.github.io/picard/; RRID:SCR_006525
Qualimap v.2.2.2	Okonechnikov et al.,2016*(83)*	RRID:SCR_001209
FastQ Screen v. 0.13.0	Wingett and Andrews,2018*(84)*	RRID:SCR_000141
bedtools subtract v2.29.0	Quinlan et al.,2010*(102)*	RRID:SCR_006646
featureCounts v. 1.5.2	Liao et al.,2014*(85)*	RRID:SCR_012919
Ggplot2 v3.3.1	Wickham, 2011*(86)*	RRID:SCR_014601
plotrix v3.7-8	Lemon, 2006*(87)*	https://www.rdocumentation.org/packages/plotrix/versions/3.7-8
Rmats2sashimiplot v2.0.2	Xinglab, 2015a*(108)*	https://github.com/Xinglab/rmats2sashimiplot
clusterProfiler v3.12.0	Yu et al., 2012*(89)*	RRID:SCR_016884
Proteomaps	Liebermeister et al., 2014; Otto et al., 2010*(35, 76)*	https://bionic-vis.biologie.uni-greifswald.de/

RepeatMasker	Smit, AFA, Hubley, R & Green, 2013-2015	http://www.repeatmasker.org
UMI-tools v. 0.5.5	Smith et al., 2017*(99)*	RRID:SCR_017048
bamCoverage v. 3.3.0	Ramírez et al., 2016*(100)*	NA
Adobe Illustrator	Adobe	https://www.adobe.com/ ; RRID:SCR_010279
Others		
Micropattern	CYTOO, Grenoble, France	ref: 10–950–10–18
Micropattern	CYTOO, Grenoble, France	ref: 10–950–00–18
Mini-PROTEAN TGX™ Precast Protein Gels	BioRad	Cat# 4561034
µ-Dish 35 mm, high ESS	ibidi GmbH, Munich, Germany	Cat# 81291

Table S2. Key Resource Table. The table includes all the reagents, deposited data, assays and software used in this paper.

Data file S1. Description of the datasets analysed in Fig. 1A, B. Related to Fig. 1. List of upregulated genes in dataset1 (mouse MI); dataset2 (mouse HF); datasets 3 and 4 (human HF).

Data file S2. Mass spectrometry data following hnRNPC immunoprecipitation in human heart tissue. Related to Fig. 2. i) List of hnRNPC interactors found by MS analysis in HF samples. Ii) List of hnRNPC interactors found by MS analysis in healthy heart samples. Iii) Proteomaps (based on the KEGG database) representing the quantitative composition of the hnRNPC interactome in healthy and HF human hearts

Data file S3. Mass spectrometry data following hnRNPC immunoprecipitation in human heart tissue. Related to Fig. 2. i) List of FHL2 interactors found by MS analysis in HF samples ii) List of PDLIM5 interactors found by MS analysis in HF samples iii) List of the common binding partners of hnRNPC, FHL2 and PDLIM5 in HF samples iv) GO cellular component analysis of the common interactors of hnRNPC, FHL2 and PDLIM5 in HF samples.

Data file S4. RNA-immunoprecipitation sequencing data. Related to Fig. 4**.** i) List of transcripts bound by hnRNPC in HF samples found by RNA-IP sequencing. ii) List of exon-enriched targets and intron-enriched targets.

Data file S5. RNA sequencing data upon hnRNPC depletion in NHDF cells. Related to Fig. 7. i) List of transcripts undergoing AS (SE; MXE; A5SS; A3SS; IR) in *HNRNPC* KD cells and pathway enrichment analysis by WikiPathways.

Data file S6. AS of Hippo pathway transcripts following hnRNPC depletion and/or direct target of hnRNPC. Related to Fig.7. i) **Hippo_ASanalysis.** Transcripts belonging to the Hippo pathway displaying alternative splicing in hnRNPC KD cells. KEGG mapper representation of HIPPO pathway: transcripts showing altered AS in hnRNPC KD cells are highlighted in red. ii) **Hippo_iCLIPanalysis.** Transcripts belonging to the Hippo pathway bound by hnRNPC in NHDF cells. KEGG mapper representation of HIPPO pathway: hnRNPC targets are highlighted in red. iii) **Hippo_AS_iCLIP_Venn.** Venn diagram showing the transcripts belonging to Hippo pathway common to the two datasets. iv) **Hippo_RNAIP.** Transcripts belonging to the Hippo pathway bound by hnRNPC in failing hearts. KEGG mapper representation of HIPPO pathway: hnRNPC targets are highlighted in red. v) **Hippo_AS_iCLIP_RNAIP.** Venn diagram showing the transcripts belonging to Hippo pathway common to the three datasets

Data file S7. iCLIP data. Related to Fig. 7. i) Number of reads in each sample (N=3); ii) List of hnRNPC targets; iii) List of transcripts common to iCLIP analysis and AS analysis; iv) Number of reads on coding vs non coding elements; v) Number of reads on Alu elements.

Data file S8. Comparative Toxicogenomics Database (CTD) analysis. Related to Fig.8. **i)** List of transcripts common to iCLIP, RNA-IP and AS analyses; ii) List of disease categories found by CTD analyses of the transcripts common to iCLIP, RNA-IP and AS analyses iii) List of hnRNPC-targets belonging to the cardiovascular diseases category.

Data file S9. In silico AS analysis in human healthy and HF heart samples. Related to Fig. S12. List of transcripts undergoing AS displaying the same AS events in HF samples (from GSE108157 and GSE141910) and in *HNRNPC* KD NHDFs.